Light Water Reactor Safety Research Program Quarterly Report July - September 1978

Light Water Reactor Safety Department

Printed April 1979

Sandia Laboratories

Prepared for

U. S. NUCLEAR REGULATORY COMMISSION

(112)

467   192

7907260363

467 193

LIGHT WATER REACTOR SAFETY RESEARCH PROGRAM
QUARTERLY REPORT JULY-SEPTEMBER 1978
Vol. 9

APPROVED:

_____
Manager, Light Water Reactor Safety Department

_____
Director, Nuclear Fuel Cycle Programs

Contributing Authors:

W. B. Benedick
M. Berman
B. M. Bulmer
L. D. Buxton
R. K. Byers

R. K. Cole, Jr.
D. O. Lee
J. F. Muir
L. S. Nelson
D. A. Powers
G. P. Steck

4

CONTENTS

TABLES

TABLES (cont)

ILLUSTRATIONS

ILLUSTRATIONS (cont)

ILLUSTRATIONS (cont)

467 199

ILLUSTRATIONS (cont)

200

1. Molten Core/Concrete Interactions Study

1.1 Summary

The Molten Core/Concrete Interactions Study was begun on July 15, 1975, to provide a qualitative, extensive exploration of the phenomena associated with contact between molten-core materials and concrete. The experimental elements of this study are divided into four categories:

a. Deposition of Corium-type melts onto concrete

b. Kinetics and stochiometry of the thermal decomposition of concrete

c. Response of concrete to high heat fluxes at one surface

d. Simulation experiments which explore phenomena at the interface between a melt and a decomposing solid.

Experimental results are being incorporated in a computer model and a scaling analysis. They will establish scaling parameters for the system and identify key elements of the melt/concrete interaction. A complete project description of the study was issued in October 1975.[1]

During the quarter, tests were performed as part of the ongoing BURN experimental program. These are small-scale tests intended to develop instrumentation and techniques for the quantitative study of melt/concrete interactions.

The BURN 3 test used induction heating to heat a slug of steel, emplaced in a crucible of CRBR concrete, up to its melting point. The test was similar to BURN 2 (reported last quarter) except for the use of CRBR instead of limestone concrete and incorporation of more extensive instrumentation. Both the concrete and steel began to melt when the steel temperature reached about 1400°C. Erosion of concrete proceeded in both downward and radial directions. The downward erosion rate of 3.7 cm/h, based on thermocouple failure time, is slightly greater than the 3.2 cm/h observed in BURN 2 for limestone concrete. Radial erosion rates calculated from posttest cavity measurements ranged from 4.1 to 4.6 cm/h. These are ~10 to 24% greater than the axial erosion rate in contrast to the results of test BURN 2 where the radial erosion rate was only 70% of the axial rate.

The analytical effort during the quarter concentrated on programming of, and phenomeno-logical model development for, the improved molten core/concrete interaction code, CORCON. In addition to the continuing effort on the core/concrete interface heat transfer model, work has begun on models for the following: gas phase thermochemical equilibrium, concrete ablation and shape change, transport properties of gas mixtures, viscosity and density of silicate melts, radiative heat transfer from the molten pool surface to the surroundings, convective heat transfer from the gas mixture above the pool to its surroundings, and convective heat transfer from the periphery of the pool (i.e., at the melt/interface boundary) to the pool interior. In addition, a study of the numerical aspects of INTER and CORCON was begun for the purpose of identifying the problem areas in INTER and suggesting improved numerical techniques for use in CORCON.

1.2   Molten Core/Concrete Interaction Experimental Program (D. A. Powers)

1.2.1 Status of the BURN Test Series

The BURN tests are a group of small-scale experiments intended to develop instrumentation and techniques for the quantitative study of melt/concrete interactions. Major issues being ex-plored in this test series include

- Development of sustained material interactions method

- Development of x-ray techniques for real-time monitoring of melt concrete interactions,

- Study of interaction between hot, but not necessarily molten, core debris and concrete.

Two of the BURN tests have been described earlier.[2] Here descriptions of other tests are presented, and the results of all tests are summarized. Results of the tests have shown the need for further experimentation, and future tests in the BURN series are described.

Crucibles used in the experiments were cut from a 6-in. diam, 12-in. long concrete testing cylinder, manufactured at the same time other concrete fixtures used in the experimental program were made. Crucible cavities are typically 3-1/2 in. in diameter and 6 to 7 in. long. Instrumenta-tion used in the tests has been varied according to the needs of the experiment. In general, test instrumentation included the thermocouples necessary to monitor the directional nature of concrete erosion and concrete thermal response.

Tests conducted thus far in the BURN series are summarized in Table 1-I. BURN 1 and 2 have been discussed before.[2] Results of BURN 0, 3, and 4 are described below.

BURN 1 was a successful demonstration of an x-ray technique that allows real-time con-tinuous observation of a high-temperature melt in contact with concrete. Melt behavior, gas flow behavior, and concrete interfacial behavior were readily visible in this test. All of these processes

must be adequately modeled if a computer model to extrapolate experimental results to realistic situations is to be devised.

TABLE 1-I

Summary of BURN Tests

Test	Concrete	Objective	Remarks
BURN 0	Limestone	Sustain a THERMITE-generated Corium melt at temperature using Joule heating supplied via two tungsten electrodes buried in concrete. Also observe interaction between Corium melt and candidate refractories - W_2B, HfC, Y_2O_3, ZrO_2 (CaO).	Wild variation in resistivity of oxidic phase made control of the dc power supply difficult. After ~30 s, overload occurred and the test was terminated.
BURN 1	Limestone	Use x-ray imaging technique to observe melt/concrete interface in real time.	BURN 1 was quite successful. Brief results and collateral data reported in Reference 2.
BURN 2	Limestone	Use inductive heating to warm steel to near its melting point while in contact with concrete. Test simulated both the interaction of fragment debris beds with concrete and the interaction of core melts late in an accident when melt solidification occurs and the concrete has been largely dehydrated.	BURN 2 was quite successful. Data have been reported in Reference 2. Erosion of concrete began at ~1300°C - a temperature below liquidus of concrete but well above solidus. Downward erosion ~3 cm/h. Radial erosion ~1.7 cm/h
BURN 3	Generic southeastern United States concrete	Similar to BURN 2 with a more refractory concrete and with more extensive instrumentation.	Result analogous to those of BURN 2 reported below.
BURN 4	Generic southeastern United States concrete	Deposit a THERMITE-generated melt into concrete and sustain that melt by inductively heating metallic phase.	Prompt gas release at the time melt impacted the concrete caused the melt to be expelled from crucible cavity. Instrumentation leads from crucible were destroyed and the test was terminated.

BURN 1 was, however, a test to demonstrate an experimental technique. Its success has led to plans for additional tests. Not all the details of these experiments have been resolved. Three tests are planned and possible descriptions for these x-ray (XR) series tests are shown in Table 1-II. Sustained melt/concrete interactions tests are not among these possibilities due to equipment limitations.

467 204

13

TABLE 1-II

Summary of Planned X-Ray Tests

Test	Concrete	Crucible	Objective
XR-1	Basaltic	16-in. diam., 18-in. high; cavity 8-in. diam, 12-in. high. Melt head to be at least 4 in.	Determine radial and downward erosion rates. Cavity diameter sufficient to include at least 3 nodes predicted by the gas film model for heat transfer from melt to concrete. Have sufficient melt head that gas bubble diameters in the melt are small. Measure heat flux and correlate result with observed melt behavior. Correlate gas behavior observed in the melt with gas composition and flow rates.
XR-2	Limestone	Identical to XR-1.	
XR-3	Basaltic	Spherical cavity of 8-in. diam.	Same as XR-1 and XR-2. Also determine influence of geometry and melt head on results.

The other BURN tests have been attempts to determine what techniques may be used to sustain interactions between molten core materials and concrete. To do this requires that additional heat be supplied to the melt. Two techniques for supplying this heat have been tried:

Joule heating - BURN 0

Induction heating - BURN 2, 3, and 4

Induction heating was clearly successful in heating metallic core materials in contact with concrete. Rapid heating (0.3 to 3°C/s) of cold metal on concrete could be achieved before the concrete adjacent to the metal began to melt, but then the metal temperature stabilized and additional heat supplied to the metal was conducted away by liquified concrete and at least partially consumed in melting more concrete. When the melting temperature range of the concrete was below the solidification temperature of the metal (BURN 2), the metal remained solid. When concrete melted at temperatures above the liquidus of the metal (as in BURN 3) a fully developed, two-phase, molten pool formed.

The inability to superheat the melt may be due to equipment limitations, experimental design, or the operative physics during melt/concrete interactions. Further tests using inductive heating will minimize the second of these possibilities and hopefully maximize the use of existing equipment capabilities. An important milestone in this test program will be reached when experiments with larger crucibles are completed.

Tests in which the core materials were not melted have yielded very useful information. The BURN 2 test demonstrated that core materials need not be molten to erode the concrete or to cause the liberation of substantial volumes of gas. The onset of erosion was shown in BURN 2 and BURN 3 to be dependent on the melting properties of the concrete. Erosion of any significance began at temperatures above the solidus temperatue of concrete yet below its liquidus temperature as determined by differential thermal analysis. These observations will significantly affect modelling long-term behavior of melt/concrete interactions and the interaction of fragmented debris beds with concrete.

Adequate modeling of the processes observed in BURN 2 and 3 cannot be done at this time without improved data concerning upward heat fluxes. Data from BURN 3 suggest that the time variation of this upward heat flux is complex.

Little success has been had in first forming a high-temperature melt, then depositing it into concrete and sustaining it inductively. Considerable redesign of the test arrangement used in BURN 4 will be necessary if this experimental operation is to be useful. Gases liberated during the initial contact between the melt and concrete must be vented without being allowed to expel melt from the heating region of the induction coil. Melt generation within the crucible cavity is not especially useful since the volume of melt created would be too small for adequate inductive coupling. Techniques such as those used in the NSS test series[3] may be useful in solving this problem.

The BURN 0 test was an attempt to use Joule heating to sustain a thermetically generated Corium melt. This test failed because limitations in the experimental equipment did not permit rapid control of current flow between the tungsten electrodes used for such heating. Attempts are now being made to overcome these equipment limitations. It is likely some combination of inductive and Joule heating may be a suitable solution.

Joule heating is a subject of some interest since it can be used to mimic internal heat generation in oxidic phases.

Future tests planned in this series are summarized in Table 1-III. BURN 5 and 6 will be similar to BURN 2 and 3. Instrumentation applied to these tests will include monitors of gas generation, gas composition, and upward heat flux. The latter is proving to be an essential parameter to perform heat balance calculations on the tests.

The BURN 7 test will have powdered UO_2 and granular stainless steel interacting with concrete. Power will be supplied to the system by inductive coupling to the metal phase. Specific phenomena to be addressed in the test are:

Crust formation via sintering in UO_2

Core debris stratification

UO_2 dissolution in molten concrete

Steel oxidation.

As planned, the initial bed will be well mixed. Evidence from other sources indicates that upon melting the stainless steel stratification will occur.[4] As melting of the concrete begins, the core debris may stratify into a three-layer bed.[5] Ultimately, the debris will evolve into a liquid metal layer covered by a liquid oxide layer.

TABLE 1-III

Future BURN Series Tests

Test	Concrete	Objective
BURN 5	Basaltic	Similar to BURN 2 and BURN 3. Rates of gas evolution as well as concrete erosion will be monitored throughout the test.
BURN 6	Generic south-eastern United States concrete	Similar to BURN 5
BURN 7	Choice based on results of BURN 5 and BURN 6	Interaction of Corium-E composition powder bed with concrete. Heating supplied by inductively heating metallic phase which will consist of 100 mesh, Type 304 stainless steel powder. Both BURN 7 and 8 will follow tests in the CATH series being done for the Advanced Reactor Safety Branch of the NRC.
BURN 8	Choice based on results of BURN 7	Similar to BURN 7 except additional heat provided by Joule heating of oxidic material in melt.
BURN 9, 10	Basaltic and limestone	Sustained interaction of THERMITE-generated melt. Inductive heating techniques will be used. Crucible design will be quite different than in other tests.

The BURN 8 test will be similar to BURN 7 except both inductive heating and Joule heating will be used. The metal phase will be inductively heated to about 1000°C. At this point the oxidic phase will be conductive and may be heated by Joule techniques.

The small size of the crucibles used in the BURN tests may not permit sustaining interactions for periods long enough to allow all pertinent phenomena to fully develop. For this reason BURN 5 and 10 will use crucibles with cavities 8 in. in diameter and 12 in. long. Melt masses will be of the order of 30 lb.

16

467 207

1.2.2 <u>Preliminary Results of Some Tests in the BURN Series</u>

Preliminary results from BURN 0, 3, and 4 are presented below.

<u>BURN 0</u> -- A schematic diagram of the crucible and test fixture used for BURN 0 is shown in Reference 6. A limestone concrete crucible 6 in. in diameter and 12 in. long with a 3-13/16 in. diam., 5-1/4 in. deep cavity was used. Half-inch diameter holes about 1-1/8 in. long were drilled in the bottom of this cavity. These holes were filled with 1/2 in. diam rods of the four refractory materials:

ZrO_2 (CaO stabilized) (rod 1.545 in. long)

Y_2O_3 (rod 1.50 in. long)

WB_2 (rod 1.695 in. long)

HfC (rod 1.610 in. long)

A photograph of these material samples in place is shown in Figure 1-1. These materials were being tested for compatibility with high-temperature Corium melt during the test.
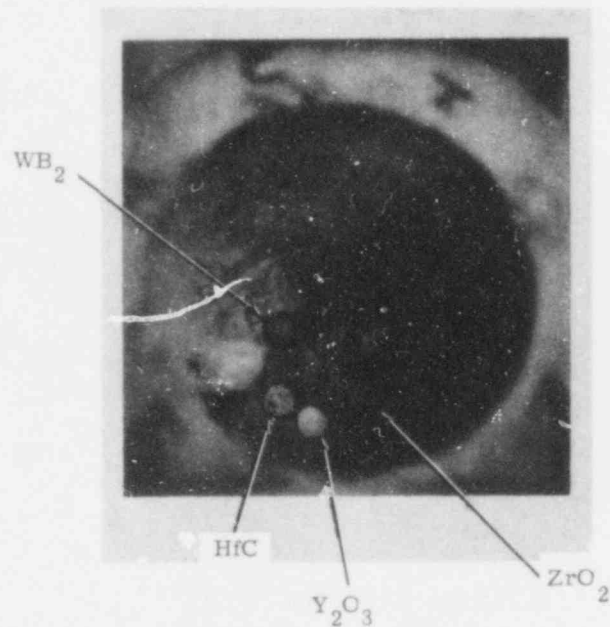
Figure 1-1. Locations of Refractory Specimens in the
BURN 0 Test

On opposite sides of the crucible cavity, 1/2 in. diam holes were drilled through the crucible walls. Tungsten electrodes (< 1/2 in. diam) sheathed with SiO_2 tubes with 1-mm-thick walls were cemented in these holes with Saureisen 63 castable refractory. The electrodes were connected to a 300 amp dc power supply.

467 208 17

The crucible was capped with an instrumentation tower similar to, but smaller than, that used in the NSS test series. No instrumentation was mounted in this tower, nor was the test extensively instrumented. The test was an attempt to demonstrate Joule heating techniques and, somewhat incidentally, the compatibility of refractories with the melt. The initial melt was generated using 5 kg of the Corium thermitic composition described else ..re. Under ideal conditions the melt would have a composition (wt %) of 54 UO_2, 17 ZrO_2, and 30 stainless steel. The reaction mixture was ignited with Pyrofuze.

About 15 s after ignition the tungsten electrodes were energized. The electrodes were operated at 10 to 20 V for about 30 s. At that time excessive power demands were placed on the power supply and the test was terminated.

Posttest x-rays of the crucible are shown in Figures 1-2 and 1-3. From these x-rays, the following observations concerning refractory compatibility with the melt may be made:

- Zirconia rod - thermally fractured.
- Yttria rod was thermally fractured.
- Tungsten boride rod was chemically attacked.
- Hafnium carbide rod both thermally fractured and chemically attacked.
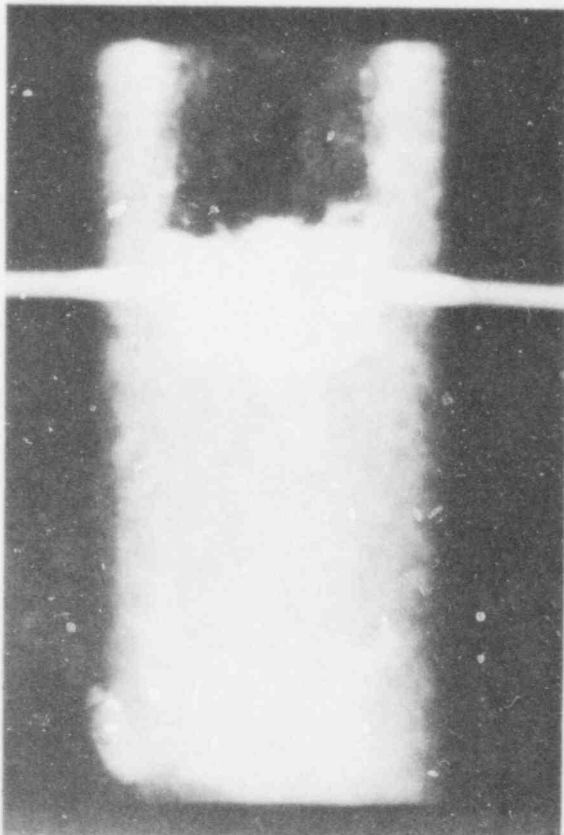
Figure 1-2.   Posttest X-Ray of Crucible Used
in BURN 0.   Angle 0 Degree
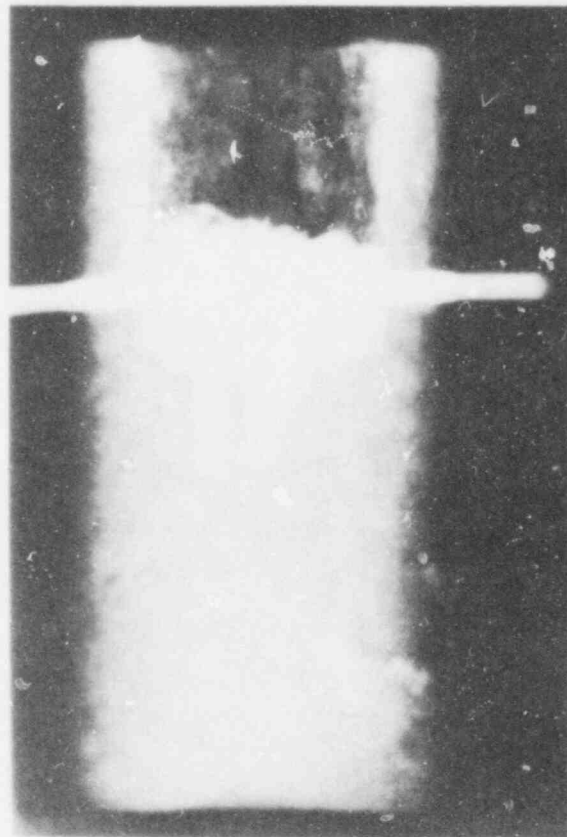
Figure 1-3.   Posttest X-Ray of Crucible Used
in BURN 0.   Angle 225 Degrees

18

BURN 3 -- This test was quite similar to a test previously described--BURN 2--except that the crucible was fabricated from the so-called CRBR composition concrete. A steel slug within the cavity of the crucible was heated by an induction coil energized with a 50 kW, 3000 Hz, Inducto 50 power supply. The induction coil and crucible were packed in dry-ram insulation as depicted in Figure 1-4. Physical sizes of the experimental fixture are listed in Table 1-IV.
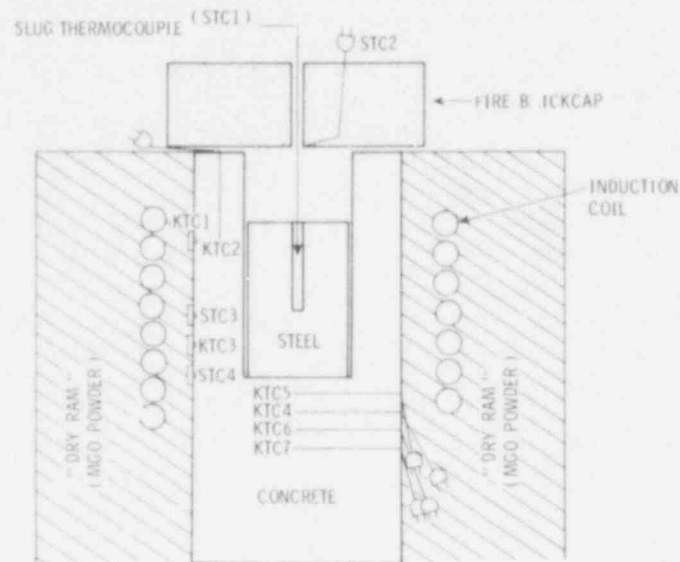
Figure 1-4. Schematic of Test Fixture Used in BURN 3

TABLE 1-IV

BURN 3 Fixture Dimensions

Crucible length	12 in.
Crucible diameter	6 in.
Cavity depth	6-1/2 in.
Cavity diameter	3-1/4 in.
Slug length	4-1/2 in.
Slug diameter	3 in.
Slug weight	5 kg
Depth of thermocouple well in slug	2-1/2 in.
Thickness of firebrick cap on crucible	2-1/2 in.
Top of induction coil from top of crucible	2-1/2 in.
Bottom of induction coil from top of crucible	8-1/2 in.
Induction frequency	3000 Hz
Concrete type	Generic southeastern United States calcareous

Instrumentation used in the test consisted basically of thermocouples embedded in the concrete to detect movement of the melt. Locations of these thermocouples are described in Table 1-V.

TABLE 1-V

Thermocouples Used in BURN 3

Thermocouple	Type	Location[a]	Data
STC-1	Bare Type S wires in alumina insulator	Within slug on aluminum oxide pedestal	Yes (see Figure 1-5)
STC-2	Platinum-sheathed MgO insulated types	In capping assembly	Yes (see Figure 1-6)
STC-3	Bare Type S wires sheathed in SiO_2	On crucible wall[b] 2 in. above original cavity bottom	No
STC-4	Bare Type S wires sheathed in SiO_2	On crucible wall 1/4 in. above original cavity bottom	Yes (see Figure 1-7)
KTC-1	0.040 in. OD stainless-steel-sheathed MgO insulated Type K	On crucible wall 4 in. above original cavity bottom	No
KTC-2	Same as KTC-1	3/4 in. from original cavity wall, 4 in. above original cavity bottom (a)	No
KTC-3	Same as KTC-1	On crucible wall 1 in. above the original cavity bottom (a)	Yes (see Figure 1-8)
KTC-4	Same as KTC-1	1 in. below original cavity bottom; junction at centerline of crucible	Yes (see Figure 1-9)
KTC-5	Same as KTC-1	1/2 in. below original cavity bottom; junction at centerline of crucible	No
KTC-6	Same as KTC-1	1-1/2 in. below original cavity bottom; junction at centerline of crucible	No
KTC-7	Same as KTC-1	2 in. below original cavity bottom; junction at centerline of crucible	No

[a] All thermocouples at horizontal locations except KTC-1 which was vertically oriented.

[b] Wall thermocouples mounted as described in Reference 2.

An attempt was made to differentially monitor the response of concrete to the heat flux from the inductively heated steel. A thermocouple located within an aluminum oxide filled, 1/4 in. ID fused silica tube, mounted 1 in. below the bottom of the crucible cavity, was differentially coupled to a thermocouple in the concrete. The thermocouple in the concrete was also 1 in. below the bottom of the crucible cavity in a 0.083 in. diam hole packed with concrete powder.

Only those thermocouples whose output was recorded after being passed through integrating digitizers yielded useful data. Those thermocouples were connected directly to recording apparatus coupled to the induction field and produced data too noisy to be of use. Good data were recorded from the following thermocouples:

1. Thermocouple in the 1″ 1 slug   (Figure 1-5)

2. Thermocouple in the firebrick cap over the crucible   (Figure 1-6)

3. Thermocouple in a groove on the wall of the crucible   (Figure 1-7)

4. Thermocouple 1 in. below the bottom of the crucible cavity   (Figure 1-9)
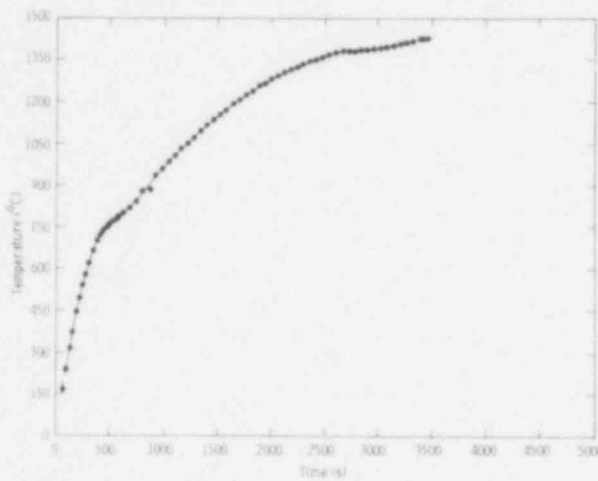
Figure 1-5. Steel Temperature, BURN 3   Figure 1-6. Cap Thermocouple, BURN 3
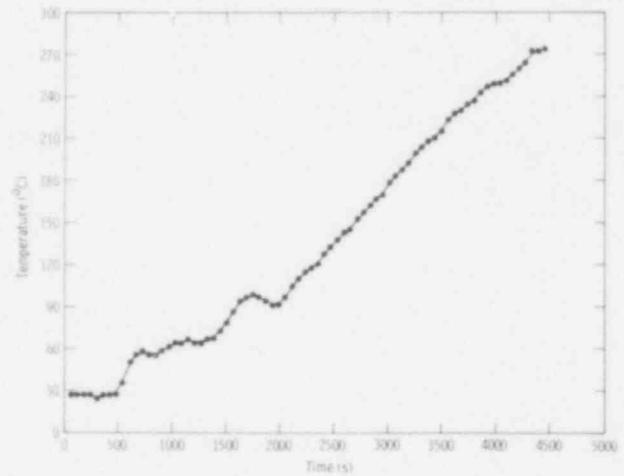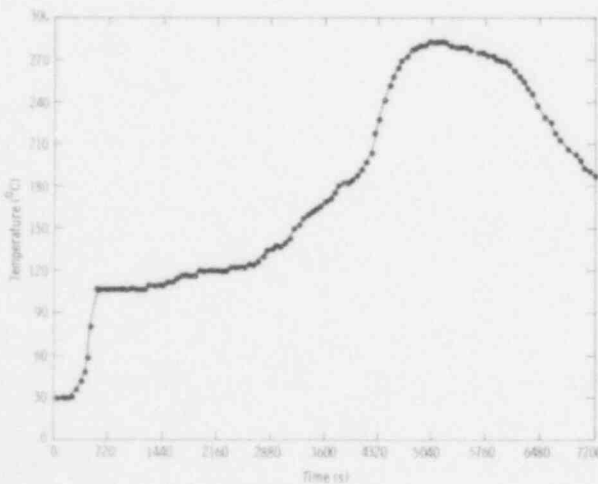
Figure 1-7. BURN 3 Wall Thermocouple   Figure 1-8. BURN 3 Thermocouple
(1/4 in. above cavity bottom)   (1 in. above cavity bottom)

Figure 1-9. BURN 3 Thermocouple
(1 in. below cavity bottom)
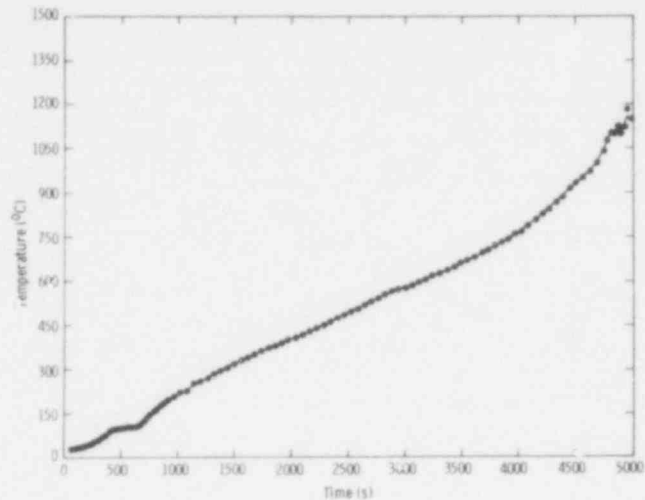
The steel slug was heated at a rate of ~ 2°C/s from 30 to about 700°C. This corresponds to an energy input rate of about 7.1 kW if it is assumed the system was adiabatic. Once the curie temperature of the steel was exceeded, the heating rate slowed to 0.35°C/s or an energy input rate of 1100 W.

At about 1400°C heating of the steel slowed greatly as both concrete and steel began to melt. The onset of the melting attack on concrete was taken to be 2500 s after the start of the test.

Posttest inspection of the fixture showed that the steel had completely melted. This result was expected in view of the very high liquidus temperature of CRBR concrete (estimated to be 1600°C).[7] Some of the steel formed a compact disk with a maximum diameter of 5.8 in., a minimum diameter of 5.375 in., and weighing 2615 g. This disk was found at the bottom of the crucible cavity. A second piece of highly distorted steel was found near the top of the crucible. It weighed 725 g. The balance of the steel was oxidized or distributed within the oxidic contents of the crucible cavity. Photographs of the steel pieces are shown in Figures 1-10 and 1-11.

This configuration of the steel could not lead to very good coupling between the steel and the induction coil. A further detriment to inductive coupling was that, at the conclusion of the experiment, the steel slug was at a level near the bottom of the induction coil.

The very low temperatures reached by the thermocouple in the crucible capping assembly suggest that this sensor was not well-suited for detecting upward heat fluxes during the experiment. The device did produce some unusual results. Temperatures were constant up to about 480 s. At that point the temperature rose sharply to about 60°C. Temperatures rose slowly and not monotonically to about 100°C during the period of 490 to 2000 s after the start of the test. Data from thermocouples within the concrete suggest that this was the period during which water was being driven from the concrete. That portion of the water that escaped the concrete and passed through the capping assembly was probably responsible for heating of the thermocouple. Such a heat transfer mechanism would account for the vary nonlinear temperature rise of the thermocouple and is

467 213

consistent with the temperatures observed. Condensing water on the capping assembly would be expected to hold the cap temperature low and fairly constant.
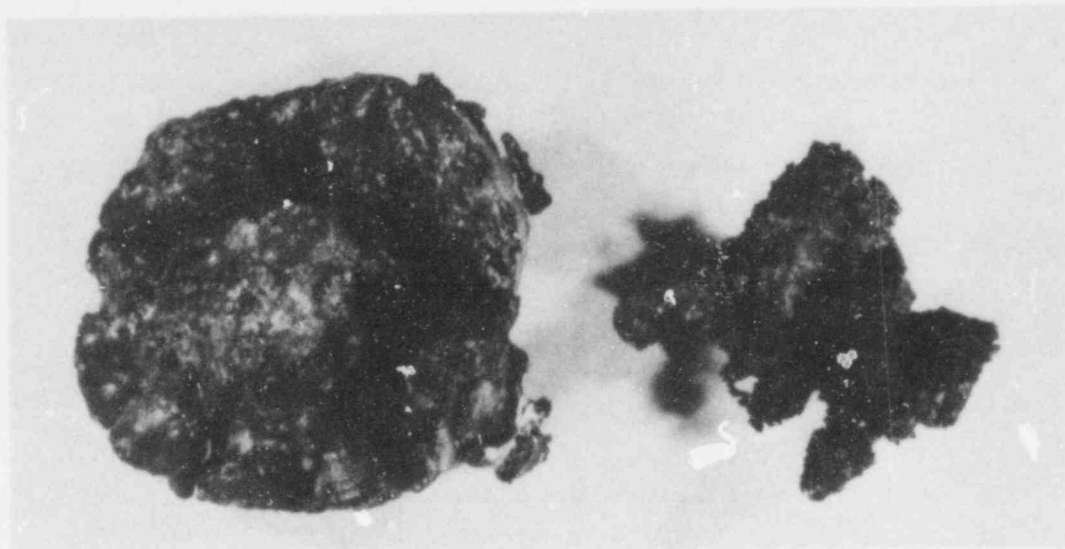
Figure 1-10. Top View of Steel From BURN 3 Test
(Sandia negative C78-9404)
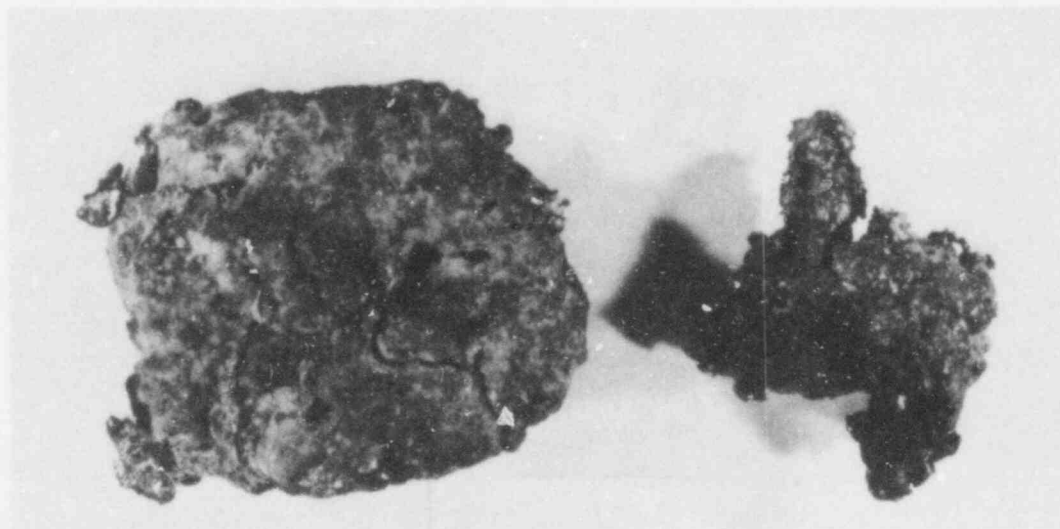
Figure 1-11. Bottom View of Steel From BURN 3 Test
(Sandia negative C78-9405)

After 2000 s the capping thermocouple indicated a fairly linear temperature rise of about 0.1°C/s.

The thermocouple 1 in. below the original bottom of the crucible cavity showed a temperature rise to a level of 102°C about 420 s after the start of the test. This level lasted for 250 s. The temperature rose smoothly again until failure 4950 s after the start of the test. This failure would indicate a downward erosion rate of 3.7 cm/h. This erosion rate is somewhat greater than the rate of 3.2 cm/h observed for the erosion of ordinary limestone concrete observed in BURN 2.

The difference may be attributed to the higher temperatures that molten steel developed in BURN 3.

Thermocouple outputs from sensors located on the walls of the crucible were quite different from that of the thermocouple below the crucible cavity. Temperatures at the locations of these sensors rose rapidly to an arrest again at about 102 to 120°C, 450 s after the start of the test. Temperatures rose no more than 20°C for the next 2000 s, then temperatures increased at a rate of 2.5°C/min up to about 170°C. Then the temperatures rose quite sharply. Neither of the wall thermocouples failed so that a radial erosion rate could not be calculated.

A possible explanation for the observed behavior of the wall thermocouples: The concrete walls of the crucible cavity are not in contact with the steel while it is heated. Steam and gases liberated from the concrete pass through the gap between the steel and the concrete and keep the walls cool. No such cooling mechanism is available at the bottom of the crucible cavity which is in intimate contact with the steel. Once concrete begins to melt, liquid-phase heat transfer from the steel to the concrete accelerates temperature rises in the wall concrete. The liquid phase reduces the cooling effect of gases passing upward along the wall. Collapse of the steel prevented any very large temperature rise in the 1/4-in. wall thermocouple.

Posttest inspection of the test fixture showed there was a frozen slag layer between the steel and concrete at the bottom of the cavity. Frozen slag layers on the walls of the crucible cavity were 0.4 to 1.6 cm thick, as shown in Figure 1-11. Concrete on the walls which had clearly been affected by the heat, but not melted, was 0.2 to 0.5 cm thick. Radial erosion rates calculated from these posttest measurements are 4.1 to 4.6 cm/h. These rates are greater than the observed axial erosion rate of 3.7 cm/h, whereas in BURN 2 the radial erosion rate was only 70% that of the axial rate.

The fact that the melt so easily migrated in the radial direction is strong evidence that neither the Lorenz forces produced by the coil nor the water-cooling of the coil had strong influence on the nature of the melt/concrete interaction.

The results of BURN 3 are curious indeed and must be verified or refuted. Some modifications that have been arranged for the repeat tests include

- Low-pass filters for thermocouples to eliminate induction noise,

- Reorientation of the induction coil so that axial erosion of concrete does not move the steel out of the effective heating zone of the coil,

- Improved melt temperature measurements, and

- Capping system that allows gas generation rates to be monitored.

24

BURN 4 -- The experimental and instrumental arrangements used in test BURN 4 were quite similar to those used for BURN 3. However, the melt to be sustained in BURN 4 was generated metallothermically in a generator similar to that used in the PLATE test series. A melt-out plug in the generator allowed the melt to flow into the awaiting concrete crucible. Once in place, the melt was to be sustained by induction coils wrapped around the crucible.

The metallothermic generator was used instead of igniting the metallothermic reaction within the concrete crucible so that the crucible could be filled with melt. Powder densities of the reaction constituents are too low to generate sufficient melt in situ. Unfortunately, gas generation initiated by the melt when it entered the crucible was so great that nearly all the melt was expelled from the crucible, and it destroyed most of the instrumentation sensors used in the test. Insufficient melt remained for sustained interaction by induction heating. Consequently, the test was terminated. A posttest x-ray of the crucible is shown in Figure 1-12.
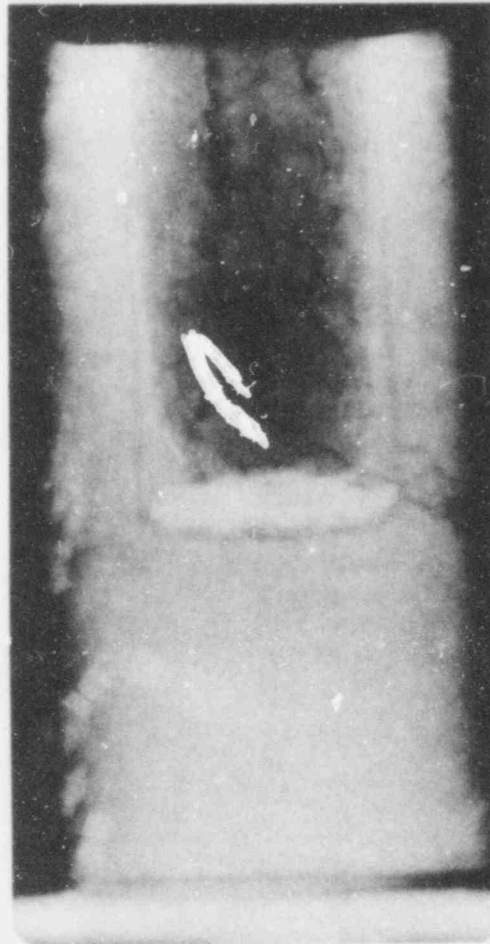
Figure 1-12. Posttest X-Ray of Crucible Used in
BURN 4

25

467 216

1.3 Molten Core/Concrete Interaction Analytical Program

1.3.1 Model Development (J. F. Muir)

Development of an improved molten core/concrete interaction model, CORCON, continued. Efforts during the quarter concentrated on computer programming and phenomenological model development.

In addition to the continuing investigation of thermal-hydraulic phenomena at the core/concrete interface (discussed below), model development efforts were initiated to describe many of the other physical and chemical phenomena which characterize the interaction process. These include

- Thermochemical equilibrium of the reacting gas mixture above the molten pool,

- Concrete ablation and shape change of the eroded cavity,

- Transport properties of gas mixture,

- Viscosity and density of the oxide melts,

- Radiative heat transfer from the pool surface to the surroundings above the pool,

- Convective heat transfer from the gas mixture above the pool to the surroundings, and

- Convective heat transfer from the periphery (sides and bottom) of the molten pool (at the melt/interface boundary) to the pool interior.

The first two models are being developed by ACUREX/Aerotherm Corporation under contract to Sandia. The Aerotherm Division of ACUREX, under sponsorship of the U.S. Air Force, has been a major developer of computer models for reentry vehicle heatshield ablation calculations. Two of these, the Aerotherm Chemical Equilibrium (ACE) and ABRES Shape Change (ASC) codes, employ techniques that are directly applicable to the model required for CORCON.

The third model is extracted, with some modifications, from the REALG code developed by F. G. Blottner for computing the thermodynamic and transport properties of equilibrium real gas mixtures.[8] It will be used to calculate the mixture dynamic viscosity and frozen thermal conductivity of the gas mixtures present in the core/concrete interface region and above the pool.

The fourth model listed above is a modified and greatly simplified version of the VISRHO code developed by D. A. Powers for estimating the viscosity and density of complex silicate melts.[9] The viscosity data base for VISRHO, currently for silicon dioxide concentrations of between 81 and 35%, is being extrapolated to include SiO_2 concentrations down to 15%. Other changes will allow extrapolation of the computed melt density and viscosity to melt temperatures outside the present range of 1200 to 1800°C.

The remaining three models address phenomena whose complexity is derived at least in part from the fact that the characteristic geometry will in many instances be unknown. As a result, these models will employ enough simplifying approximations to enable the construction of models capable of predicting realistic magnitude and trends in the unknown variables as functions of the relevant interaction parameters and consistent with the level of approximations employed elsewhere in CORCON.

In addition to the phenomenological model development efforts described above, a study of the numerical aspects of INTER and CORCON has been started for the purpose of identifying numerical problem areas in INTER and recommending improved numerical techniques for use in CORCON.

1.3.2 Interface Thermal-Hydraulics Study (B. M. Bulmer and D. O. Lee)

This study includes both analytical and experimental investigations of phenomena occurring at the core/concrete interface. The objectives are (1) to define the various interface flow configurations, the conditions under which they exist, and the necessary transition criteria, (2) to determine local heat and mass transfer across and along the interface as a function of interface configuration and local geometry material properties, and to determine flow characteristics, and (3) to provide results suitable for inclusion in CORCON.

The analytical studies include a stability analysis covering the items in the first objective and an integral study directed toward the second one. The experimental investigations using simulant materials are designed to furnish information relevant to all of the above objectives and provide guidance for the analytical studies and verification of the phenomenological models developed.

The current status of the analytical and experimental studies is as follows.

The final design of an apparatus suitable for performing the desired interface stability experiments has been completed. It is a tank approximately 6 x 9 x 24 in. deep, in which a liquid pool can be maintained above a porous plate through which a gas may be injected at controlled rates. The apparatus is designed to provide porous plate inclination angles ranging from 0 to 90 degrees. Optical quality windows are provided for both quantitative and qualitative observations (visual and photographic) of the pool/plate interface configurations (e.g., geometries, flow phenomena, etc). Finally, the tank is designed to allow independent pressurization of the liquid pool and the gas reservoir beneath the porous plate. The cost of building this apparatus is estimated at $30,000.

All experimental work has been suspended in response to a request from the U.S. NRC.[10]

Integral analyses have been performed of the continuous gas/film interface expected to occur around the sides of the molten pool above the point at which gas flow into the pool ceases. Results give the film thickness and transverse heat transfer coefficient as functions of the gas properties, local surface inclination angle, and surface mass injection distribution. Expressions for the heat transfer coefficient have been obtained for both laminar and turbulent films at inclination angles ranging from about 30 to 90 degrees (vertical). Analyses of the horizontal pseudo film boiling configuration that gives rise to Taylor instabilities have been performed by Dhir et al.[11] and Alsmeyer et al.[12] These have provided an expression for the interface heat transfer coefficient suitable for application along the bottom of the molten pool. Simulant experiments performed at Kernforschungszentrum Karlsruhe (KfK), Karlsruhe, F. R. Germany, using water over dry ice, suggest that the Taylor instability interface configuration may exist at surface inclination angles up to 20 to 30 degrees.[13] When coupled, the expressions for these various flow regimes provide a model of the core/concrete interface heat and mass transfer around the entire periphery of the pool.

Current efforts are devoted to various aspects of the integral analysis directed toward satisfying objective number 3 above.

Analyses to date have demonstrated that additional experimental insight and data are required before the stability behavior can be further analyzed and before the integral analysis can be confirmed. Since this information was to be obtained from the experimental portion of the study, which has now been suspended, further stability analyses and heat transfer model verification efforts are not presently anticipated.

28

1.4 References

1. D. A. Powers, Molten Core - Concrete Interactions Project Description, Schedule 189 No. A-1019, Sandia Laboratories, Albuquerque, NM, October 1975.

2. Light Water Reactor Safety Research Program Quarterly Report, April - June 1978, SAND 78-1901, Nuclear Fuel Cycle Safety Research Department, Sandia Laboratories, Albuquerque, NM, January 1979.

3. D. A. Powers, et al., Exploratory Study of Molten Core Material/Concrete Interactions July 1975 - March 1977, SAND77-2042, Sandia Laboratories, Albuquerque, NM, February 1978.

4. H. Plein, Sandia Laboratories, Albuquerque, NM, unpublished results.

5. D. A. Powers, Core Meltdown Experimental Review, SAND74-0382, Sandia Laboratories, Albuquerque, NM, August 1975, (Revised March 1977).

6. Light Water Reactor Safety Research Program Quarterly Report, January - March 1978, SAND78-1511, Nuclear Fuel Cycle Safety Research Department, Sandia Laboratories, Albuquerque, NM, October 1978.

7. D. A. Powers, Sustained Molten Steel/Concrete Interactions Tests, A Preliminary Report on the Feasibility of Experimental Techniques, SAND77-1423, Sandia Laboratories, Albuquerque, NM, June 1978.

8. F. G. Blottner and D. E. Larson, Calculation of Real Gas Properties for MHD Channel Flows, SAND78-1361, Sandia Laboratories, Albuquerque, NM, September 1978.

9. D. A. Powers and A. W. Frazier, VISRHO: A Computer Subroutine for Estimating the Viscosity and Density of Complex Silicate Melts, SAND76-0649, Sandia Laboratories, Albuquerque, NM, June 1977.

10. R. Sherry, Fuel Behavior Branch, Division of Reactor Safety Research, Office of Nuclear Regulatory Research, U.S. Nuclear Regulatory Commission, Washington, DC, September 6, 1978, personal communication.

11. V. K. Dhir, I. Catton, and J. Castle, "Role of Taylor Instability on Sublimation of a Horizontal Slab of Dry Ice," Journal of Heat Transfer, Vol. 99, No. 3, August 1977, pp. 411-418.

12. H. Alsmeyer, L. Barleon, J. Koster, I. Michael, V. Miller, and M. Reimann, A Model Describing the Interaction of a Coremelt with Concrete, NUREG/TR-0039 (translation of: KFK 2395, Kernforschungszentrum Karlsruhe, Karlsruhe, F. R. Germany, October 1977), September 1978.

13. M. Reimann, Kerforschungszentrum Karlsruhe, presentation at Sandia Laboratories, Albuquerque, NM, August 16, 1978, unpublished.

2. Steam Explosion Phenomena

2.1 Summary

2.1.1 Efficiency Scaling Studies

Forty field experiments, each involving up to 27 kg metallothermic-reaction-generated mixtures of molten aluminum oxide and iron, have now been performed. Explosions have occurred in 30 of the 40 experiments. Most of the explosions have occurred spontaneously at seemingly random delays from pour initiation. Both single and multiple explosions have occurred and, when multiple explosions occur, one is frequently much more energetic than the others. The spontaneous triggering mechanism is unknown but is strongly suspected to require contact of the melt with the interaction vessel walls or similar surfaces. Coating the interaction vessel walls with lard has recently been shown to reduce significantly the incidence of spontaneous explosions. Explosions can be artificially initiated using high explosive detonators, even when the tank walls are coated with lard.

The largest explosion in these tests converted almost 1% of the melt's thermal energy into work. That estimate is based on the amount of honeycomb crushed, the height the water was blown into the air, and the amount of energy expended in plastically deforming the interaction vessel. Many other experiments have produced explosions for which the conversion efficiency was about 0.5% or less. In estimating the efficiency, the thermal energy of the melt is assumed to be 3.1 kJ/g.

A limited number of direct pressure measurements and other indirect evidence suggests that steam pressures between 5 and 10 MPa lasting several milliseconds are generated during the larger explosions, with narrow spikes of even higher pressures possible.

The debris generated in the field-scale efficiency experiments looks quite similar to the debris produced in the laboratory-scale riggering experiments. Sieve analyses on partial samples of the debris recovered from some of the experiments indicate that the more efficient explosions produce the finer particulate.

The efficiency of the explosions seems to increase as the water depth increases. This is probably caused by a tamping effect (inertial confinement). There is an apparent peak in the plot of explosion efficiency vs the quantity of melt present in the tank at the time of the explosion, but it is not known at this time if the peak is related to actual experimental conditions or if it merely reflects the lack of enough data at the higher melt quantities.

Restricting the interaction volume by inserting smaller cylinders in the bottom of the interaction vessel has caused no significant change in the explosion efficiency. Based on the data from five tests involving hot or boiling (saturated) water, it has been concluded that water temperature does not significantly affect the explosions.

2.1.2 Triggering Studies

During this quarter, matrix variable studies were completed. Experiments were performed with Corium-A simulants at different levels of oxidation; one modest explosion was obtained with the most oxidic composition. A Corium-E simulant was studied as a function of water temperature, and a temperature limit for explosion was identified. The same Corium-E simulant and molten Fe_2O_3 were studied at chamber gas pressures of 1.0 MPa. Explosions were not seen at this chamber pressure. The effect of water additives on the steam explosion phenomena was studied by the use of simulated sea water and borated water. Both molten Corium-E simulant and Fe_2O_3 exploded with apparently little difference from the interactions produced in deionized water.

Several experiments were performed with an electrochemical-evolved gaseous oxygen analyzer to determine the instantaneous composition of the melts at flooding time. The technique was checked against two alternate analyses; all three methods produced essentially identical analyses. The evolved gas analytical technique was applied to two Corium-E and two Fe_2O_3 samples, all four of which exploded. The debris from the two Fe_2O_3 experiments was analyzed by wet chemistry.

The experiments performed this quarter are summarized in . . 2-I.

2.2 Efficiency Scaling Studies (L. D. Buxton and W. B. Benedick)

2.2.1 Introduction

The first 22 efficiency scaling experiments using multikilogram melts generated by a metallothermic reaction were reported in the three previous quarterly reports.[1-3] Eighteen additional experiments of that type are reported here. One of those was performed primarily to continue the investigation of the effect of high-water temperature; it will be discussed in Section 2.2.2. Four more were performed for the purpose of investigating the effect of restricting the interaction zone; they will be discussed in Section 2.2.3. Section 2.2.4 will contain the details on two tests for which the intent was to investigate the effect of a highly increased pour rate. Artificial triggering and/or the use of lard coatings as a spontaneous trigger elimination method were the primary motivations for the rest of the 18 tests; they will be discussed in Section 2.2.5.

The debris recovered from the interaction vessel after 23 of the tests has been subjected to a limit sieve analysis; the results will be presented in Section 2.2.6. Pressure histories obtained using lithium niobate transducers immersed in the water during two of the recent tests will be discussed in Section 2.2.7.

TABLE 2-I

Summary of Results of Triggering Experiments[a]

Starting Material	Experiment No.	Sample Weight (g)	Water Temperature (K)	Argon Pressure (MPa)	Melt Temperature (K)	Transient Generation	Delay Time (s)	Flash X-Ray	High-Speed Photos	Remarks
Oxidic Corium-A[a]	10-92-1	14.92	298.8	0.083	2355	BW	0.162	3	400	No fragmentation. Heat exchange tubing in chamber.
	10-92-2	15.03	298.2	0.083	2098	BW	0.265	3	400	
	10-93-1	15.02	307.1	0.083	1986	BW	0.389	3	400	
	10-93-2	15.04	298.2	0.083	NM	BW	NM	3	NM	
	10-93-3	14.93	302.5	0.083	1706	BW	0.164	3	400	
	10-94-1	14.96	304.5	0.083	1950	BW	0.271	3	400	Modest fragmentation. Heat exchange tubing in chamber.
Oxidic Corium-A[b]	10-95-1	15.04	310.7	0.083	1850	BW	0.193	NM	400	No fragmentation
	10-95-2	15.04	300.2	0.083	2000	BW	0.233	NM	400	No fragmentation
	10-96-1	15.03	298.9	0.083	NM	BW	0.378	NM	400	Large spherules and irregular rounded masses
	10-96-2	14.97	300.8	0.083	NM	BW	0.142	NM	400	No fragmentation
	10-97-1	15.01	297.6	0.083	1799	BW	0.449	NM	400	Flat pieces and large spherules
	10-97-2	15.08	299.4	0.083	1699	BW	0.301	NM	400	No fragmentation
Oxidic Corium-A[c]	10-98-1	15.05	302.4	0.083	1662	BW	0.197	NM	400	No fragmentation. No sign of phase separation.
	10-98-2	15.11	301.2	0.083	1664	BW	0.308	NM	400	No fragmentation
	10-98-3	14.92	297.3	0.083	1642	BW	0.375	NM	400	No fragmentation. No sign of phase separation.
	10-99-1	15.12	300.2	0.083	1639	BW	0.194	NM	400	No fragmentation. No gross signs of phase separation.
	10-100-1	14.96	298.1	0.083	1818	BW	0.265	NM	400	No fragmentation
	10-100-2	15.00	298.8	0.083	1721	BW	0.389	NM	400	No fragmentation. Phase separation noted.
Oxidic Corium-A[d]	10-101-1	15.06	295.8	0.083	1406	BW	0.192	NM	400	No fragmentation
	10-101-2	15.02	302.3	0.083	1676	BW	0.247	NM	400	No fragmentation
	10-102-1	15.05	301.6	0.083	1767	BW	0.385	NM	400	No fragmentation
	10-102-2	14.97	305.0	0.083	1782	BW	0.166	NM	400	No fragmentation. No sign of phase separation.
	10-103-1	15.14	300.8	0.083	1634	BW	0.297	NM	400	No fragmentation
	10-103-2	15.05	299.3	0.083	1619	BW	0.358	NM	400	No fragmentation. Phase separation noted.

33

TABLE 2-I (cont)

Starting Material	Experiment No.	Sample Weight (g)	Water Temperature (K)	Argon Pressure (MPa)	Melt Temperature (K)	Transient Generation	Delay Time (s)	Flash X-Ray	High Speed Photos	Remarks
Oxidic Corium-E[b]	10-103-1	15.00	359.0	0.083	1941	BW	0.237	NM	400	Single flat piece. Heat exchange tubing in chamber.
	10-104-2	14.95	352.4	0.083	1972	BW	0.196	NM	400 }	No fragmentation. Heat exchange tubing in chamber.
	10-105-1	15.00	343.2	0.083	NM	BW	0.277	NM	400 }	
	10-105-2	15.01	336.4	0.083	1948	BW	0.215	NM	400	Coarse fragmentation. Heat exchange tubing chamber.
	10-106-1	15.06	330.6	0.083	1946	BW	0.306	NM	400	No fragmentation. Heat exchange tubing in chamber.
	10-106-2	14.96	322.6	.083	1946	BW	0.314	NM	400	Fairly coarse fragmentation. Heat exchange tubing chamber.
Fe_2O_3	10-107-1	14.68	298.6	.083	1770	BW	0.176	NM	400	Simulated sea water. Very fine fragmentation.
	10-107-2	15.01	297.7	0.083	1755	BW	0.167	NM	400	Simulated sea water. Fine fragmentation.
	10-109-1	14.96	300.4	0.083	2155	BW	0.225	NM	400	Borated water. Fragmentation.
	10-110-1	15.02	290.6	0.083	NM	BW	0.214	NM	400	Borated water. Fine fragmentation.
Oxidic Corium-E[b]	10-108-1	14.96	298.4	0.083	1755	BW	0.205	NM	400	Simulated sea water. Fine fragmentation.
	10-109-2	15.01	295.2	0.083	1872	BW	0.194	NM	400	Simulated sea water. Fragmentation.
	10-111-1	15.04	295.3	0.083	NM	BW	0.227	NM	400	Borated water. Fragmentation.
	10-113-1	14.93	292.0	0.083	NM	BW	0.191	NM	400	Borated water. Fragmentation.
Oxidic Corium-E[b]	10-115-1	15.00	300.4	0.10	1657	BW	0.973	NM	400	No fragmentation
	10-115-2	15.04	299.1	0.10	NM	BW	0.940	NM	400	No fragmentation
Fe_2O_3	10-114-1	14.96	305.2	0.10	NM	BW	0.939	NM	400	No fragmentation.
	10-113-2	15.08	293.3	0.083	NM	None	-	NM	400	Oxygen evolution/weight loss test. No fragmentation.

---

[*] Common to all experiments - Water amount 1.5 litres
             - Melt atmosphere argon

[a] 64.2 at. % initial oxygen content

[b] 61.5 at. % initial oxygen content

[c] 58.7 at. % initial oxygen content

[d] 55.9 at. % initial oxygen content

Table 2-II contains a summary of the test parameters and results from all 40 tests performed thus far. Most of the information for the first 22 tests is merely repeated from the previous quarterly reports for completeness, but an important quantity not previously shown is the quantity of melt estimated to be in the interaction vessel at the time of the explosion. It is that value which is used to estimate the thermal-to-mechanical energy conversion efficiencies rather than the total amount of melt initially contained in the generator. This will be discussed further in Section 2.2.8, where the most recent scaling data will be presented.

2.2.2 Water Temperature Effect Test

The THERMITE 22 experiment, reported last quarter,[3] did not produce a spontaneous explosion when the molten iron/alumina mixture was poured into a full tank of saturated water. To test whether that result was reproducible, the test was repeated this quarter as closely as possible. One minor difference in the setup for the two tests was that THERMITE 23 used a slightly taller generator which allowed a larger gas expansion volume above the thermite reactants. The only other difference was that this time a detonator was hung in the tank inside a piece of plastic tubing, the purpose being to try to trigger an explosion after the pour ended if one had not already occurred spontaneously. These changes should not influence the results.

The melt plug did not fail quite as fast in THERMITE 23 as in 22, but it did finally fail and initiate the pour about 29 s after ignition of the thermite reaction. About 1.08 s after the melt plug failed there was a strong explosion, followed by a smaller explosion at 1.78 s after plug failure. Both explosions were spontaneous, thus the detonator was not fired. Almost all of the water was blown out of the tank to an average height of about 5 m. The heaters were also blown out.

The estimated efficiency for THERMITE 3 was 0.24%, which is not exceedingly large, but certainly is not abnormally low when compared   explosion efficiencies for cold-water tests under otherwise similar conditions. Conseq n   the conclusion is that the reasons for not getting an explosion in Test 22 are unknown, but they probably involved a failure to achieve proper triggering conditions rather than diminished propagation behavior due to the saturated water. Figure 2-1 supports that conclusion since no trend toward lower efficiencies is seen for the hot- or boiling-water tests compared to the cold-water tests.

2.2.3 Interaction Volume Restriction Tests

From one point of view, the previously reported tests studying the effect of low water levels were inter   volume restriction tests. The four interaction volume restriction tests performed this quar   a little different, however. They employed ring baffles (pipe sections), tack-welded to the bottom of the interaction vessel to simulate using smaller tanks and larger length/diameter ratio tanks. Two different sized baffles were used for the four tests; one was 460 mm in diameter by 460 mm tall and the other was 310 mm in diameter by 380 mm tall. In both cases the volume of water contained in the ring was still considerably larger than the volume of the melt (the volume of the unreacted standard charge of mixed powders, 13.6 kg, is approximately one-fourth of the volume of the smallest pipe section used).

TABLE 2-II

Summary of Efficiency Scaling Experiments

Experiment No.	Primary Test Purpose	Quantity Water (kg)	Water Temperature (K)	Quantity Melt (kg)	Diameter Pour (mm)	No. Explosion	Time to Explosion (s)	Efficiency (%)	Remarks
1	Melt Generator	840	300[a]	1.0	-	0	-	-	Paint can generator
2	Melt Generator	840	300[a]	3.0	12.7	0	-	-	Power's generator
3	Melt Generator	320	300[a]	6.3	25.4	0	-	-	Cortran insulation
4	Melt Generator	270	300[a]	13.6	25.4	0	-	-	Generator meltthrough
5	Melt Generator	200	300[a]	3.0	28.6	1	1.00	.05	Greencast insulation
6	Melt Generator	200	300[a]	3.6	35.0	4	0.60	.05	Larger pour hole
7	Water Level	200	300[a]	3.5	50.8	1	1.10	.21	Honeycomb first used
8	Water Level	420	300[a]	9.2	50.8	3	1.75	.11	Half tank water
9	Water Level	840	300[a]	6.6	50.8	1	2.20	.41	Bent baseplate
10	Water Temperature	250	320	3.0	50.8	1	0.95	.23	Warm water
11	Water Temperature	550	357	3.4	50.8	1	1.00	.00	Hot water
12	Trigger Elimination	200	300[a]	2.0	50.8	1	0.50	.13	Sandblasted cover
13	Water Temperature	400	369	4.4	50.8	2	1.48	.26	Saturated water
14	Trigger Elimination	175	300[a]	2.0	50.8	1	0.41	.08	Waxed cover
15	Pour Rate	840	300[a]	5.0	76.2	1	1.27	.96	Bottom blew out
16	Trigger Elimination	175	300[a]	3.5	50.8	1	1.31	.07	Epoxy painted cover
17	Trigger Elimination	840	300[a]	3.4	50.8	2	0.41	.05	Single screen, 6 in. down
18	Trigger Elimination	840	300[a]	7.6	50.8	1	2.78	.21	Two screens, 12 in. & 18 in.
19	Trigger Elimination	840	300[a]	4.1	50.8	2	0.55	.10	Single screen, flush
20	Trigger Elimination	840	300[a]	5.0	50.8	2	1.63	.36	Splatter plate
21	Trigger Elimination	560	300[a]	6.2	50.8	2	1.27	.18	1/2 in. Melt plug
22	Water Temperature	780	366	12.5	76.2	0	-	-	Long heaters

TABLE 2-II (cont)

Experiment No.	Primary Test Purpose	Quantity Water (kg)	Water Temperature (K)	Quantity Melt (kg)	Diameter Pour (mm)	N. Explosion	Time to Explosion (s)	Efficiency (%)	Remarks
23	Water Temperature	820	368	6.9	76.2		1.08	.24	Repeat of T-22
24	Geometry	820	300[a]	13.6	50.8	0		-	15 in. x 18 in. Baffle
25	Geometry	820	300[a]	5.4	50.8	1	7	.47	Repeat of T-24
26	Geometry	820	300[a]	7.4	50.8	1	?.	.18	2 in. x 15 in. Baffle
27	Artificial Triggering	820	300[a]	4.2	76.2	1	.1	.42	SE1 detonator trigger
28	Artificial Triggering	820	300[a]	5.5	76.2	1	1.30	.46	Spontaneous before det
29	Artificial Triggering	820	300[a]	3.4	76.2	1	0.32	.47	First pressure traces
30	Artificial Triggering	820	300[a]	3.2	76.2	1	0.95[b]	.6	Clear analog pressure traces
31	Pour Rate	820	300[a]	10.0	200.0	1	2.52	.25	First 8 in. pour attempt
32	Geometry	300	300[a]	5.7	76.2	3	.78	.12	12 in. x 15 in. Baffle, low water
33	Pour Rate	820	300[a]	27.2	200.0	0	-	-	Fast pour, no explosion
34	Trigger Elimination	200	300[a]	13.6	50.8	0	-	-	Lard-coated cover
35	Trigger Elimination	820	300[a]	12.0	76.2	1	3.34[b]	.20	Lard, det triggered
36	Trigger Elimination	820	300[a]	13.6	76.2	0	-	-	Melt plug abort
37	Trigger Elimination	820	300[a]	13.6	50.8	0	-	-	Lard, late pour
38	Trigger Elimination	820	300[a]	13.0	76.2	1	3.45[b]	.19	Lard, digital pressure traces
39	Trigger Elimination	820	300[a]	6.0	76.2	1	1.55	.51	Lard, spontaneous trigger
40	Trigger Elimination	820	300[a]	5.5	76.2	3	1.38	.59	Lard, spontaneous trigger

[a] Approximate; ambient conditions determine exact temperature.

[b] Artificially triggered.
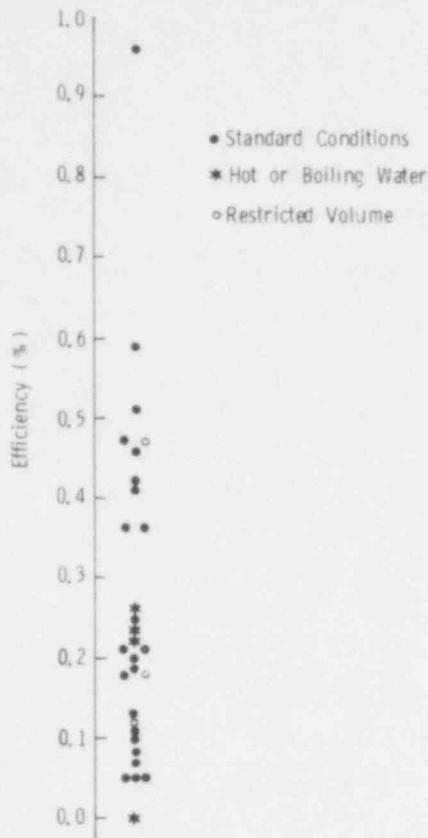
Figure 2-1. Explosion Efficiency vs Conditions of Test

THERMITE 24 used the larger volume ring baffle. The interaction tank was completely filled with water to provide additional tamping of the interaction over that which would be provided by just the water inside the ring. However, this also provided a geometry in which the melt could be coarsely fragmented by Weber breakup before the pour stream reached the restricted volume and might even fall to the bottom of the vessel outside the baffle region. It was observed after the test that such a diversion did not occur, at least to any large extent. Unfortunately, there also was no explosion in THERMITE 24. There was fragmentation of the melt, generation and burning of hydrogen at the water surface, and slow boiloff of about 20 kg of water, but no energetic event. A large amount of fine black material, like soot, was found both in the debris and inside the generator after this test. This had not been seen previously and has not been seen since; the origin and possible effect on the experiment are unknown.

THERMITE 25 was a repeat of the THERMITE 24 test just discussed. The only differences in the two tests were that a 6.4-mm-thick melt plug was used in Test 25 instead of the 12.8-mm-thick plug used in Test 24 and a detonator was hung in the tank inside a piece of tubing for Test 25. Neither of these two changes would be expected to alter the test results. As in Test 23, the intentions were to fire the detonator after the pour finished if an explosion had not occurred already.

From the films of Test 25, it can be seen that, again, there are flames on the water surface immediately after melt/water contact was initiated. This was followed by a single large explosion

which occurred spontaneously 1.97 s after melt plug failure. About 620 kg of water and debris were blown approximately 6 m into the air. The spot welds holding the ring baffle were broken loose and a vertical seam in the pipe section was broken. This suggests that the explosion did occur inside the restricted region. The estimated thermal-to-mechanical energy conversion efficiency for this test was determined to be 0.47%. That value is perhaps a little high since the pour rate determined by timing the total pour seems low compared to other tests using the same diameter melt plug.

The THERMITE 26 experiment was similar to Tests 24 and 25 except the smaller pipe section mentioned earlier was used to further restrict the water volume immediately accessible to the melt. Again, the tank was filled completely with water to provide strong tamping. As seen in many of the other tests, there were lots of flames visible on the water surface soon after melt/water contact was initiated. A single explosion occurred 2.48 s after the melt plug failed in this experiment. The explosion sounded sharper than some of the previous explosions in the opinion of those observers present, but it was only average in efficiency (0.18%) compared to other tests in the series. Streaks of filigree material on the inside of the ring baffle indicated that at least part of the explosion was inside the ring, but some filigree material was also recovered from outside the ring. The tack welds were broken loose but there was no obvious deformation of the pipe section itself.

The final interaction volume restriction test in this series, THERMITE 32, was essentially a repeat of Test 26 except this time the initial water level was only at the top of the restrictive ring rather than having the whole tank full. One other difference which could have some significance is that THERMITE 32 had a 76.2 mm diam pour hole instead of a 50.8 mm one as in the previous volume restriction tests.

There were three separate explosions in THERMITE 32. The first one occurred 0.78 s after melt plug failure. The second explosion, which was the largest one, occurred 1.25 s after plug failure. The third explosion was at about 1.38 s. It did not occur down in the tank, but instead near or at the bottom of the melt generator. Apparently some water blown out of the tank in the second explosion was blown into some melt still pouring from the generator. The efficiency estimate for this experiment was only 0.12%. The lack of good inertial confinement by a large head of water is probably partially responsible for the low value.

The efficiencies for the restricted volume tests are compared to the rest of the tests in Figure 2-1. As indicated, there is no apparent increase in efficiency for restrictions of this size. The data for this series of tests are distributed fairly uniformly among the other data. This might not hold if the interaction volume was shrunk even further, of course.

2.2.4 Pour Rate Effect Tests

As indicated in Table 2-II, most of the tests previously reported and a few of the tests performed this quarter have used 50.8 mm diam pour holes. Most of the tests performed this quarter have used 76.2 mm diam pour holes in an attempt to get somewhat larger quantities of melt into the interaction tank before an explosion occurred. Since pour rate was not the primary motivation for performing those tests, they will be discussed elsewhere. Two tests in which very large pour rates were attempted were THERMITE 3. and 33. Both tests involved trying to use the whole bottom plate of the melt generator as a melt plug. A 0.2 m diam circular groove about 6 mm deep was cut in the bottom side of the 12.7-mm thick bottom plates. If the melting of the uninsulated plate is assumed to be uniform over the whole area, the groove should force the plate to fail at the outer radius before the center fails.

From the slow speed movies of Test 31, it can be seen that the pour obviously did not proceed as quickly as intended. The pour was slow for about 1.8 s after initial failure and then was observed to increase somewhat. There was a single explosion about 2.52 s after initial plug failure. The pour was still in progress at that time, so it was assumed that about 10 kg of the original 13.6 kg of melt was actually in the tank at the time of the explosion. This corresponds to a pour rate of only about 4 kg/s. The melt plug did ultimately separate from the generator, but inspection of it suggests that it was still attached at a couple of points before the explosion and was then blown loose in the explosion. The complete generator was torn loose from its tiedown brackets and blown about 6 m into the air in this test. The tank was also plastically deformed somewhat but, because of the large quantity of melt assumed to be involved in the explosion, the efficiency estimate was only 0.25%.

For THERMITE 33, the amount of mix placed in the generator was doubled from the normal load used with the thought that the additional 13.6 kg might apply enough additional force on the melt plug to cause the hole to open faster and more completely. All other aspects of the test were the same as for Test 31.

From the movies, it can be seen that there was a lot of material blown out the vent pipe as the chemical reaction proceeded. It is assumed this was caused because the insulation on the generator walls was contaminated with a lubricant used to facilitate one step in building the generator. No estimate was made for the amount of melt material blown out. The films suggest that the pour hole opened faster than in Test 31 but inspection of the generator indicated only a large hole on one side with the other side intact. There was no explosion in this test. Lots of flames on the water surface were visible as the pour progressed and the water was seen to be in motion after the pour ended, presumably because of heavy boiling at the bottom of the tank. (The water was quite hot to the touch several minutes later but the temperature was not measured.) The total pour time was about 4.1 s, which implies a pour rate of about 6.6 kg/s. This is large but still not as large as desired.

467 230

40

No explanation is immediately available for failure to trigger an explosion in THERMITE 33. It could be related to the larger amount of melt, which might have caused more vigorous local boiling and reduced the chances for an entrapment-based trigger. It could also have to do in some peculiar fashion with the lubrication contaminant in the generator. The test will not be repeated with this design of the pour hole opening, however, since neither of the two fast-pour tests have worked properly. A new design will be developed.

Although very large pour rates have not yet been achieved, it is still important to see whether the limited range studied has had any effect on explosion efficiencies. Figure 2-2 shows the efficiency of each of the explosions to date as a function of the average estimated pour rate. There does not appear to be any correlation in the data but there could be a very large error in almost any of the indicated rates because of the way in which they were estimated (usually by timing complete pours and assuming that the explosions did not directly affect the pours).
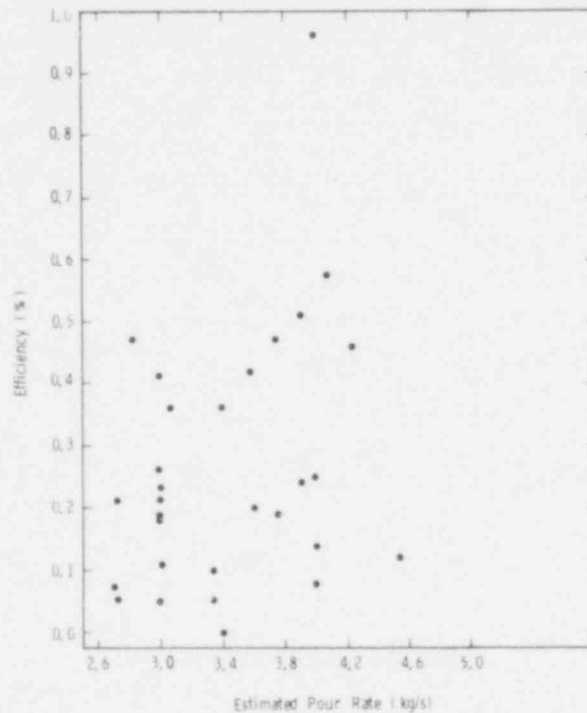
Figure 2-2. Explosion Efficiency vs Estimated Pour Rate

2.2.6 Artificial Triggering and Triggering Elimination Tests

Because of the almost random occurrence of the spontaneously triggered explosions in the large-scale open geometry tests, development of proper instrumentation techniques for the closed geometry, highly instrumented tests to follow this series is difficult. Several tests were performed this quarter to investigate the possibility of artificially triggering these large explosions in a manner similar to that used in the laboratory studies (see Section 2.3) by applying an impulsive

pressure transient to the system. The method selected was to fire an SE1 detonator in the water near the bottom of the tank. The detonator was encased in plastic tubing to keep it dry. The chemical energy release from the explosion of one of these detonators is about 3.6 kJ, which is only slightly more than the thermal energy assumed to be in 1 g of melt.

For the tests in which artificial triggering was attempted, the pour hole diameter was increased to 76.2 mm so that more melt could get into the tank before artificial triggering was attempted. The tank was also completely filled with water in the tests in an attempt to delay any spontaneous initiation as long as possible. This was suggested by the plot of explosion efficiency vs pour time to first explosion shown in Figure 2-3. As shown there, many of the spontaneous explosions have occurred prior to 1 s of pour time, but further investigation revealed that all of those tests involved low water levels or screens in the tank. This observation supports the assumption made in the early trigger elimination tests that the spontaneous triggering involves the melt coming into contact with the tank bottom, walls, or similar surfaces. Therefore, it was assumed for these artificial triggering tests that if the detonator was fired at about 1 s after pour initiation, the chances of not having already had a spontaneous explosion would be high.

Figure 2-3. Explosion Efficiency vs Pour Time
to First Explosion

42

467 232

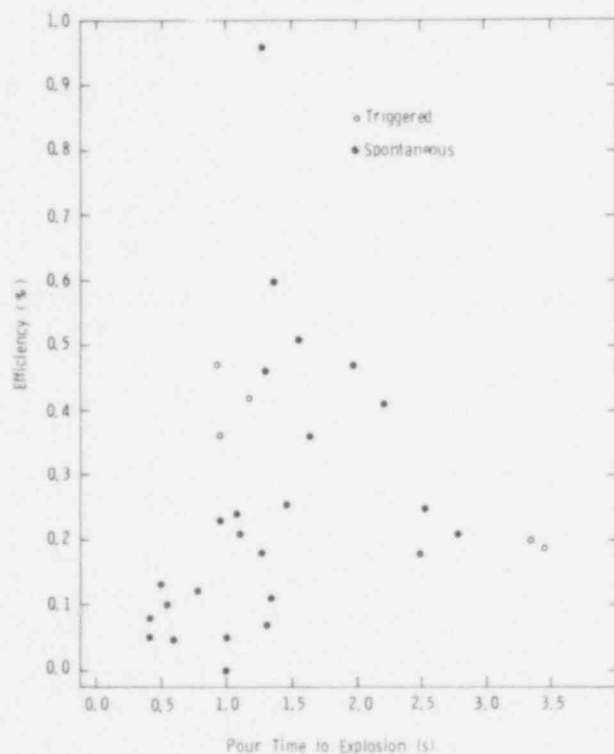THERMITE 27 was the first test of artificial triggering. In that test, as in all of the tests, the experiment was observed in real time by remote-control television. When the pour was seen to begin, a manual count of 1 s was performed and a butt⸱, was then pressed to fire the detonator. Apparently coincidental with the firing of the det⸱ ⸱.or, there was a large explosion which blew water and debris about 6 m into the air. From the low-speed movie of this experiment, the explosion was timed as starting about 1.17 s after plug failure. In the high-speed movie, a light flash is seen in the plastic tubing which extends outside the tank. Within a few milliseconds of that flash, the motion of the upper water surface begins. This strongly suggests that the detonator did initiate the explosion. The explosion efficiency estimate for this test was 0.42%. The detonator chemical energy was neglected in this estimate, but if it were subtracted the estimated efficiency would be about 0.39%.

THERMITE 28 was an attempt to repeat THERMITE 27 exactly, but in this test the melt plug failed very late, about 50 s after ignition. Because of this, the shot was temporarily assumed to be an abort and when the pour finally started we were caught unaware and did not fire the detonator at the selected time. A single explosion then occurred spontaneously 1.30 s after plug failure. It was estimated to be 0.46% efficient.

THERMITE 29 was another attempted repeat of THERMITE 27. The only modification for Test 29 was that pressure transducers were put into the interaction vessel with the recording equipment designed to start on the detonator firing gnal. This time the plug failure timing was more normal and the detonator was fired manually about 1 s after plug failure. Again, there was a large explosion that seemed to coincide with the firing of the detonator. From the low-speed movie the explosion was seen to start about 0.92 s after the pour initiated. In the high-speed movie, the flash of the detonator is seen in the tube, followed a few milliseconds later by motion of the water surface. The efficiency of this explosion was estimated to be 0.47%. Pressure traces were obtained on the analog scopes for this experiment, but they were not very clear since the oscilloscopes were not set up to record properly the high frequency signals which were actually generated.

Although the proof of the ability to trigger large-scale explosions artificially was quite convincing after Test 29, the test was repeated again in THERMITE 30 in an attempt to get better quality pressure traces. The oscilloscope settings were improved and a time delay was also built into the circuit so that the scopes would trigger 4 ms before the detonator was fired, assuring a clear recording of the initial portion of the trace. Everything worked as intended this time, with an explosion being initiated 0.95 s after melt plug failure. The pressure traces obtained in this test will be discussed in Section 2.2.7. The estimated efficiency for THERMITE 30 was 0.36%.

Following the verification of the ability to trigger large-scale explosions artificially, efforts to eliminate the unknown spontaneous triggering mechanism were renewed. As discussed earlier, it still seemed highly probable that the trigger involved contact of the melt with some surface. Since the grease coating which was used in Test 14 was really more like a wax and the epoxy paint

was later found to have been penetrated in Test 16, a decision was made to try a highly volatile hydrocarbon coating on the tank walls under the assumption that any hot melt contacting the walls would immediately vaporize the hydrocarbon, pushing the melt away. Since most commercially available lubricants contain additives to prevent vaporization and decomposition, the hydrocarbon material chosen for use was plain lard.

As in the earlier trigger elimination tests, an inverted tank cover was used as the interaction vessel for the first test using a lard coating on the walls. A layer of lard about 6 mm thick was smeared on the inside of the inverted tank cover in THERMITE 34 and the cover was filled with water. The cover was mounted above the interaction tank as described in Reference 2. For comparison with earlier test results, a melt generator with a 50.8-mm-diam pour hole was used.

When the melt contacted the water, there were lots of flames as usual, and one minor interaction which gave off a puff of orange smoke, but there was no explosion. The pour ended at about 3.6 s after plug failure and the flames continued to burn until a detonator was fired at 5.4 s after plug failure. Even the detonator did not trigger an explosion but it was fired quite late, probably after enough time for at least a surface layer of the melt to have frozen. The water in the lid was boiling vigorously when the apparatus was approached several seconds later.

Since the lard coating had apparently prevented a spontaneous explosion in Test 34 with the cover as the interaction tank, coating the regular tank with lard was tried for THERMITE 35. The lard coating on the bottom of the tank was made 5- to 10-mm thick and only a thin layer was put on the walls. The tank was filled with water and a generator with a 76.2-mm-diam pour hole was used. An SEI detonator was hung in the tank for this test so that an artificial initiation could be attempted late in the pour if one had not occurred already. Slightly more than 3 s from initial plug failure was chosen as the time to fire the detonator since no spontaneously triggered explosions had occurred that late (see Figure 2-3) and the pour usually ended a little after that time.

The lard coating worked as expected in THERMITE 35; there was no explosion until the detonator was fired at 3.34 s after pour initiation. Again, the high-speed movies verify that it was not merely a spontaneously triggered explosion which happened about the time of the detonator firing. The estimated efficiency of the explosion was 0.20%, assuming that 12 kg of melt was in the tank at the time of the explosion.

The following test, THERMITE 36, was supposed to be a repeat of Test 35 to obtain more data on larger melt quantity explosions. Unfortunately, the melt plug never failed in this experiment so no data were obtained. THERMITE 37 was another attempted repeat of THERMITE 35, except the melt generator with the 50.8-mm pour hole was used. The melt plug failed this time but extremely late, about 2 min after ignition of the thermite mix. Because of the late plug failure, it was assumed the pour had aborted so the detonator was possibly fired too late. No explosion occurred when it finally was fired. Both films had run out by the time the pour began, so no information is available on actual timing of the detonator firing.

After one complete abort and one near abort of the melt plug system, it was decided that the buildup of slag in the bottom of the generator was causing the majority of the melt to be held away from the plug area and thus the heat flow to the melt plug was too small. To solve this problem, the generator was totally rebuilt so that the insulation layer on the bottom plate surrounding the pour hole was only 10 to 20 mm thick.

THERMITE 38 used this new generator in another attempted repeat of THERMITE 35. This time the generator worked as intended, with the melt plug failing and initiating the pour about 9.1 s after ignition of the mix. The lard apparently worked again to prevent a spontaneous explosion. The detonator was fired at 3.45 s, just as the pour was ending, and it did initiate an explosion. The efficiency was estimated to be 0.19% based on 13 kg of melt. Pressure traces were obtained in this test also as will be discussed in Section 2.2.7.

Tests 39 and 40 were both attempted repeats of the lard-coated tank test with a detonator to be fired at late times, but both had spontaneous explosions as shown in Table 2-II. It is assumed that some melt got inside a transducer bracket or on some other surface with not enough lard coating since the coating seemed to work as intended in four previous tests.

2.2.6 Debris Sieve Analysis Results

The debris from 23 of the earlier tests has been subjected to limited sieve analyses. Because only a small fraction of the total melt is usually recovered from the interaction tank, a really accurate analysis cannot be performed. Also, all recovered debris larger than 4.75 mm in diameter was excluded from the analysis in an attempt to make the comparisons more meaningful. Most of the results are based on a representative 100-g sample of debris, but less material was available from a couple of the tests. Sixteen sieve cuts were used in determining the particle size distributions, the smallest sieve being a No. 325, which has $45-\mu$m openings.

Figure 2-4 is a plot of explosion efficiency vs mean particle size obtained from the individual sieve analyses. Data for experiments in which fragmentation but no explosion occurred are also shown. As indicated in the plot, there is a general trend toward smaller particles as the explosion efficiency increases. The mean particle diameter is about 2500 μm when there is no explosion or only a weak one. The mean particle size of the debris is closer to 300 or 400 μm for the more efficient explosions. No debris was recovered from the most efficient explosion, THERMITE 15, since the bottom of the tank blew out in that test.
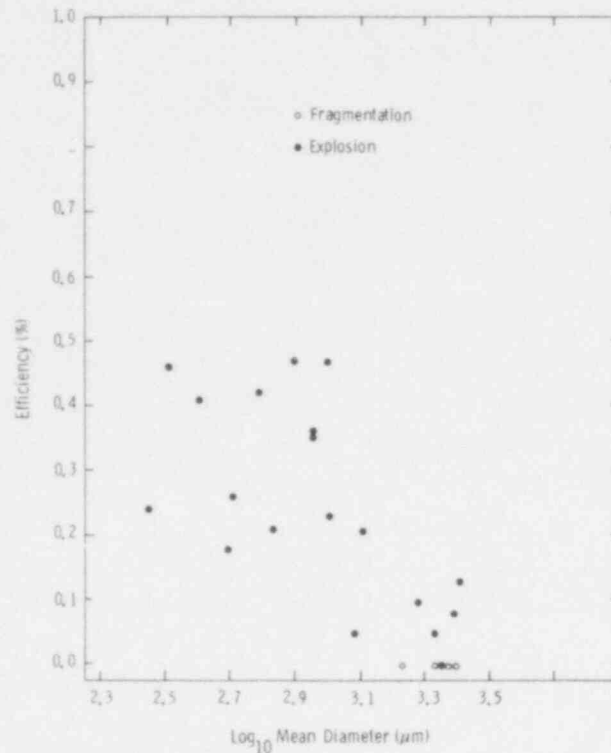
Figure 2.4. Explosion Efficiency vs Mean Particle Diameter

2.2.7 Pressure Histories

By using artificial triggering for the explosions, it became considerably easier to perform active diagnosis of the explosions since high-speed, short-duration recording equipment such as oscilloscopes could be properly initiated. As mentioned earlier, pressure traces have been obtained in three experiments, but they were washed out at early times in one of those. The pressure histories were obtained using the same lithium niobate gages which were used in the laboratory triggering studies.[5] The recording circuit parameters were chosen to produce a signal of about 0.12 V per MPa of applied pressure. The circuit time constant was about 6.7 ms. Two gages were used in each experiment as checks on one another; both were about 120 degrees from the detonator and from each other. They were hung from brackets about 0.3 m above the bottom of the tank and near the wall. The gages were enclosed in a very porous foam and wrapped in tape to give them some thermal protection since they are also pyroelectric. This encapsulation should slightly slow the gage response to fast rise time pulses.

Figure 2.5 shows the signal obtained from one of the pressure transducers in THERMITE 30. The signal was recorded on an analog oscilloscope and then digitized manually. In the plot, it has already been converted from volts to MPa through the appropriate conversion factor. The first spike to 7.5 MPa is caused directly by the detonator. This was verified by an independent test in which a detonator was fired with no melt present. The time delay from firing which is indicated for that initial pulse reflects the transit time of the pulse through the water in the tank. The second spike to about 10 MPa is the result of the steam explosion. The gage signal then "rattles"

around somewhat, but the background pressure still remains substantia¹. Since the natural period of ringing in the tank is at least a millisecond in stagnant water, it is probably even larger in boiling water. Therefore, the pressure spikes which occur for the next several milliseconds are thought perhaps to indicate the incoherency of the interaction on a local scale, even though there is a large measure of coherency to the explosion. The low-magnitude pulses seen at late times may well be reflections of earlier pulses. It should be mentioned that the signals received from the pressure transducers at THERMITE 29 look very similar to the one in Figure 2-5, at least where they are not washed out.
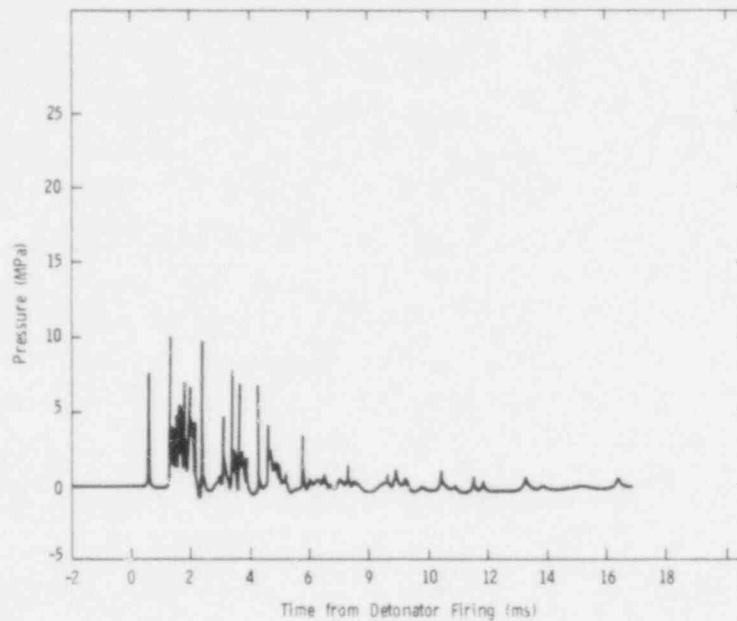
Figure 2-5. Pressure History Recorded During THERMITE 30

Figure 2-6 shows the pressure signature of the explosion in THERMITE 38. It looks less spiky than the THERMITE 30 trace. That is possibly because this particular signal was recorded with a digitizing oscilloscope which effectively takes the average signal in a 5 ns window every 10 µs. Thus, it can easily miss spikes shorter than a few microseconds in duration. Besides being smoother in appearance, this trace also shows no indication of a direct pulse from the detonator. Further, the first pressure increase due to the explosion comes much later in time. Both of these effects are probably caused by the presence of a large amount of boiling water between the detonator and the gages in THERMITE 38. In that test the explosion occurred after quite a lot of melt had a chance to reach the bottom of the tank where the gages and detonator were. The explosion was triggered early in THERMITE 30, and only a small amount of melt, if any, would have reached the bottom.

Figure 2-6. Pressure History Recorded During THERMITE 38

The initial pressure shown in Figure 2-6 probably went higher than indicated since the peak shown corresponds to the full-scale reading of the oscilloscope. Integrating this pulse to get an impulse and applying that impulse to the water slug driven from the tank in THERMITE 38 suggests that the potential energy technique used to estimate the slug's kinetic energy is reason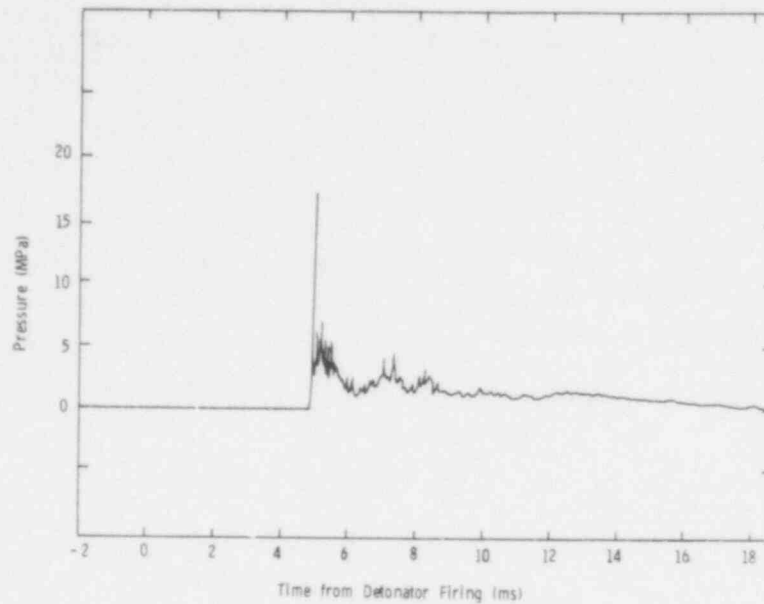ably good. The two agree within a factor of two, with the potential energy estimate on the low side as expected. This is quite encouraging for attempts to design the closed geometry system since several independent pieces of information now indicate that the same range of pressures must be contended with.

2.2.8 Scaling Results

Figure 2-7 indicates the thermal-to-mechanical energy conversion efficiency vs initial water quantity for those 30 tests out of 40 which have produced explosions. About 60% of the tests have been in a full tank of water while the other 40% have had various lower water levels. It is becoming even more evident, as seen in this plot, that the additional water in the full-tank tests does increase the probability of getting a more efficient explosion. This is still thought to be caused by the increased inertial confinement (tamping) of explosions in the bottom of the tank.

Figure 2-8 shows the explosion efficiencies vs the amount of melt estimated to be in the interaction vessel when the last energetic explosion occurred for each experiment. It is not known if the peak in the data around the 6-kg value is related to the amount of iron or alumina in the normal quantity of mix (13.6 kg) used for these tests or if there simply is a lack of data at the higher melt quantities. Additional experiments with large melt quantities will be performed to try to resolve this question.
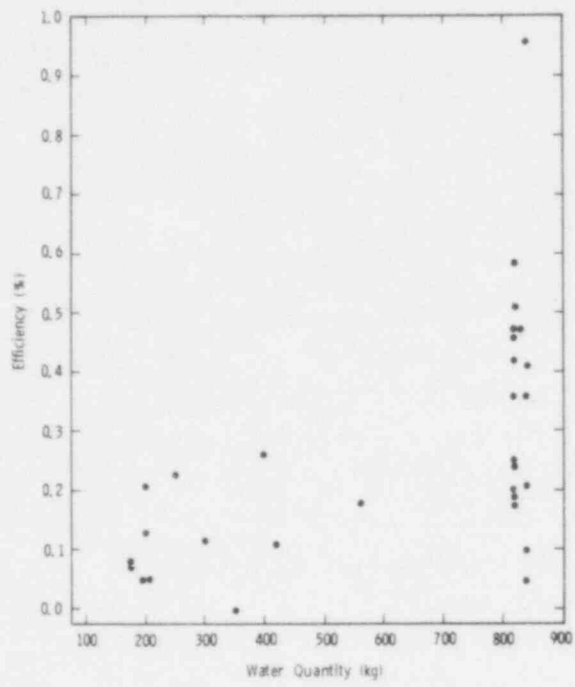
467 238

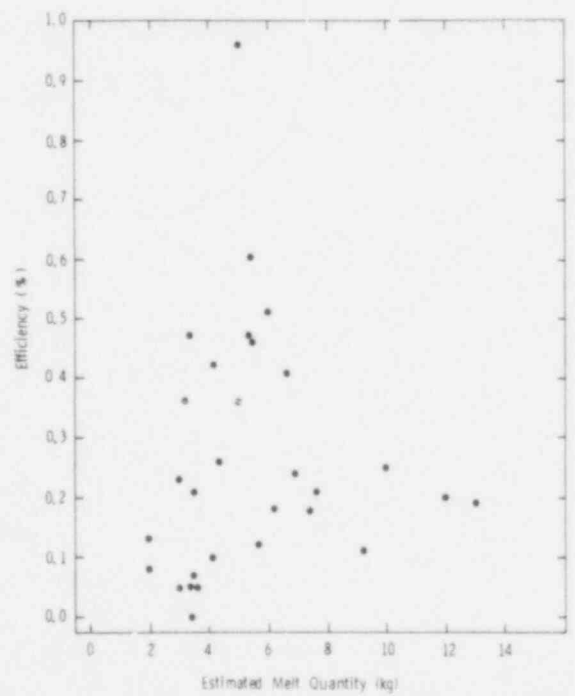Figure 2-7. Explosion Efficiency vs Initial
Water Quantity

Figure 2-8. Explosion Efficiency vs Melt
in Tank at Explosion Time

49

467 240 239

2.3 Triggering Studies (L. S. Nelson)

2.3.1 Matrix Variable Studies

Corium-A Simulants as a Function of Initial Oxygen Content -- A series of experiments was performed with the four-component Corium-A simulants as a function of oxygen content before melting. The initial oxygen contents studied were 64.2, 61.5, 58.7, and 55.9 atomic percent (at.%). Six experiments were performed at each initial oxygen composition (24 experiments in all). Delay times between the start of flooding and the bridgewire pulse were approximately 0.25, 0.35, and 0.45 s. Two experiments were performed at each delay time for each initial composition.

Only one explosive interaction with the Corium-A simulants occurred (10-94-1); this with one of the 64.2 at.% initial oxygen melts. It was in the form of a mild explosion which resembled somewhat the explosions that occur with the Corium-E simulants and the molten iron oxide. A pressure trace recorded during the experiment is reproduced in Figure 2-9. There was one significant difference, however, from the explosive interaction normally observed with the Corium-E simulants and the iron oxide. This was determined from the flash x-ray imaging, in which exposures were taken through the apparatus at 2, 3.5, and 5 ms. No fragmentation was observed in the first two exposures, while modest fragmentation had begun by the third exposure. In the comparable experiments in which molten Corium-E simulants and iron oxide exploded, fragmentation is usually observed in the first two exposures as well as in the third. Thus, for the Corium-A simulant, there was no stage-1 breakup as normally observed with the other two exploding materials. This is consistent also with the absence of a recorded stage-1 pressure pulse, as shown in Figure 2-9. Notice that the pressure-producing event in the Corium-A simulant occurred at about the same time after the bridgewire firing (in the range 3 to 8 ms) as is seen for the stage-2 interaction in the Corium-E simulants and iron oxide.
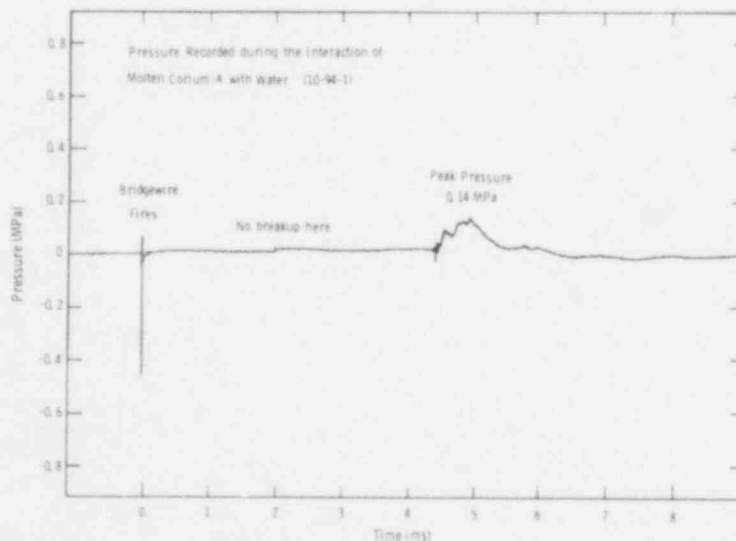
Figure 2-9. Pressure Record of Interaction of Arc-Melted Corium-A
Simulant (64.2 at.% initial oxygen) with Room Temperature
Water. Note absence of stage-1 pulse at ≈ 0.5 ms.

467 240

Corium-E Simulant Interactions with Water at Elevated Temperatures -- In the previous quarterly report, experiments had begun with the heat-exchanger-type water temperature control system; however, the cutoff for explosivity as a function of water temperature was poorly defined for the Corium-E simulant of 61.5 at.% initial oxygen. During this quarter, experiments have been carried further with this Corium-E simulant. It was observed that the highest water temperature at which an explosion could be initiated with this material was 337 K, using bridgewire initiation. Since the boiling temperature of water locally is 368 K, this corresponds to a minimum subcooling of 31 K. This should be compared with the minimum subcooling for the molten iron oxide of 24 K.[3] The main effect of the increase of water temperature (decrease of subcooling) seems to be that the stage-2 interaction (usually the major pressure-producing interaction) gradually diminishes and eventually disappears as water temperature increases. Eventually stage-1 breakup also disappears as water temperature increases. This is shown in Figures 2-10 through 2-14 which show pressure traces for a series of molten iron oxide experiments (with bridgewire initiation) as a function of increasing water temperature.

Figure 2-10. Pressure Record of Interaction of Arc-Melted Fe_2O_3 With 299 K Water (subcooling = 69 K) (10-85-2)

467 241

Figure 2-11. Pressure Record of Interaction of Arc-Melted Fe_2O_3 With 317 K Water (subcooling = 51 K) (10-86-1)
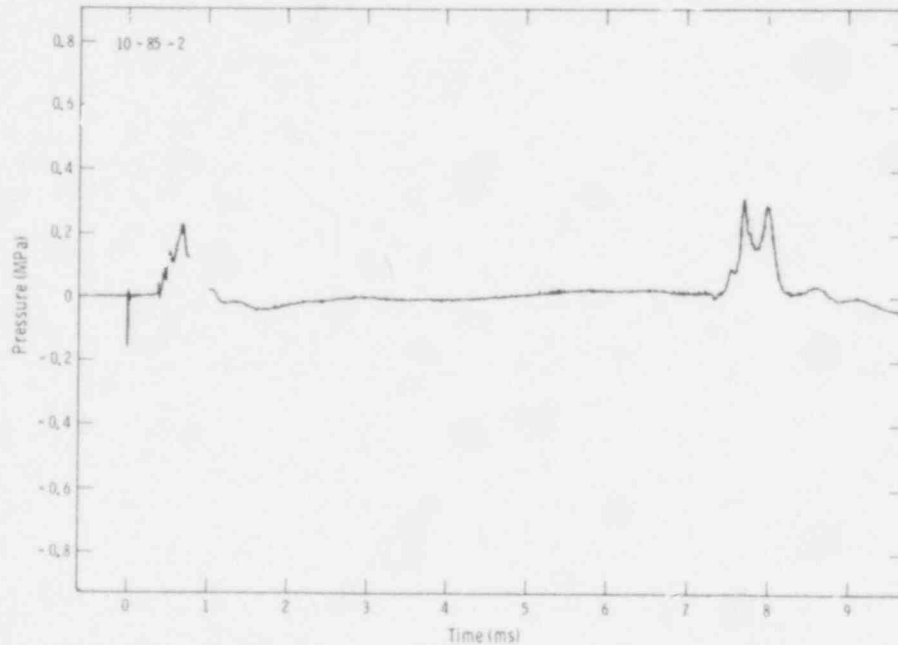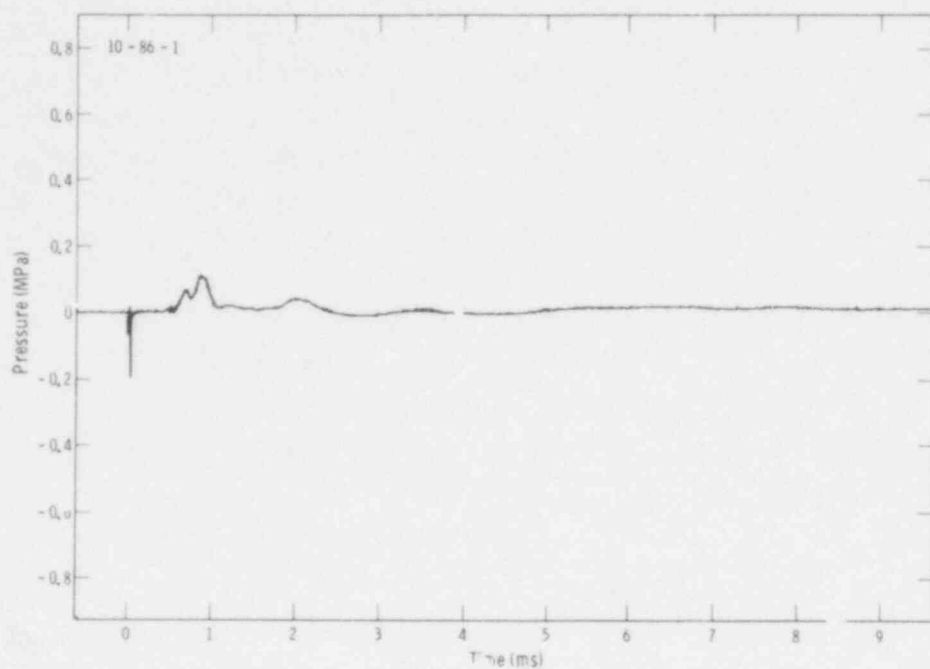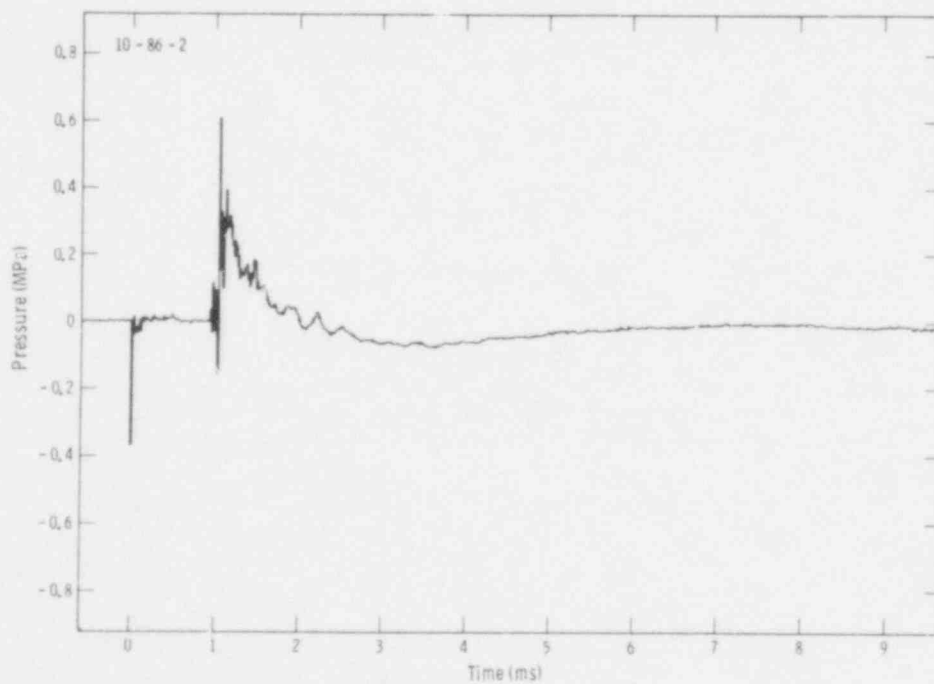

Figure 2-12. Pressure Record of Interaction of Arc-Melted Fe_2O_3 With 327 K Water (subcooling = 41 K) (10-86-2)
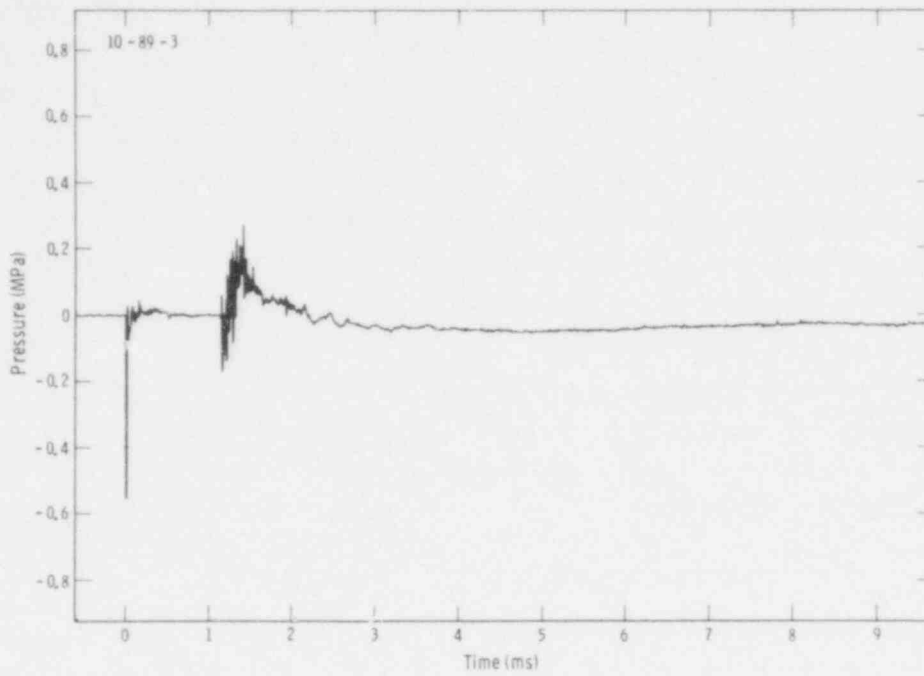
Figure 2-13. Pressure Record of Interaction of Arc-Melted Fe_2O_3
With 343 K Water (subcooling = 25 K) (10-89-3)
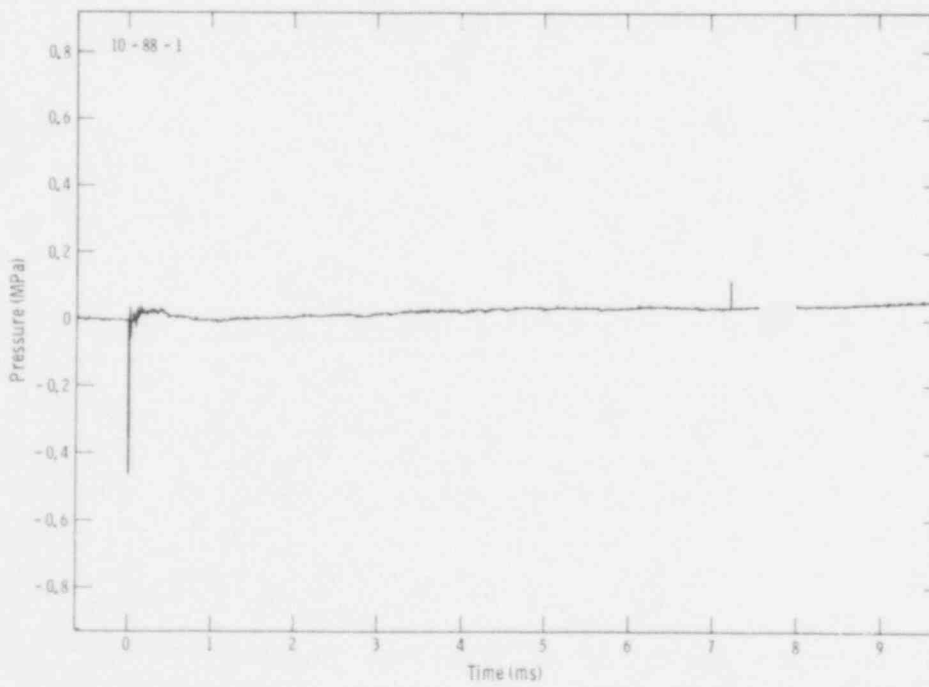
Figure 2-14. Pressure Record of Interaction of Arc-Melted Fe_2O_3
With 364 K Water (subcooling = 4 K) (10-88-1)

Effect of Water Additives -- The effects of water composition on the explosive nature of the interactions in the floodable arc melter were studied for comparison with the deionized water normally used. Two water compositions were used--simulated seawater containing 3.5 wt% sodium chloride,[6] and borated water containing 3000 parts per million of boron by weight as boric acid (simulated chemical shim solution).[7] The two most explosive melt compositions were used-- Corium-E simulant with 61.5 at.% initial oxygen, and molten iron oxide with 60 at.% initial oxygen (Fe_2O_3). The experiments were performed with bridgewire initiation and the most favorable delay time for inducing an explosive interaction (approximately 0.2 s). Two experiments were performed with each melt flooded with each of the two water compositions. Explosions were triggered easily in the eight experiments performed with the modified water compositions. Compared to deionized water, there seemed to be no major differences[*] in the explosive behavior of the melts as indicated by the pressure records, high-speed films, and debris (no flash x-ray images were recorded here, however). Pressure traces recorded in experiments with the water additives are shown in Figures 2-15 through 2-18.
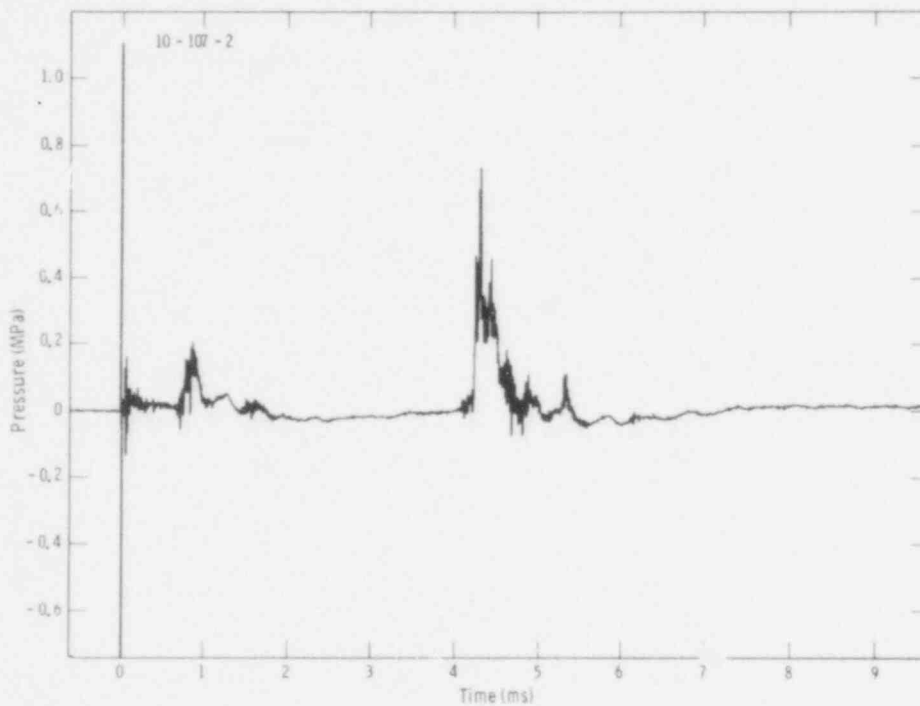
Figure 2-15. Pressure Record of Interaction of Arc-Melted Fe_2O_3 With Simulated Seawater (10-107-2). Note unusually large deflection at bridgewire firing time (t = 0).

---

[*] In the simulated seawater experiments, the bridgewire-generated pressure transient records showed an unusually high peak pressure (off-scale at 3.1 MPa). This was attributed to the increased electrical conductivity of the water due to the added electrolyte. It is assumed that this somehow increased the efficiency of the capacitor discharge through the bridgewire, which is not isolated electrically from the water. The peak bridgewire pressures were normal (< 1.0 MPa) in the borated water experiments.
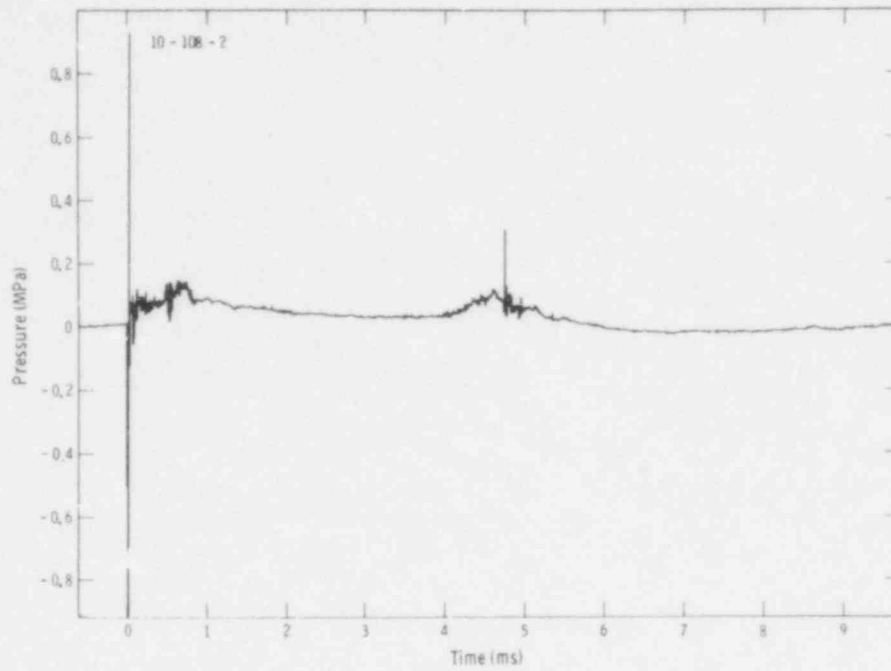
Figure 2-16. Pressure Record of Interaction of Arc-Melted Corium-E Simulated (61.5 at.% initial oxygen) With Simulated Seawater (10-108-2). Note unusually large deflection at bridgewire firing time (t = 0).
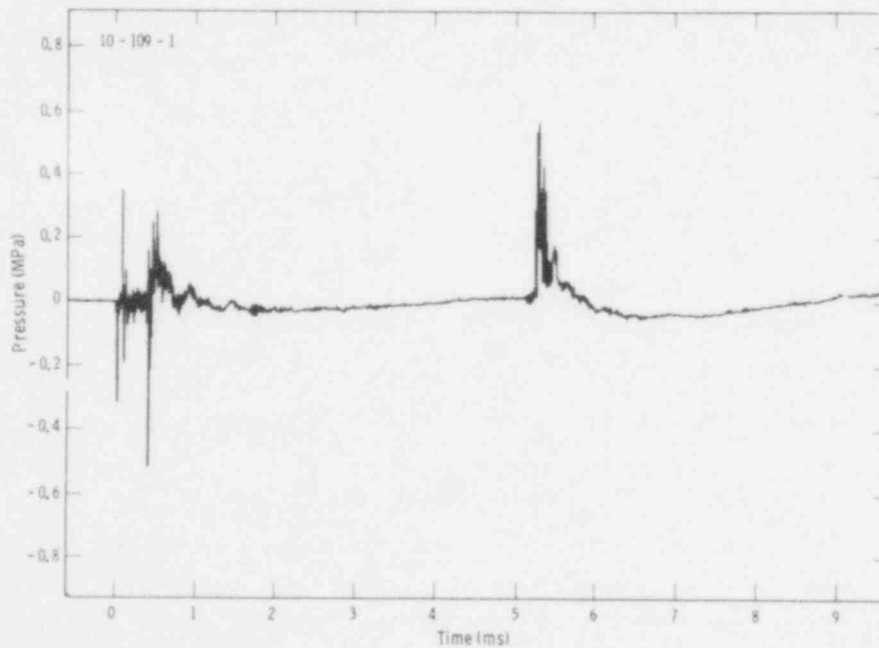
Figure 2-17. Pressure Record for Interaction of Arc-Melted Fe_2O_3 With Borated Water (10-109-1).
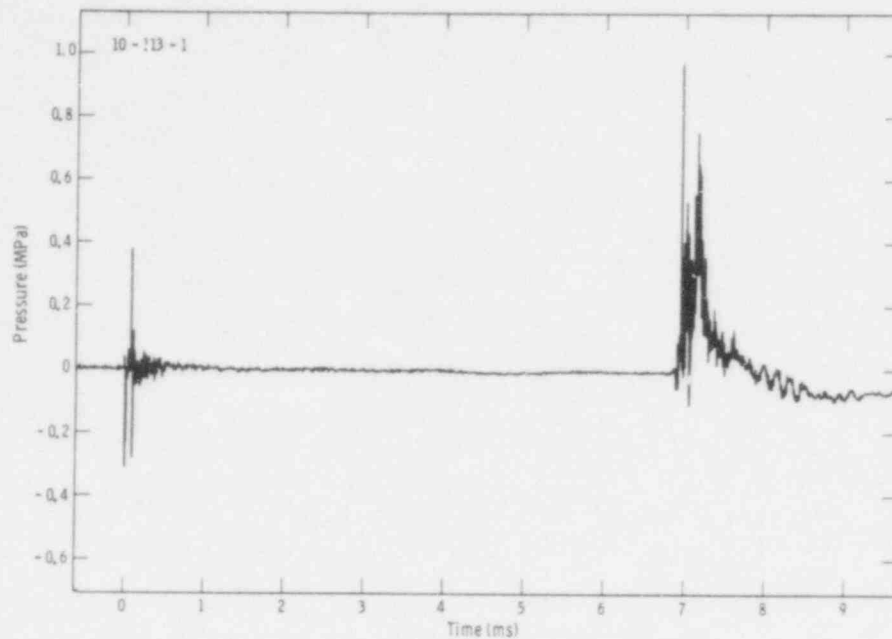
Figure 2-18. Pressure Record for Interaction of Arc-Melted Corium-E Simulant (61.5 at. % initial oxygen) With Borated Water (10-113-1).

Effects of Elevated Chamber Pressures -- In previous experimentation, the maximum chamber pressure studied was 0.75 MPa. During this quarter, experiments were performed with Corium-E simulants of 61.5 at. % initial oxygen and with molten Fe_2O_3, both at a chamber pressure of 1.0 MPa. Two experiments were performed with the Corium-E simulant (10-115-1 and 10-115-2) and one experiment with the molten iron oxide (10-114-1). Explosions were not observed with either melt at this pressure.

2.3.2 Determination of Gaseous Oxygen Evolved During Melting

Test of Technique -- During this quarter, a Teledyne Model 320A electrochemical gaseous oxygen analyzer, equipped with flowthrough adaptor, was inserted in the outlet argon flow from the arc melting innerchamber. This analyzer gives a linear voltage output which is proportional to the oxygen content of the gas stream over wide concentration ranges. The output of the analyzer was recorded as a function of time with a Honeywell Model 193 recording potentiometer. A schematic diagram of the arrangement is shown in Figure 2-19. The output of the analyzer was integrated as a function of time, and calibrated with known volumes of oxygen sent through the analyzer via a bypass system. The purpose of these analyses is to determine the instantaneous composition of the melt at the time of flooding to determine the effect, if any, of the chemical nature of the melt on the explosive triggering interaction. The applicability of the technique to these experiments was explored by determining instantaneous melt composition in three separate ways in the same arc-melting experiment (10-113-2), which included flooding with water but without application of an initiating pressure transient. Melt composition was determined by weight loss of the sample, by

56

measuring the gaseous oxygen evolved during melting with the electrochemical analyzer, and by wet chemistry applied to the residue remaining after the experiment. The results of this test of technique are shown in Table 2-III. Notice that the compositions of the melt at flooding time as determined by the three independent techniques are within ±0.5 at. %.
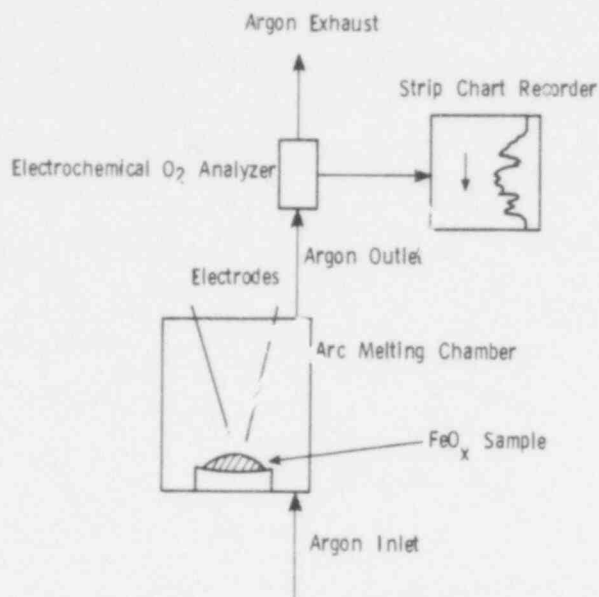
Figure 2-19. Schematic Diagram of Apparatus Used to Determine True Composition of FeO_x Melts at Flooding Time

TABLE 2-III

Determinations of Composition of an Iron Oxide Melt by Three Independent Techniques

	Method		
Composition	Weight Loss	Volume of O_2	Wet Chemistry
O/Fe[*]	1.176	1.190	1.151
X_O[**]	0.540	0.545	0.535

[*]Oxygen-iron ratio

[**]Mole fraction of oxygen

Melt Compositions Before and After Explosive Interaction -- Once confidence in the gaseous oxygen analyses was obtained, the technique was then applied to determining the compositions at flooding time of melts which were induced to explode with a bridgewire pulse. Two experiments were performed with molten Corium-E simulant of 61.5 at.% initial oxygen content (10-111-1 and 10-113-1) and two w.h melts formed from Fe_2O_3 (10-109-1 and 10-110-1). In addition, both samples of debris retrieved from the molten iron oxide experiments were analyzed for oxygen content by wet chemistry for comparison with the composition determined just prior to the interaction by the electrochemical evolved oxygen analyzer. The debris retrieved from the Corium-E simulant explosions was not analyzed, since normal analytical techniques are time-consuming and inaccurate. (Ease and accuracy of analysis is one reason for using the simple binary iron-oxygen melts as a simulant of the Corium-E compositions; see Appendix A of SAND78-0076.)[8] The results of these experiments are shown in Table 2-IV.*

TABLE 2-IV

Determination of Melt and Debris Compositions in
Explosive Flooding Interactions With Oxidic Melts*

Experiment No.	Starting Material	Melt Composition by Gas Analyzer (O/Me)	Debris Composition by Wet Chemistry (O/Me)
10-109-1	Fe_2O_3	1.235	1.236
10-110-1	Fe_2O_3	1.251	1.241
10-111-1	Corium-E Simulant**	1.360	N.D.
10-113-1	Corium-E Simulant**	1.380	N.D.

---

* Flooding was done with borated water (3000 ppm B as B_2O_3).
** Initial oxygen content was 61.5 at.%.

---

*One difference between the experiments reported in Table 2-IV and the experiment as normally performed should be recorded: In all four experiments, borated water was used for the flooding. These experiments are thus not strictly comparable to those performed with deionized water as the coolant; the effect of the water composition is probably negligible, however. Normal experiments with deionized water are planned.

467 248

Notice that, for the two experiments reported in Table 2-IV, the difference between the compositions of the iron-oxygen melts when flooded (determined with the gaseous analyzer) and the retrieved debris (determined by wet chemistry) is very small. This small difference would tend to place a limit on the amount of gaseous oxygen which could be liberated during the interaction, as suggested by the impulse-initiated gas release hypothesis proposed by Buxton and Nelson.[5]

2.4 References

1. Light Water Reactor Safety Research Program Quarterly Report, October - December 1977, SAND78-0600, Nuclear Fuel Cycle Safety Research Department, Sandia Laboratories, Albuquerque, NM, June 1978.

2. Light Water Reactor Safety Research Program Quarterly Report, January - March 1978, SAND78-1511, Nuclear Fuel Cycle Safety Research Department, Sandia Laboratories, Albuquerque, NM, October 1978.

3. Light Water Reactor Safety Research Program Quarterly Report, April - June 1978, SAND78-1901, Nuclear Fuel Cycle Safety Research Department, Sandia Laboratories, Albuquerque, NM, January 1979.

4. Commercially available as RP1 detonators from Reynolds Industries, Marina del Rey, CA.

5. L. S. Nelson and L. D. Buxton, Steam Explosion Triggering Phenomena: Stainless Steel and Corium-E Simulants Studies with a Floodable Arc Melting Apparatus, SAND77-0998, Sandia Laboratories, Albuquerque, NM, May 1978.

6. R. W. Fairbridge, Encyclopedia of Oceans, Reinhold, New York, NY, 1966, p. 792.

7. P. Cohen, Water Coolant Technology of Power Reactors, Gordon and Breach, New York, NY, 1969, p. 215.

8. Light Water Reactor Safety Research Program Quarterly Report, July - September 1977, SAND78-0076, Nuclear Fuel Cycle Safety Research Department, Sandia Laboratories, Albuquerque, NM, April 1978.

3. Statistical Analysis

3.1 Summary

This program has as its goal the application of statistical methods for predicting the probable distribution of peak clad temperature (PCT), as calculated by RELAP4, during a loss-of-coolant accident (LOCA). The response surface method is being used for this purpose to minimize the number of calculations required.

We continued to investigate the question of problem initialization for the off-nominal power levels to be used in the study. Calculations were made (at 94 and 106% power) with thermal and mechanical balancing appropriate to the power level. The effect of balancing on PCT for these runs was shown to be small.

It was determined that the fuel state (i.e., fresh or once-burned) has no important effect on temperature histories or hydrodynamics during the blowdown portion of a LOCA. Fresh fuel was assumed in 26 blowdown calculations, and the results were used to establish a PCT prediction surface for the Zion plant. These calculations showed a PCT range of about $500°$ F $(920°$ to $1420°$ F), and provided information on the relative importance of various physical models and input parameters.

3.2 Steady-State Calculations and Problem Initialization (R. K. Byers and M. Berman)

It may be recalled from previous quarterlies that considerable difficulty was encountered in attempts to calculate steady-state operation of the Zion plant. Our intent was to determine if, using off-nominal power levels, the reactor would adjust, over a reasonable period of time to the nonstandard conditions. This would eliminate any need for a large number of input modifications, i.e., balancing for each power level in the statistical set. When the original input data set was modified by the addition of a large "buffer" volume to the pressurizer, adequate steady-state calculations could be made when a suitable timestep for the calculation was found and an improved flow predictor was used. Reactivity feedback was found to have no significant effect in the calculations. However, when breaks were initiated after various delay times, subsequent results did not converge in calculationally feasible times.

During the course of the above work, we considered the possibility that variations in PCT among the off-nominal power cases might be small enough to be acceptable. To examine this question, it was decided to perform calculations at the limits of the power range for thermally and mechanically balanced problems. During this quarter, a procedure for altering some input parameters depending on power level was implemented.

The initialization approach was based on the following assumptions for off-nominal power conditions:

- For the steam generators: heat transfer rate, temperature drop across the primary side, and secondary-side flow rate, all vary as the ratio of power to nominal power.

- The sum of secondary-side temperatures and mean inlet-outlet primary-side temperatures is equal to its value at nominal power conditions.

- Primary coolant loop mass flow rates are equal to their nominal values.

When these assumptions are combined with one of constant temperature through the steam generator secondaries, the results for volume average temperatures are (superposed tilde indicating off-nominal power condition):

$$\tilde{\tilde{T}} = \frac{1 + \pi}{2}\,\bar{\tilde{T}}_p + \frac{1 - \pi}{2}\,T_s$$

$$\tilde{T}_s = \frac{1 - \pi}{2}\,\bar{\tilde{T}}_p + \frac{1 + \pi}{2}\,T_s \qquad$$

Beginning at hot side of (say) the intact loop: (Volume k is nearer the vessel than Volume k+1)

$$\tilde{T}_p^{\,I} = \bar{\tilde{T}}_p + \frac{\pi}{2}\left(T_p^{\,I} - T_p^{\,O}\right) \qquad \tilde{T}_{k+1} = \tilde{T}_k + \pi\left(T_{k+1} - T_k\right).$$

$$\tilde{T}_p^{\,O} = \bar{\tilde{T}}_p - \frac{\pi}{2}\left(T_p^{\,I} - T_p^{\,O}\right)$$

Here, $\bar{\tilde{T}}_p$ indicates mean of steam generator primary-side inlet and outlet temperatures $\left(= 1/2\left(T_p^{\,I} + T_p^{\,O}\right)\right)$ and Ts indicates secondary-side temperature for the steam generator; π is the ratio of power level to nominal power level, e.g., 1.06 for 106% power. The resulting temperature changes sometimes necessitate minor input changes, such as junction loss factors, before proceeding with the calculation.

Table 3-I summarizes the combination of problems we have calculated for the Zion plant (Figure 3-1) in testing the balancing technique. As was our hope, the differences in PCT are small, giving us reason to believe that, indeed, the statistical study can be carried out without any re-balancing at off-nominal powers.

TABLE 3-I

Thermal Balance Runs

Run Name	Power (%)	Steady-State Period	Thermal Balance?	ΔT Core	SLAB 15		SLAB 16	
					Time	Max Temp (°F)	Time	Max Temp (°F)
BD4A	100	0.01	Yes	59.30	6.65	1087	6.50	1094
	100	80.01	Yes	59.30	6.70	1076	6.51	1071
BDST-05E	106	0.01	Yes	62.87	6.63	1134	6.52	1128
06B	106	0.01	No	59.30	6.63	1132	6.50	1125
05F	106	80.01	Yes	62.87	6.64	1126	6.51	1116
06C	106	80.01	No	59.30	7.56	1116	7.53	1104
07D	94	0.01	Yes	55.73	6.61	1040	6.50	1037
08A	94	0.01	No	59.30	6.64	1045	6.49	1041
07E	94	80.01	Yes	55.73	6.50	1033	6.50	1032
08B	94	80.01	No	59.30	5.79	1041	5.47	1040

Good agreement in other quantities was also obtained in the runs with and without rebalancing. Fuel stored energies are virtually identical for both the high and low power cases (Figures 3-2 and 3-3). As shown in Figures 3-4 and 3-5, the only difference in slab temperatures occurs later than the peaks (again for both power levels), and does not appear to be of significant magnitude. Core flows, pressures, and temperatures (Figures 3-6 through 3-8) are also practically identical.

Another consequence of rebalancing may be noted in Figures 3-9 and 3-10. (Time axes are measured from break initiations.) Previously, it was not possible to achieve good agreement for off-nominal calculations with and without delays before the break. It appears from the near identity of these results that the failure to do so was caused by the initial imbalance and, consequently, a large drift away from initial conditions.

To make a decision on whether to use a fresh or once-burned description of the fuel in the study, we compared results of calculations whose input differed only in that respect. All other specifications were nominal and the Zion nodalization (Figure 3-1) was again used.
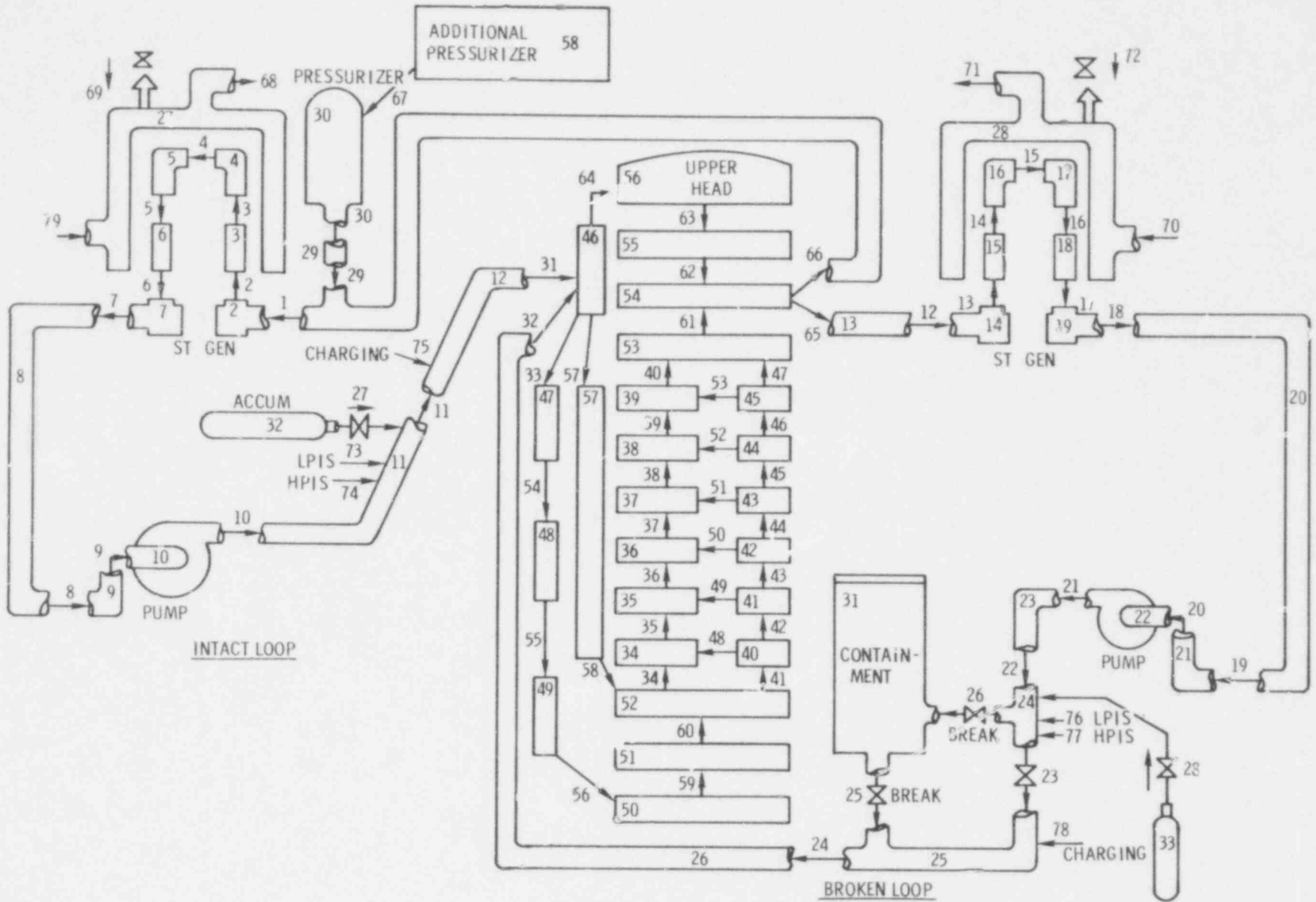
Figure 3-1. RELAP4 Nodalization for BE/EM Study
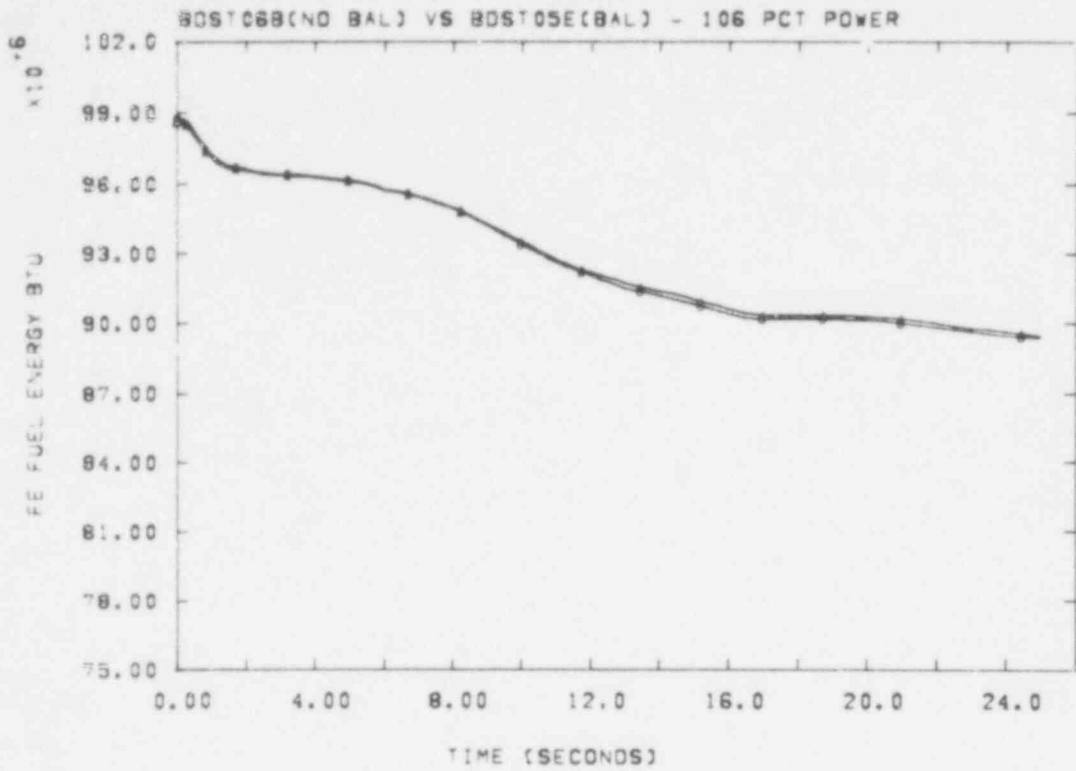
Figure 3-2. Fuel Stored Energy for High Power Case, No Rebalancing vs Rebalancing
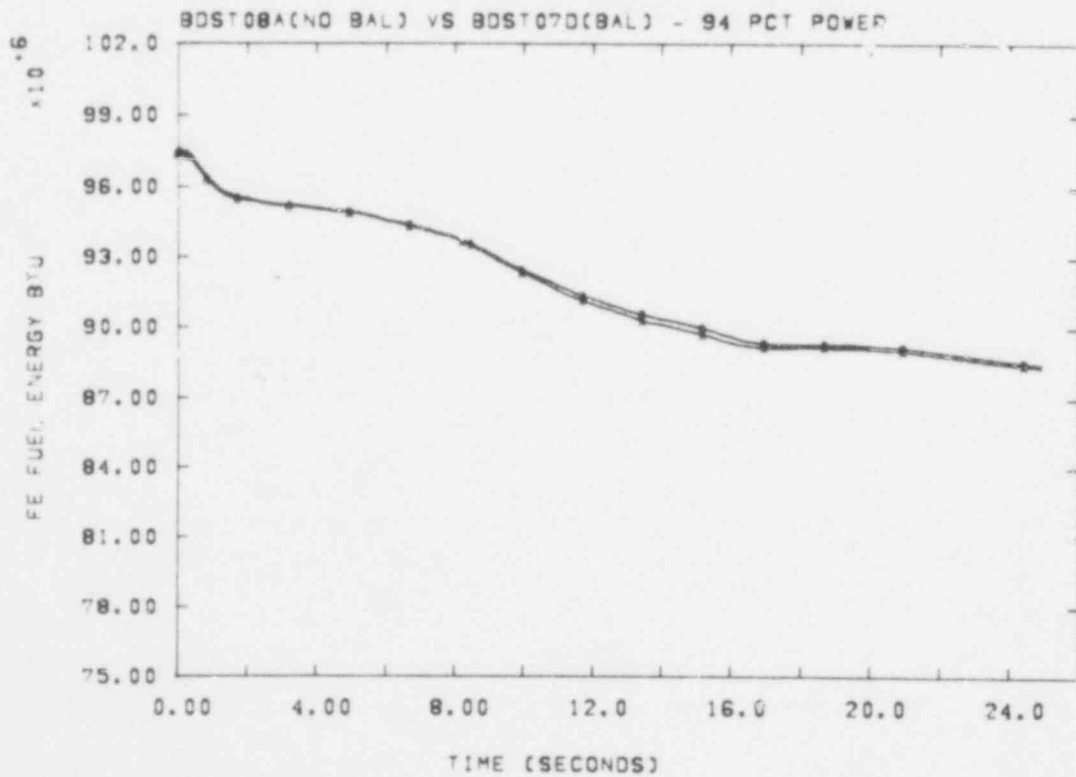
Figure 3-3. Fuel Stored Energy for Low Power Case, No Rebalancing vs Rebalancing
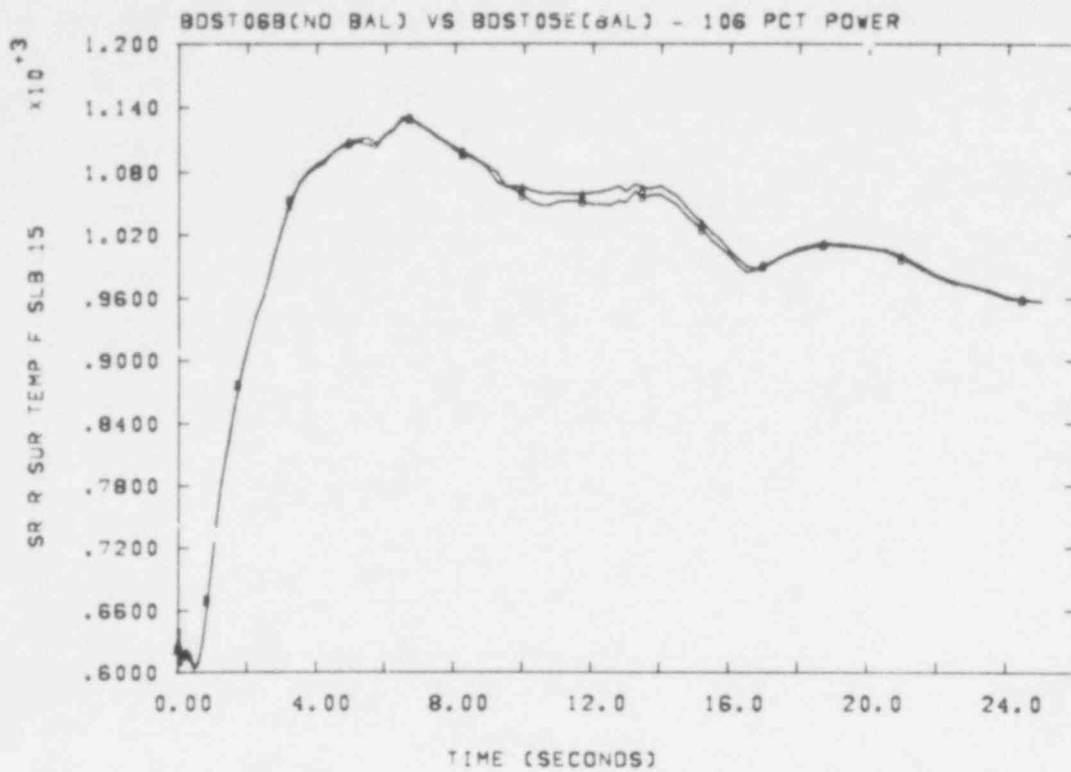
Figure 3-4. Clad Temperatures, High Power Case, No Rebalancing vs Rebalancing
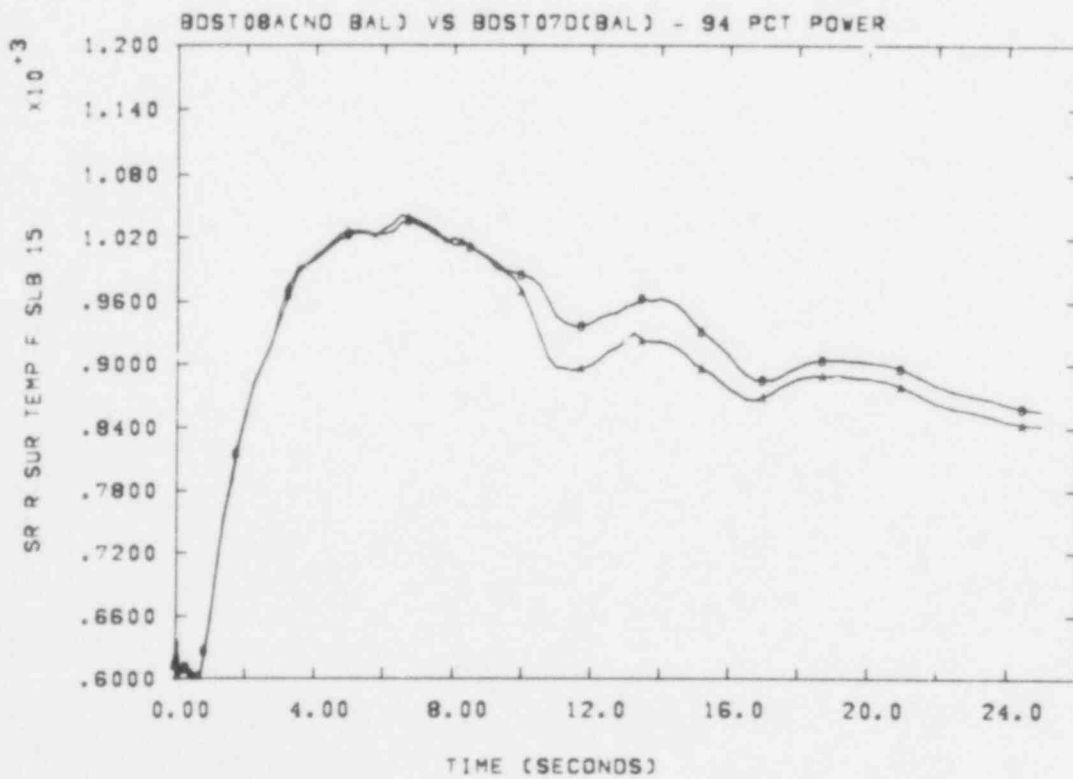
Figure 3-5. Clad Temperatures, Low Power Case, No Rebalancing vs Rebalancing

467 255

BOSTO8A(NO BAL) VS BOST07D(BAL) - 94 PCT POWER
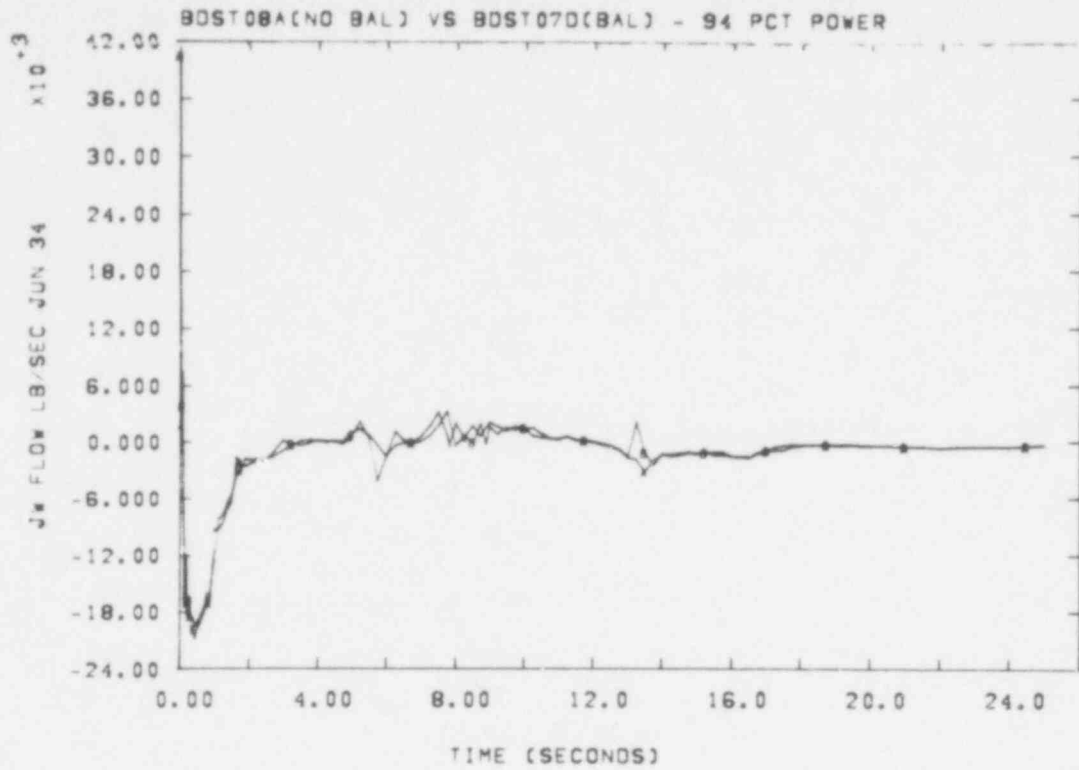
Figure 3-6. Mass Flow into Bottom of Average Core, Balanced and Not Balanced

BOSTO8A(NO BAL) VS BOST07D(BAL) - 94 PCT POWER
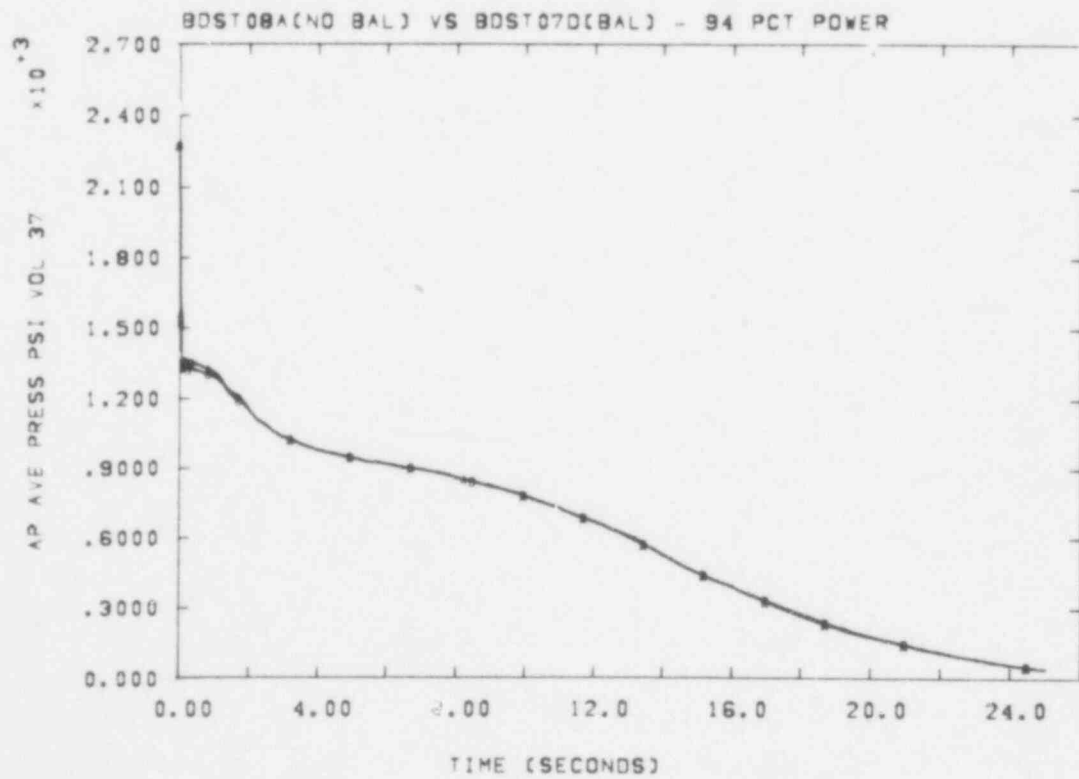
Figure 3-7. Fluid Pressure at Middle of Average Core, Balanced and Not Balanced

467 256

BOSTOBA(NO BAL) VS BOST070(BAL) - 94 PCT POWER
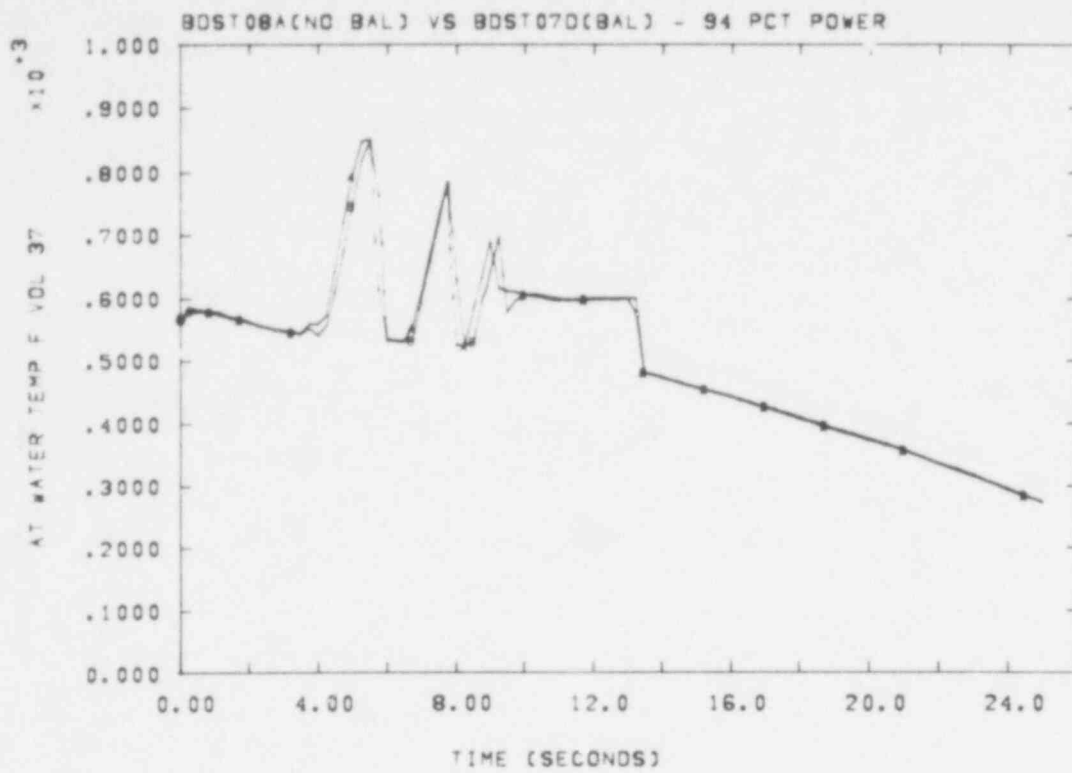
Figure 3-8. Fluid Temperature at Middle of Average Core, Balanced and Not Balanced

BOST070(.01 SS) VS BOST07E(80.01 SS),94 PCT,REBAL
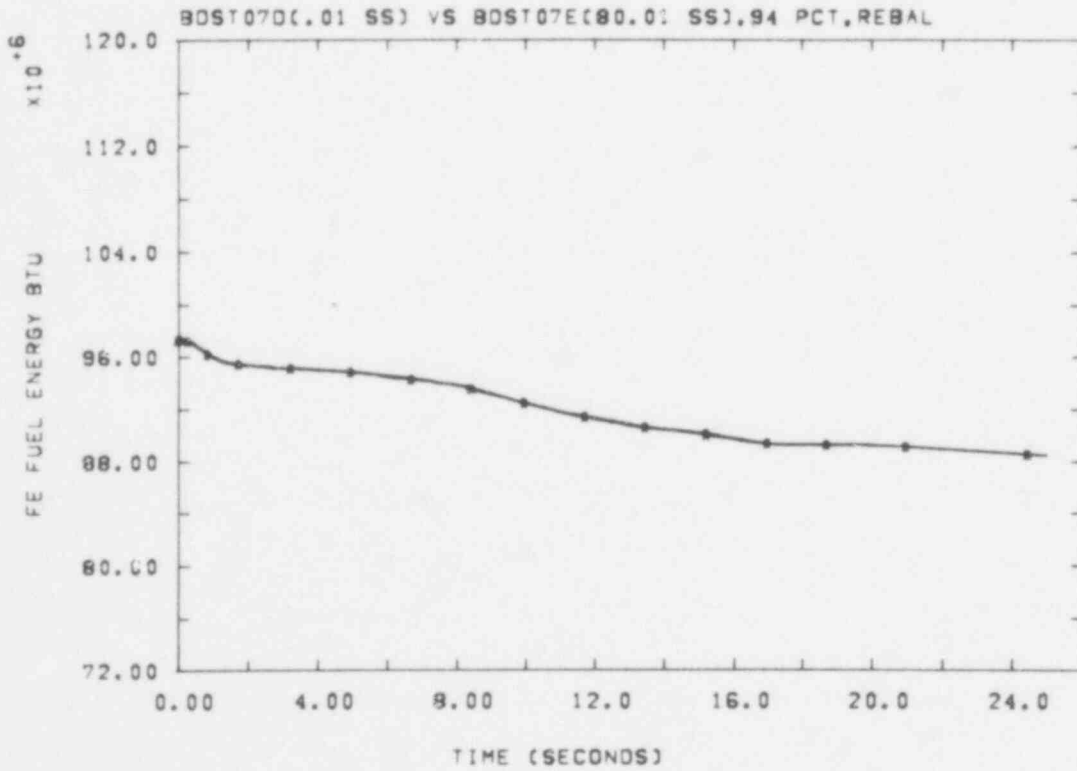
Figure 3-9. Fuel Stored Energy for Break Times of 0.01 and 80.01 s
(Balanced for Off-Nominal Power)

467 257

BOST07O(.01 SS) VS BOST07E(80.01 SS),94 PCT,REBAL
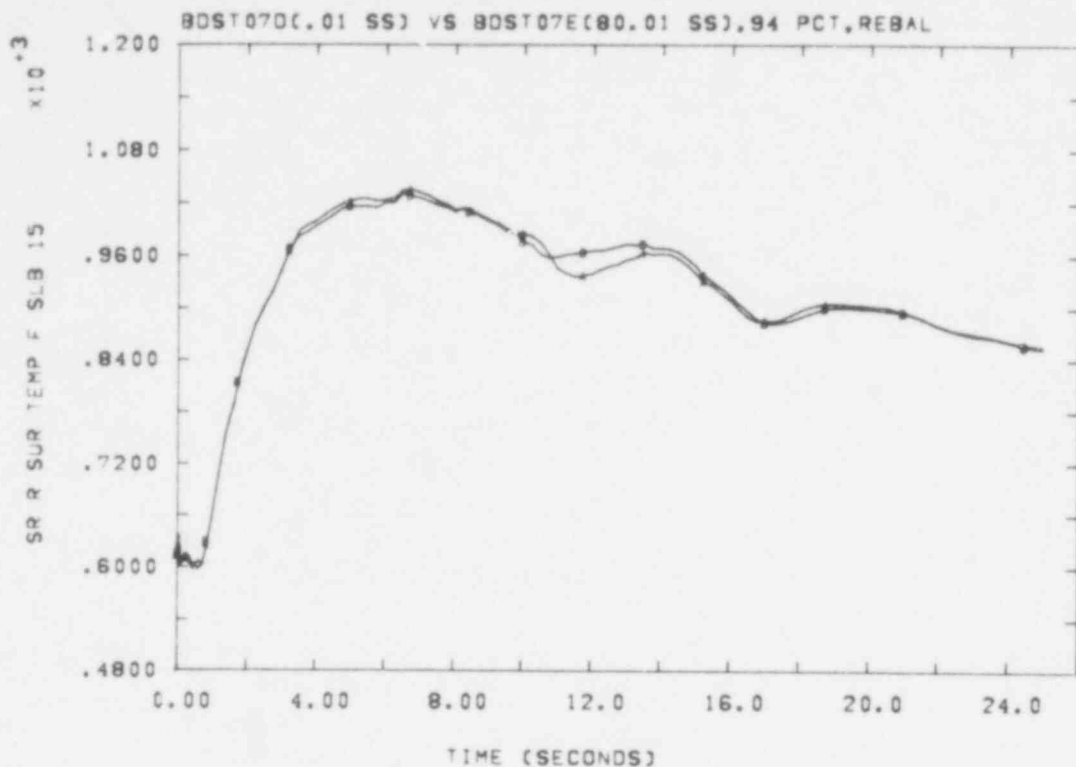
Figure 3-10. Clad Temperatures for Break Times of 0.01 and 80.01 s
(Balanced for Off-Nominal Power)

The RELAP input parameters affected by fuel state (i.e., fresh or once-bur...are gap
width and decay heat (as discussed in the last quarterly report). As Figure 3-11 shows, modeling
the fuel as once-burned resulted in complete closure of almost all of the pellet-to-clad gaps in the
hot initial state. However, there appeared to be no significant effect of this phenomenon on subse-
quent behavior during the transient. Slight differences over short periods of time were seen in
such quantities as flow and temperature histories. For example, Figures 3-12 and 3-13 show that
flow to the upper annulus and middle hot pin temperature were virtually unchanged by the choice of
fuel states. More global quantities, such as fuel stored energy (Figure 3-14), were affected to a
much smaller degree. Therefore, the fuel state was assumed to be fresh for all the runs in the study.

3.3   Results of Statistical Blowdown Runs (G. P. Steck)

The first 26 RELAP runs were made (the scheduled 25 plus 1 with all variables at nominal) and
the results are shown in Table 3-II.

Since, in this report, the input variables are coded 1 to 21, the reader may wish to refer to
Table 3-III for their definitions. A complete description of the implementation of these variables may
be found in the progress report for last quarter.[1]

Figure 3-11.   Statistical Study--Nominal Dials BD4A (Fresh
Fuel) vs BD4B (Once-Burned Fuel), Gap Thick-
ness at T = 0 for Hot Pin

Figure 3-12.   Flow to Upper Annulus, Effect of Fuel State

Figure 3-13. Effect of Fuel State on Clad Temperatures

Figure 3-14. Effect of Fuel State on Stored Energy

467 260

71

TABLE 3-II

Values of Independent and Dependent Variables for First 26 Runs

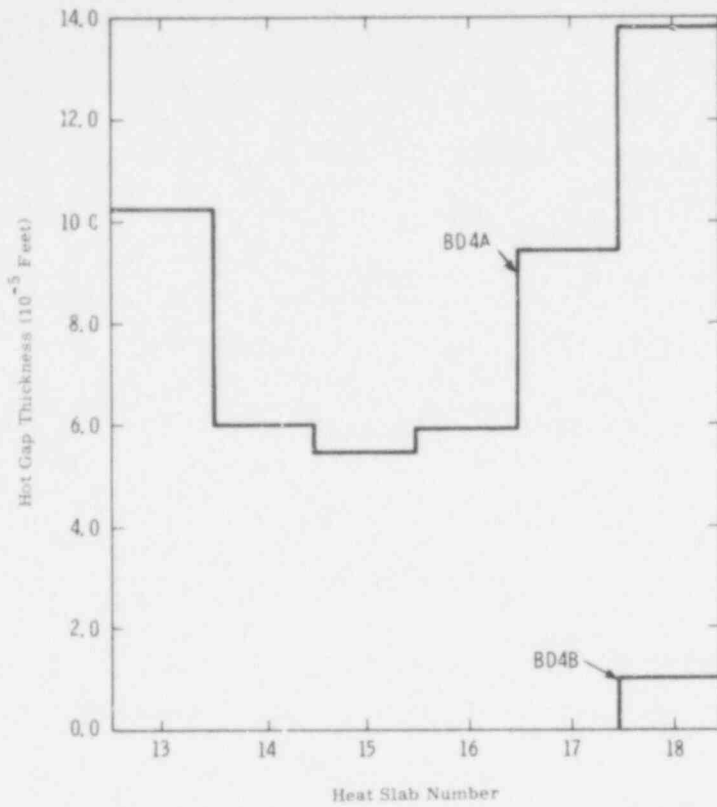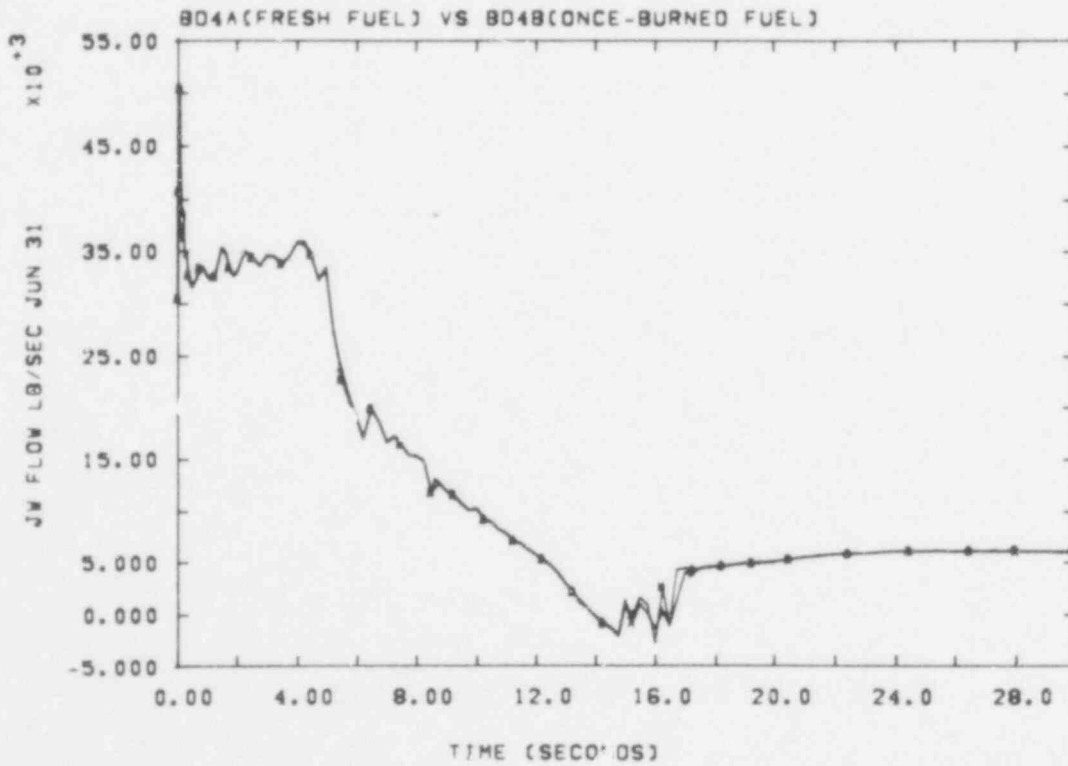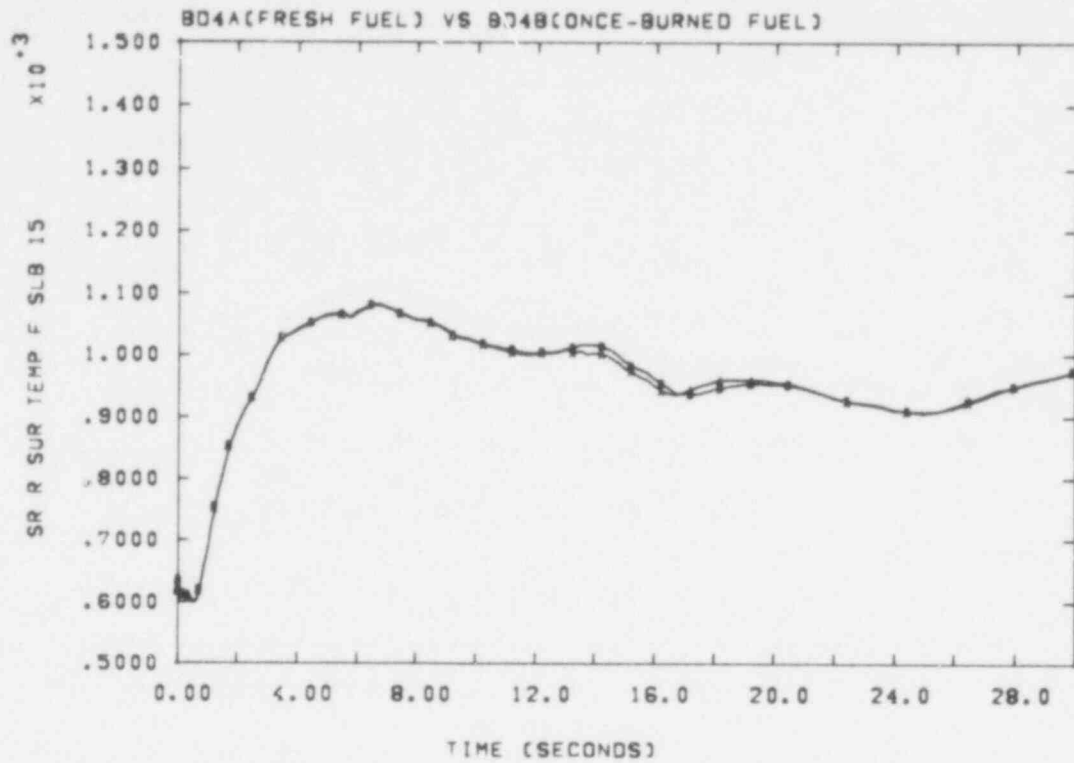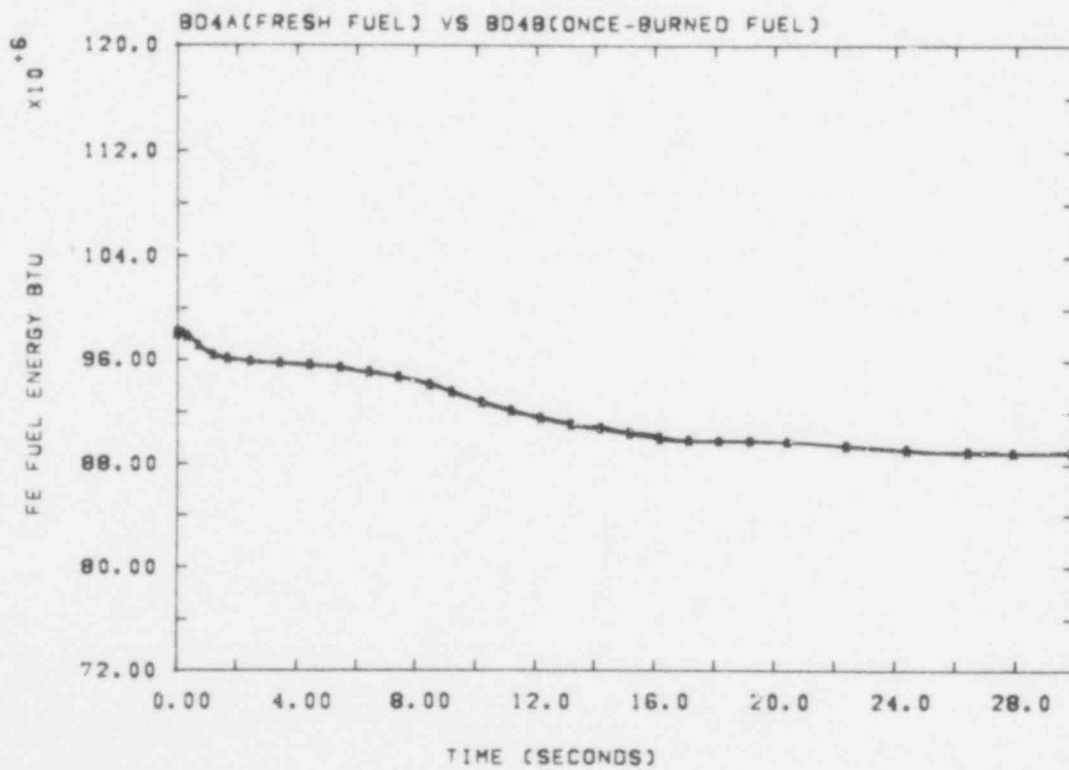|	1	2	3	4	5	6	7	8	9	10	11	12	13	14	15	16	17	18	19	20	21	T15	T16	TMAX
0	.90	0.00	0.00	1.00	1.00	1.00	1.00	1.00	1.00	1.00	1.00	1.00	0.00	9.00	90.0	643.2	226.0	1.57	1.00	.23	0.00	1183.	1175.	1183.
1	.82	-.11	.53	.62	1.00	1.62	.62	1.82	.91	.97	1.00	.97	1.10	-.70	84.4	634.6	178.3	1.60	.78	.19	.48	1082.	1188.	1188.
2	1.16	.46	.26	1.31	1.28	1.07	.98	.91	.88	1.22	1.00	1.03	6.73	.41	113.6	657.5	108.8	1.65	.88	.11	-.03	1178.	1203.	1203.
3	1.06	.19	.19	.83	.46	1.00	1.08	1.34	.99	1.07	1.00	1.02	3.47	-.29	78.6	655.9	182.2	1.76	1.00	.16	-.03	1189.	1178.	1189.
4	.83	.13	.15	1.27	.34	.60	1.01	1.04	1.33	.65	1.00	1.03	4.75	-.19	59.3	601.2	289.2	1.62	1.23	.23	.46	1271.	1273.	1273.
5	.84	.68	.02	.59	.94	1.51	.88	1.31	.72	1.02	1.00	1.04	2.88	-.38	123.5	651.8	396.3	1.64	.83	.25	.14	1162.	1184.	1184.
6	.90	-.04	.41	.48	1.46	.90	.75	.62	1.22	.57	1.00	1.01	-.34	-.66	120.4	688.1	37.5	1.48	1.13	.24	-.04	1068.	1098.	1098.
7	.89	-.12	-.28	1.01	.42	1.03	.82	.81	1.43	.75	1.00	1.00	-2.35	-.42	62.8	621.9	356.3	1.36	1.02	.18	-.05	988.	1013.	1013.
8	1.00	.02	-.11	1.05	2.45	.66	.91	1.38	1.15	1.29	1.00	.95	2.38	.32	90.0	602.2	71.7	1.49	.81	.27	.04	1328.	1321.	1333.
9	.96	-.05	.79	1.03	.50	.91	1.18	.89	1.04	1.17	1.00	1.03	-1.86	-.89	54.2	647.8	190.2	1.76	.76	.30	-.01	1443.	1442.	1443.
10	.87	.67	.78	1.10	1.57	1.45	1.23	.68	1.12	1.21	1.00	.96	-3.65	.47	75.6	638.5	238.2	1.59	1.17	.27	-.02	1033.	1163.	1163.
11	1.08	.62	-.69	1.15	2.14	.68	1.26	.74	.86	1.12	1.00	.97	-1.33	.28	90.5	616.2	309.6	1.76	.72	.35	.55	1595.	1593.	1595.
12	.74	-.02	-.58	.71	1.69	1.34	1.27	.83	.83	.68	1.00	1.00	2.88	-.88	49.7	573.8	67.6	1.44	.84	.25	-.02	1992.	1847.	1892.
13	.94	.25	-.23	1.52	1.87	.97	1	1.16	.80	1.09	1.01	-1.94	-.02	93.5	668.9	317.9	1.46	.94	.25	.03	1262.	1281.	1281.
14	1.04	-.06	.06	.78	.61	.75	.78	.52	1.07	.73	1.00	.96	-3.88	.22	119.5	672.0	359.8	1.66	1.11	.21	-.01	1129.	1154.	1154.
15	1.00	.56	.65	1.36	.82	1.38	.71	.64	.78	1.25	1.00	1.04	4.32	.15	87.9	611.7	432.5	1.68	.67	.35	-.02	1445.	1457.	1457.
16	.75	.34	.36	.91	1.12	.78	1.14	1.02	.84	.68	1.00	.99	-3.94	.37	107.6	663.8	12.3	1.61	1.19	.31	-.04	1293.	1320.	1320.
17	.80	-.21	-.37	.74	.67	.53	1.03	1.23	1.04	.85	1.00	.96	-2.64	.54	64.7	641.1	270.6	1.39	1.06	.37	-.04	1351.	1337.	1391.
18	.80	-.15	-.79	1.20	1.98	.74	.79	1.46	.89	.89	1.00	1.05	8.82	-.26	67.9	635.7	216.7	1.43	.90	.25	.62	1200.	1215.	1215.
19	1.18	-.18	-.87	1.23	.64	.88	.86	.71	.96	1.39	1.00	.98	-2.88	-.13	112.1	619.9	142.3	1.52	1.18	.24	.68	1200.	1226.	1226.
20	1.03	-.19	-.42	.51	1.44	1.19	1.06	1.67	1.27	.79	1.00	1.00	.36	-.53	130.6	642.1	174.6	1.68	1.19	.15	.39	1020.	1045.	1045.
21	.92	-.07	-.68	1.40	.57	1.22	1.12	1.55	1.89	1.45	1.00	.99	5.94	.82	95.9	648.6	382.0	1.61	1.04	.16	.20	1137.	1168.	1148.
22	.78	.51	-.19	.92	1.24	.78	.93	.79	.99	.92	1.00	.96	5.71	.06	101.6	663.8	255.5	1.49	.92	.30	-.01	1327.	1312.	1347.
23	.77	.88	.33	.55	1.84	1.12	1.19	.96	.96	.43	1.00	.97	-.65	.76	79.3	623.1	410.9	1.81	1.89	.19	.69	1862.	1885.	1883.
24	.95	-.14	-.49	.68	.72	1.41	.71	1.19	1.38	1.34	1.00	1.02	-1.64	.61	105.8	626.7	133.0	1.70	.90	.31	.22	1330.	1380.	1390.
25	.87	.40	.55	1.14	.88	1.72	1.34	1.88	1.28	.53	1.00	1.01	.15	-.52	72.9	678.3	29.2	1.48	.68	.24	.21	1193.	1238.	1211.

TABLE 3-III

Input Variables and Values

Parameter	Range	Nominal Value
1. DLEHRY = subcooled discharge coefficient	0.7 → 1.2	0.9
2. DLHEM = saturated discharge coefficient	-0.25 → 1.0	0.0
3. SLIP = slip correlation dial	-1.0 → 1.0	0.0
4. DLTF = 2-phase form loss dial	0.4 → 1.6	1.0
DLTFFM = 2-phase fanning friction loss dial		
These dials are assumed to be equal, and a single variable.		
5. DCHF = critical heat flux dial	0.3 → 3.0	1.0
6. DHTC6 = Condie-Bengston dial	0.5 → 2.0	1.0
7. DHTC7 = free convection and radiation dial	0.6 → 1.5	1.0
8. DHTC8 = Dittus-Boelter dial	0.5 → 2.0	1.0
9. DHTC9 = Hsu and Bromley-Pomeranz dial	0.5 → 2.0	1.0
10. DLBLK = flow blockage dial multiplier	0.4 → 1.6	1.0
11. DLMWR = multiplier of Cathcart-Pawel reaction rates	0.85 → 1.15	1.0
12. DLPWR = power level multiplier	0.94 → 1.06	1.0
13. DLCPR = increment to be added to containment pressure	-5.0 → 10 psia	0.0
14. DLPUMP = dial for 2-phase pump head multiplier	-1.0 → 1.0	0.0
15. ECCTMP = temperature of accumulator and safety injection system water	40° → 140° F	90°F
16. DLACC = accumulator pressure	593.2 → 693.2 psia	643.2 psia
17. TLF = time in life	0.0 → 440 months	226 months
18. PFUNC = peaking factor uncertainty multiplier	0.84 → 1.16	1.0
19. DLECON = thermal conductivity dial multiplier	0.6 → 1.3	1.0
20. DLGAP = additive uncertainty in radial gap size	±1.5 mils	0.0
NOB = 0 → fresh fuel = 1 → once burned fuel		
21. DLDEC = decay heat multiplier	-0.06 → 1.0	0.0

After the first 14 runs were made, response surfaces were determined for the maximum temperatures of slabs 15 and 16, labeled T15 and T16 in what follows. These models are shown in Table 3-IV. The terms used in Table 3-IV may be unfamiliar. For completeness we give their definitions in the next paragraph.

Let n denote the number of dial sets used to produce a model and let

$$S_T^2 = \frac{1}{n} \sum_{i=1}^{n} (PCT_i - \overline{PCT})^2 ,$$

where

$$\overline{PCT} = \frac{1}{n} \sum_{i=1}^{n} PCT_i .$$

If $\overset{\wedge}{PCT}_i$ denotes the model prediction for PCT_i, then

$$RS = \sum_{i=1}^{n} (PCT_i - \overset{\wedge}{PCT}_i)^2$$

is the residual sum of squares and $MSR = RS/(n - k - 1)$ is the residual mean square (k is the number of terms in the model) and $RMSR = \sqrt{MSR}$, the root mean square residual. In this notation R^2, which is the percent of total variability in the dependent variable accounted for by the model, is defined to be $R^2 = 1 - RS/nS_T^2$. The "Relative Importance" of a variable is 100 times the change produced in the dependent variable PCT (in units of S_T) produced by a $1\,\sigma$ change in that variable.

Although a good model based on 14 observations was obtained with only three terms, it did not predict well. The RMS prediction error for T15 and T16 in the next six runs was $250°F$ and all errors were ones of underprediction which shows the model is based more on idiosyncrasies in the data than on any real trends.

The next model used for prediction was based on the first 20 runs. It is shown in Table 3-V.

This time the RMS prediction error in predicting the next six runs was $130°F$, - about half of what it had been. There were errors of both signs although there were more (and larger) errors of underprediction than otherwise.

Note that, in these models, variable 17 is total time-in-life rather than time-into-the-11-month cycle, as it is in the following model. The expression, 17', is used in place of 17 to make the distinction.

A model based on the first 26 runs is shown in Table 3-VI, and Table 3-VII displays peak temperatures and times, as well as ... ator turn-on times, for the full set of runs.

74

467 263

TABLE 3-IV

Response Surfaces for T15 and T16 Based on the First 14 Runs

T15		T16	
Model Terms	Relative Importance	Model Terms	Relative Importance
5 x 5	-92	3 x 5	-95
1 x 17	-42	1 x 17	-68
3 x 16	32	2 x 5	34
$R^2 = 0.986$		$R^2 = 0.987$	
RMSR = 18° F		RMSR = 17° F	

Notes: R^2 denotes percent of total data variability accounted for by the model.

RMSR denotes the root mean square of the residuals.

The sign of the Relative Importance indicates the direction of the effect.

An entry "3 x 5" denotes "X(3)X(5)", which in this case is the slip by DNB correlation interaction.

TABLE 3-V

Response Surface for T15 and T16 Based on the First 20 Runs

T15		T16	
Model Terms	Relative Importance	Model Terms	Relative Importance
19	-83	19	-73
14 x 14	-52	6	-33
7 x 20	-38	18	32
9 x 12	37	19 x 19	31
5 x 8	-35	14 x 14	-19
14	26	17 x 18	-15
12 x 12	24	5 x 17	10
4 x 7	21		
$R^2 = 0.978$		$R^2 = 0.991$	
RMSR = 27° F		RMSR = 15° F	

TABLE 3-VI
Model Based on the First 26 Runs

T15		T16	
Model Terms	Relative Importance	Model Terms	Relative Importance
19	-84 (-104.2)*	19	-84 (-93.2)
18	60 (74.4)	18	52 (57.7)
6	-37 (45.9)	6	-42 (46.6)
19 x 20	-34 (-42.2)	4	26 (28.9)
2 x 14	-27 (-33.5)	1 x 3	-19 (-21.1)
9 x 12	19 (23.6)	12	16 (17.8)
7 x 21	-18 (-22.3)	17	-16 (-17.8)
2 x 15	16 (19.8)	5	-15 (16.7)
16	-14 (-17.4)	1 x 4	-11 (-12.2)

$$R^2 = 0.990 \qquad\qquad R^2 = 0.990$$

$$RMSR = 15°F \qquad\qquad RMSR = 14°F$$

*Note: The numbers in parentheses represent the change in PCT in °F resulting from a 1σ change in the model term.

TABLE 3-VII

BD4 Series - Statistical Study

a	Dial Set	Slab 15		Slab 16		$t: JW_{27} > 0$
		Time at Max	Max Temp (°F)	Time at Max	Max Temp (°F)	
A	Nominal	6.65	1087	6.50	1084	12.5
B	Nominal - Once-Burned Fuel	6.65	1085	6.48	1081	12.5
C	1	4.25	1073	4.26	1100	13.25
D	2	5.50	1155	5.35	1191	10.75
E	3	7.40	1188	7.50	1180	10.75
F	4	8.09	1134	7.25	1132	13.0
G	5	4.08	1124	3.50	1113	10.5
H	6	4.25	921	4.34	943	12.75
I	7	6.25	975	6.12	1003	14.0
J	8	11.88	1172	11.64	1162	11.25
K	9	7.21	1357	7.21	1338	12.25
L	10	5.56	925	5.53	954	12.0
M	11	8.84	1419	8.88	1388	11.5
N	12	4.55	984	4.56	974	13.0
O	13	11.58	1111	11.72	1133	11.5
P	14	6.57	1046	6.41	1070	11.75
Q	15	5.76	1336	5.75	1336	12.0
R	16	4.21	961	7.43	1027	11.25
S	17	6.01	1026	6.00	1009	14.75
T	18	6.82	1069	6.82	1084	14.75
U	19	7.08	1061	7.04	1085	13.0
V	20	4.51	1016	4.66	1044	13.25
W	21	7.37	1117	7.16	1147	13.25
X	22	10.30	1105	10.39	1089	10.75
Y	23	4.97	1041	8.36	1085	10.75
Z	24		1153	5.78	1133	13.5
ZZ	25	8.23	1173	8.21	1183	10.75 (SLAB 14: 1205, 10.15)

From Table 3-VI, we see that the most important parameters, in order of importance, are fuel thermal conductivity, peaking factor, and high-flow film boiling heat transfer. The quantity affected by these three parameters is energy stored in the core which, therefore, seems to be the primary factor in determining PCT. This is clearly a reasonable result.

Examination of the calculated RELAP results gives an indication of the reliability of the importance ranking of the model. For example, the importance of fuel thermal conductivity is consistent with the initial stored energy shown in Figure 3-15. Since RELAP calculates fuel temperatures by solving conduction equations from the outer clad surface toward the centerline, higher thermal conductivity will result in a more uniform temperature distribution, and consequently lower fuel temperature and internal stored energy. Another example is that, for times earlier than PCT occurrence, the dominant mode of heat transfer in most of the calculations is the Condie-Bengston correlation. This behavior is consistent with the high ranking of the mode 6 heat transfer dial in Table 3-VI.
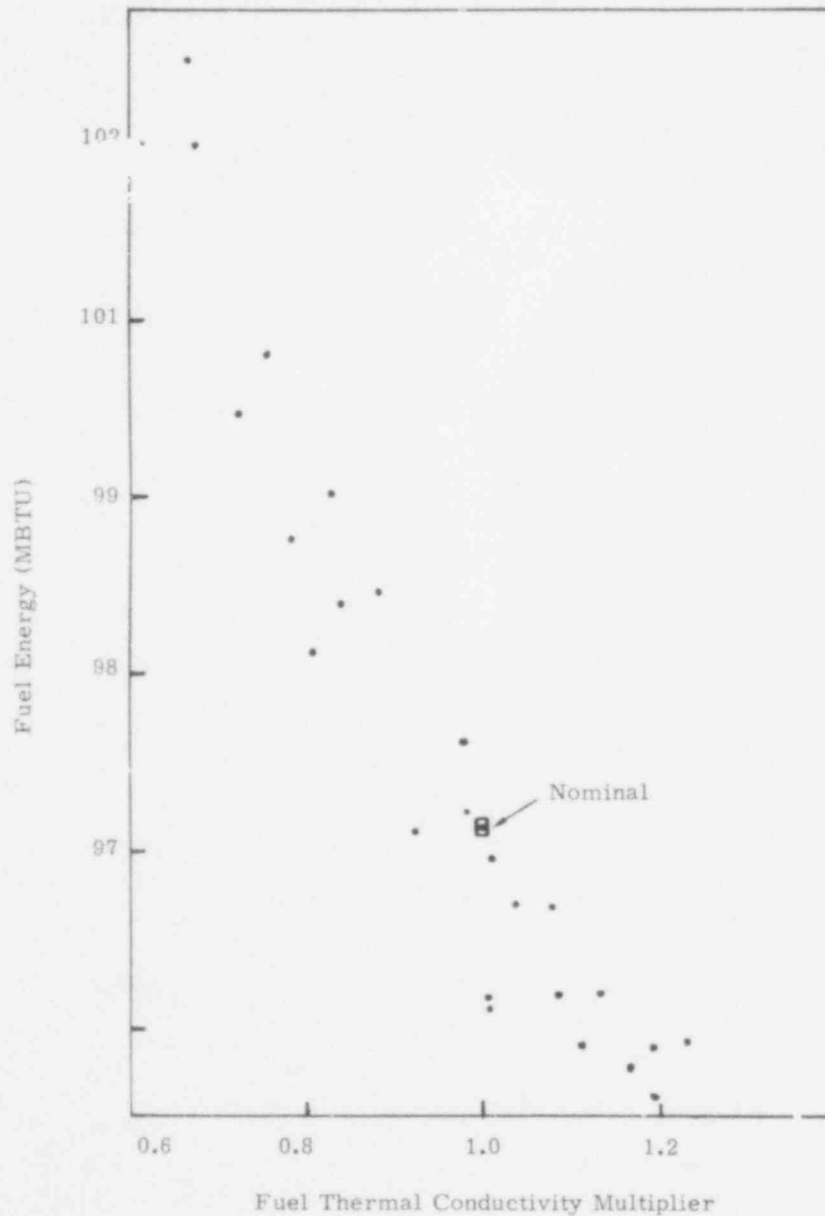

Figure 3-15. Effect of Fuel Thermal Conductivity
on Initial Fuel Stored Energy

467 267

78

It was somewhat surprising that the peaking factor (variable 18) was so much more in-
fluential than the power level (12). However, as may be seen in Table 3-III, the range of the dial
for the former is almost three times that for the latter. Also, the relative unimportance of ECCS
temperature conforms with the data in Table 3-VII (compare PCT times and accumulator turn-on
times). In fact, that it appears at all among the first nine terms is probably an indication that its
calculated importance lies below the limit of reliability of the model.

Input parameters related to hydraulic behavior (e.g., critical flow, slip, etc.) do not seem
to have had much influence on PCT. DNB is also conspicuously absent from Table 3-VI. These
variables might, indeed, not be too important, but we should remain cautious because of the
relatively small number of runs upon which these conclusions are based.

3.4   References

1. Light Water Reactor Safety Research Program Quarterly Report, April - June 1978,
   SAND78-1901, Nuclear Fuel Cycle Safety Research Department, Sandia Laboratories,
   Albuquerque, NM, January 1979.

467 268

4. UHI RELAP Model Development

4.1 Summary (M. Berman, R. K. Byers, R. K. Cole, Jr.)

Upper head injection (UHI) describes a new emergency core cooling system developed by Westinghouse for pressurized water reactors using ice condenser containment systems. Analytic tools (predominantly RELAP4) presently available for studying LOCA are considered inadequate for treating several phenomena whose import has increased with UHI. These include, among others,

- Increased importance of two-phase flow with slip,
- Occurrence of top quench in the core, and
- Upper head draining during refill.

Sandia has embarked on a model development and testing program to improve the treatment of these phenomena in the RELAP4 code. Following are the results for this quarter.

Using RELAP, we continued our effort to obtain a physically reasonable analysis of a LOCA in a plant with UHI. The results of various forms of RELAP calculations exhibit large oscillations (which we regard as unrealistic) whenever our slip model, incorporating the Westinghouse-Zuber (WZ) drift-flux correlation, is employed.[1] In those cases investigated in detail, these oscillations were "triggered" by a transition from the film-annular to the churn-turbulent-bubbly flow regime. This was true even when the transition was continuous, with the profile slip (C_o) and drift-flux (V_{gj}) correlations each made continuous functions of the void fraction.

In an attempt to increase our understanding of the problem, we performed a series of calculations using various combinations of Sandia's modifications to RELAP4/MOD5. These modifications included:

- corrected potential energy treatment and improved flow estimator (for choking) previously described,[2]

- NIFTE recycle changes related to donor-cell definition,[3]

- Westinghouse quench heat transfer,

- junction void-fraction definition derived from continuity-wave considerations (and used consistently in the relative velocity correlation and in the mass fluxes), and

- WZ correlation.

In addition, one calculation was performed using the improved water-properties package developed for RELAP4/MOD7 at INEL.

These calculations, described in following subsections, revealed a number of interactions between the models, some of which are still imperfectly understood. However, there was no evidence that anything other than the WZ correlation itself was involved in the observed oscillatory behavior. Moreover, the cause could not be as simple as the comparatively high relative velocity permitted by this correlation; no oscillation was observed in a calculation using generic MOD5 slip with input parameters chosen to permit a much higher relative velocity.

Finally, a calculation was run with the WZ correlation altered by quadratic spline smoothing at all transition points, making $\partial C_o/\partial\alpha$ and $\partial V_{gj}/\partial\alpha$ continuous as well as C_o and V_{gj}. The intent was to further reduce the strength of any "trigger" associated with a change in flow regime in the hope of avoiding an oscillation. This hope was frustrated; an oscillation was clearly observed when the transition region between film-annular and churn-turbulent-bubbly flow was entered.

This led us to perform an analysis of the stability of the basic differential equations solved by the code (see Section 4.3). We conclude that these equations are unstable (i.e., nave complex characteristics) if the difference between the continuity-wave velocity and the average (mixture) velocity--that is, the velocity of a continuity wave relative to the mixture--is larger than some fraction of the sonic velocity. In the absence of slip, this difference is zero because "continuity waves" reduce to a simple translation, at the material velocity, of density variations. For the WZ correlation and counter-current or small co-current flow, this velocity difference in the transition region is much greater for the churn-turbulent-bubbly regime than for the film-annular regime. This offers a plausible explanation of our observed calculational instabilities, but does not suggest any solution.

During the course of this work, we became aware of relevant work done in Great Britain (RELAP-UK).[4,5] They concluded that stability of the equations depends on the form of the slip correlation employed, and they placed primary emphasis on the role of "profile slip" (corresponding to the distribution parameter $C_o \neq 1$). The correlation employed in RELAP-UK has been constructed to yield stable equations, essentially by making C_o a function of the net mass flux, G, which leads to curved drift-flux lines. We also note that RELAP-UK uses a consistent junction void fraction, defined in a way which agrees with our prescription except for one case. This is the case of gravitationally unstable (low α over high α) counter-current flow, where their prescription leads to a greater relative velocity than does ours.

We are unsure how best to proceed with slip-model development. The WZ correlation perhaps could be modified to give stable equations. The necessary modification is not obvious, and the resulting correlation would probably be quite different from the original. A change involving C_o as a function of mass flux (as in RELAP-UK) would require significant modification of the code. Moreover, it is somewhat disturbing that a correlation derived from experiment should lead to an instability; perhaps the form used for the conservation equations is involved in some manner. While we have not devoted much time to this possibility, it may be possible to cast the equations in a stable form only slightly more complicated than the present drift-flux form.

10

82

467 270

4.2 UHI Calculational Progress

All calculations referred to in the previous section and described below used the most recent UHI nodalization described last quarter[2] (designated UHL); the most important changes in nodalization have been shown to be the azimuthally divided ("double") downcomer and split intact cold leg with pumps downstream of the split. Figure 4-1 shows, for convenience, the UHL nodalization, and Table 4-I summarizes the various important characteristics of the calculations performed.

TABLE 4-I

UHL2 Calculations

UHL2:	Westinghouse quench, NIFTE recycle, WZ slip
UHL2F:	UHL2 with potential energy correction (PE)
UHL2FT:	Westinghouse quench, NIFTE recycle, PE MOD5 slip (Max $V_{slip} \sim 36$ ft/s)
UHL2FT-New:	UHL2FT with MOD7 water properties routines
UHL2FS:	UHL2FT with Max $V_{slip} \sim 1000$ ft/s
UHL2FD:	UHL2FT, but $\Delta\alpha$ term zero
UHL2G:	UHL2F, but WZ slip spline-smoothed
UHL2G1:	UHL2G, but $C_o = 1.0$ for co-current flow

In the following pages we examine the effects of the potential energy correction (Section 4.2.1); the generic slip correlation (4.2.2); and spline smoothing of the WZ correlation (4.2.3).

4.2.1 The UHL2 and UHL2F Calculations

To assess any combined effects of implementing the potential energy correction, along with the rest of our modifications, we compared results of two runs which differ only in that regard (Table 4-I). As in previous similar comparisons,[2] the energy correction seems to affect only the amount of liquid present in the steam generator primaries at late times (see Figures 4-2 through 4-5). In this case, however, the effect is a much smaller one. Figure 4-5 shows a mass difference of perhaps 20%, where previously we have seen factor-of-two differences. We now suspect that the phenomenon is not simply one of gravitational force alone, but involves complex interactions with our NIFTE recycle modifications. Other evidence of such interactions has been reported previously.[2] These could cause, for example, different condensation behavior and ratios of liquid-to-gas masses, but we have not yet determined that this is indeed occurring.
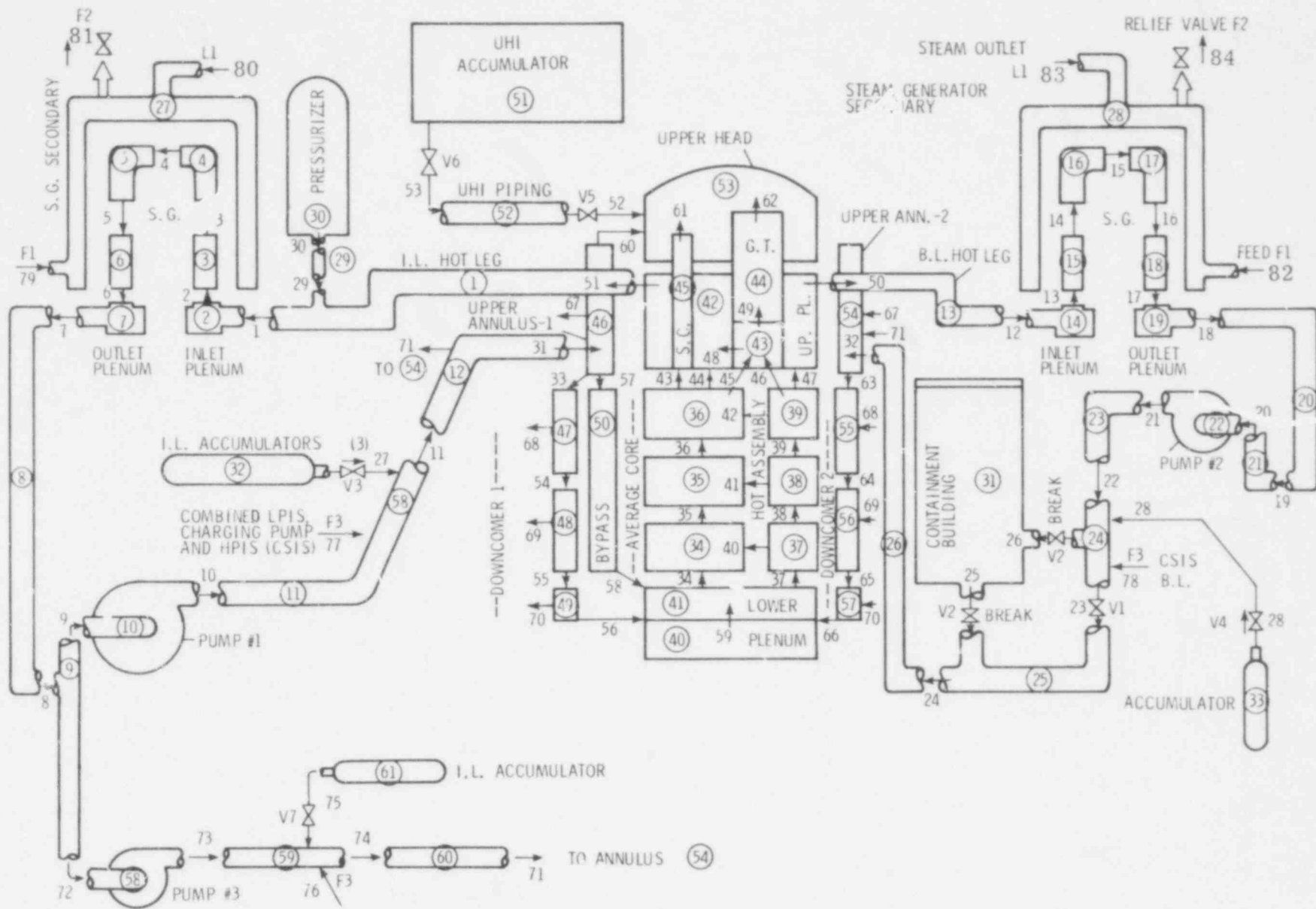
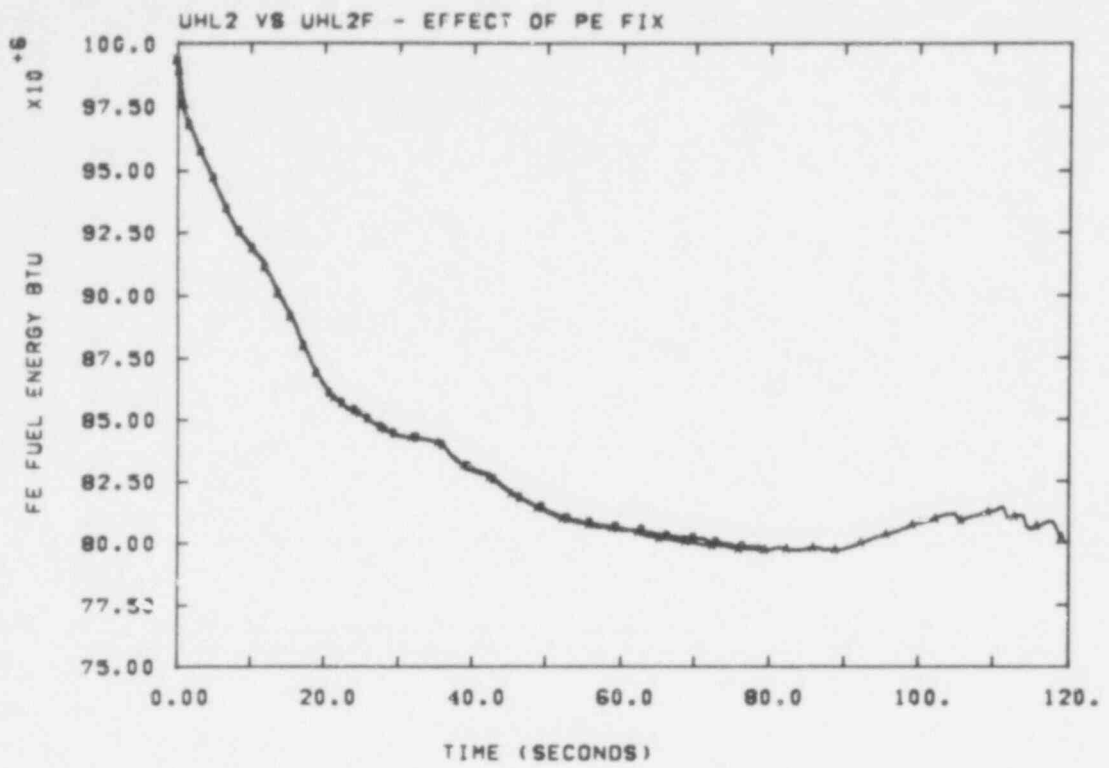Figure 4-1. UHL, an Upper Head Injection Nodalization Scheme With Azimuthally Noded Downcomer

UHL2 VS UHL2F - EFFECT OF PE FIX

Figure 4-2. Fuel Stored Energy, With and Without "PE Fix"
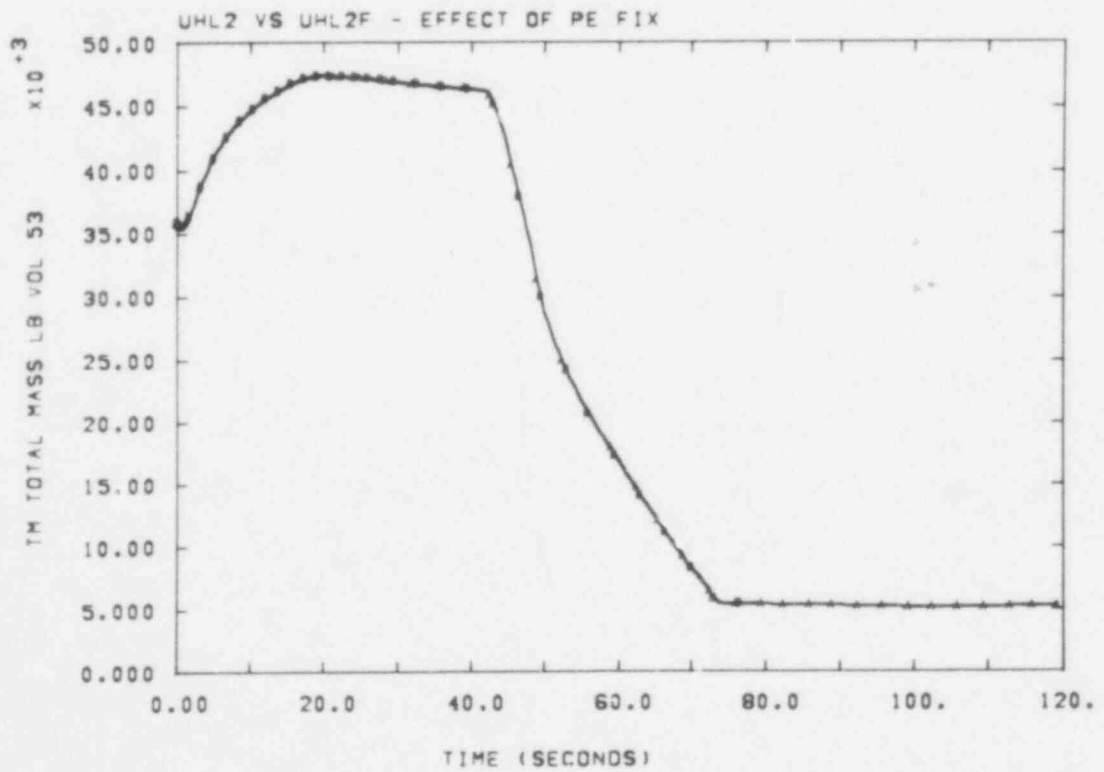
UHL2 VS UHL2F - EFFECT OF PE FIX

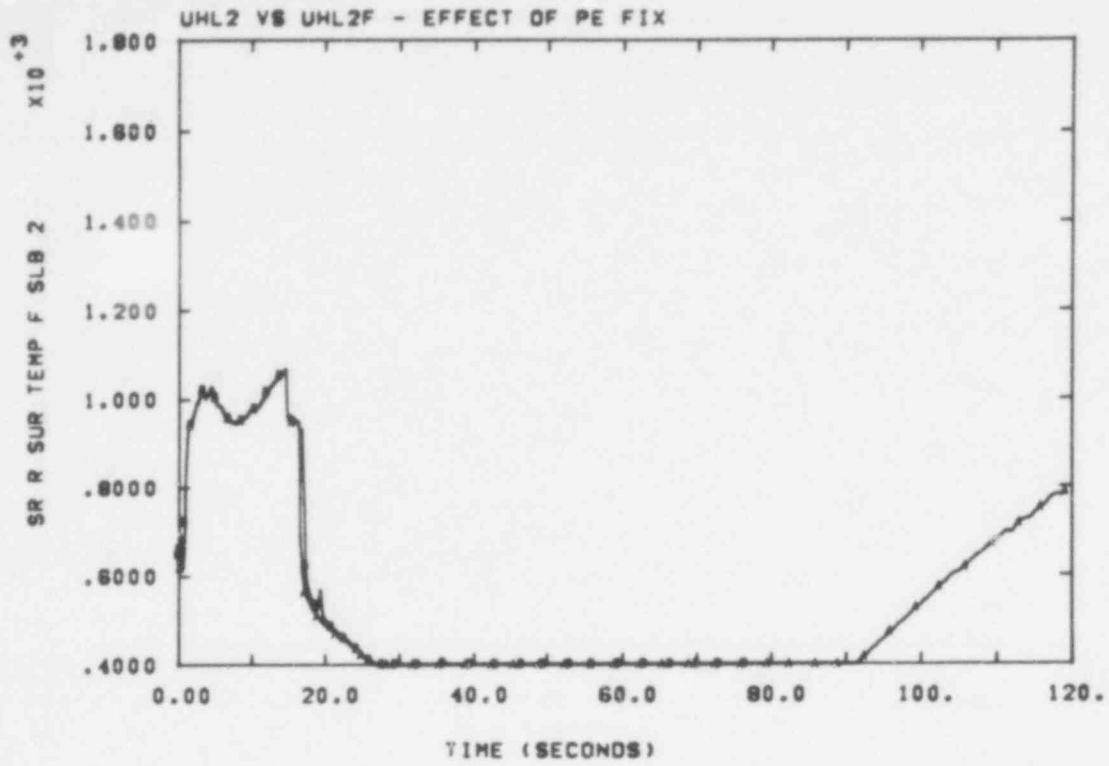Figure 4-3. Upper Head Mass, With and Without "PE Fix"

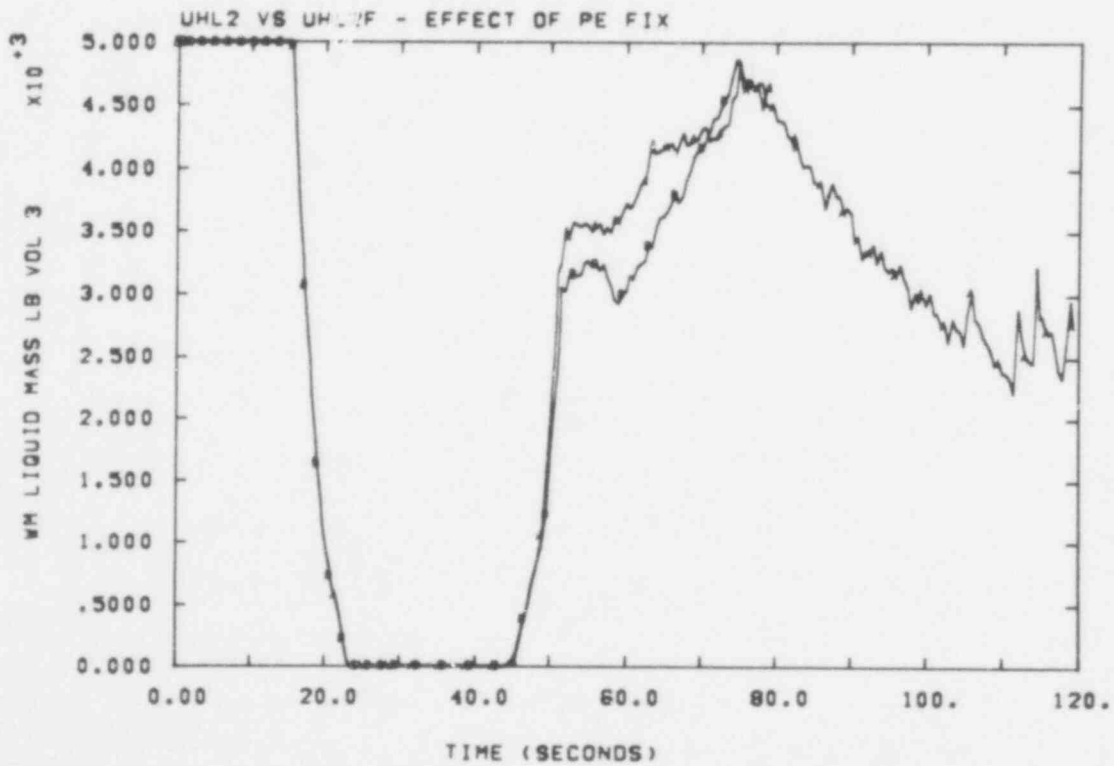Figure 4-4. Clad Temperature, With and Without "PE Fix"

Figure 4-5. Mass in Steam Generator Primary, With and Without "PE Fix"

86

467 274

4.2.2   Calculations with Generic Slip Correlation

Results from last quarter gave strong indications that Sandia's modifications to the NIFTE recycle logic were not the source of the flow oscillations observed in downcomer junctions. We therefore wished to determine whether the WZ correlation for the slip velocity could be at fault. The calculations called UHL2FT, UHL2FT-New, UHL2FS, and UHL2FD were run with various combinations of the "generic" slip velocity, as desribed in the RELAP4/MOD5 manual.[6] This correlation is of the form

$$VSL = V_{liq} - V_{gas} = (10 + S_1 \Delta\alpha) \, \bar{\alpha}_j \, (1 - \bar{\alpha}_j)^{1 - 1.25 \, \bar{\alpha}_j}$$

where

$\bar{\alpha}_j$ is Min $\left| \alpha_m, \text{ junction void fraction} \right|$,

$\Delta\alpha$ is Max $\left| 0, \, \alpha_{BELOW} - \alpha_{ABOVE} \right|$,

and

S_1 and α_m are input parameters.

In UHL2FT and UHL2FT-New, S_1 was chosen to have the value 4.0, and α_m was taken as 0.995. UHL2FT-New uses the RELAP4/MOD7 steam tables and associated routines.[7] These choices permit a maximum relative velocity (in the gravitationally stable case) of about 36 ft/s. The UHL2FS calculation used S_1 equal to 4.0 also, but α_m was chosen to be $1.0 - (1.0 \times 10^{-8})$, or 0.99999999. This permits a corresponding maximum relative velocity of about 1000 ft/s. The goal here was to determine whether the presence of very high relative velocities could account for slip-related difficulties. Finally, UHL2FD was run with $S_1 = 0.0$ and $\alpha_m = 0.995$; this was an attempt to check the effect of a discontinuity in the correlation when local conditions oscillate between gravitationally stable and unstable.

These calculations all ran very smoothly, and more efficiently than others in recent experience. See for example, Figures 4-6 and 4-7, comparing computational speeds against generic MOD5 and MOD6 calculations. In addition, UHL2FT, UHL2FS, and UHL2FT-New produced essentially identical results. Figures 4-8 and 4-9 compare downcomer flows and downcomer crossflows with and without the MOD7 water properties package. Similar comparisons for UHL2FT vs UHL2FS appear in Figures 4-10 and 4-11. These are regions where we have previously experienced significant difficulties and large slip velocities. Figures 4-10 and 4-11 also demonstrate that there is no significant effect on the large disparity in relative velocity permitted. This was true even of normally very sensitive quantities, such as quality in the core and guide tube volumes (Figures 4-12 and 4-13). In still other quantities, such as total stored energy and slab temperature (Figures 4-14 and 4-15), the plots show even smaller differences.
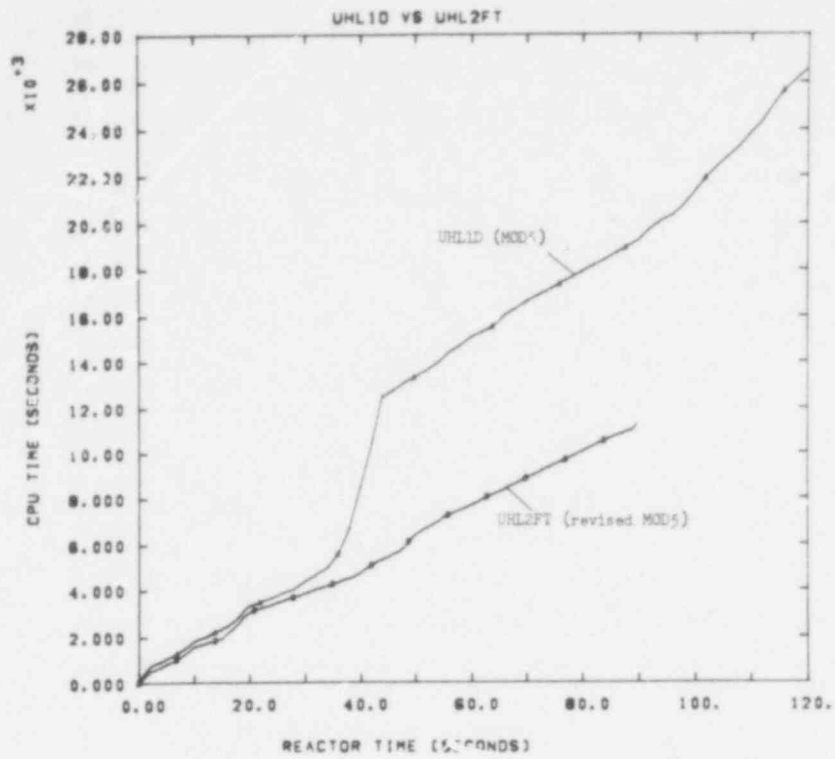
Figure 4-6. Computational Efficiency for Generic MOD5
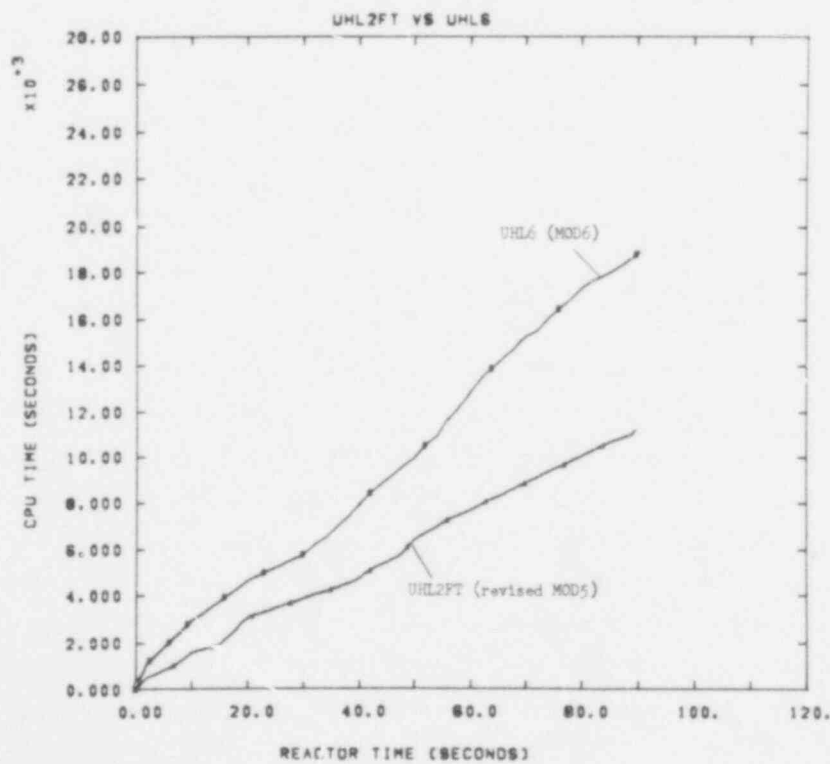and Revised MOD5 RELAP Calculations

Figure 4-7. Computational Efficiency for MOD6 and Revised
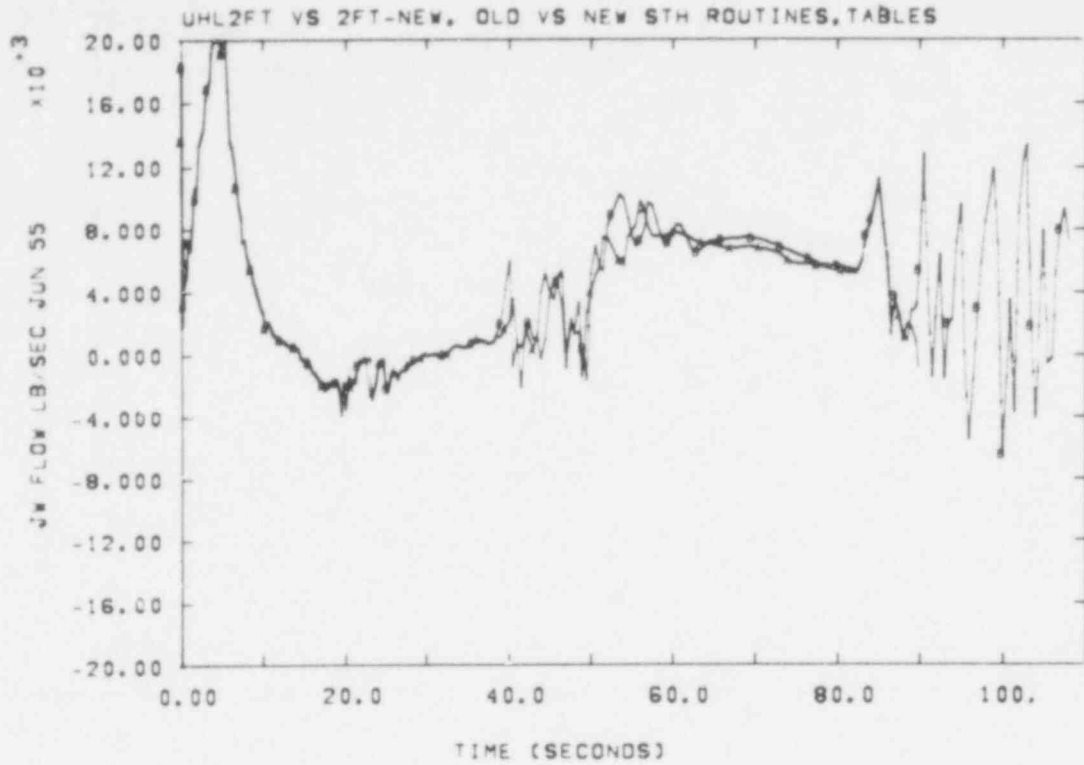MOD5 RELAP Calculations

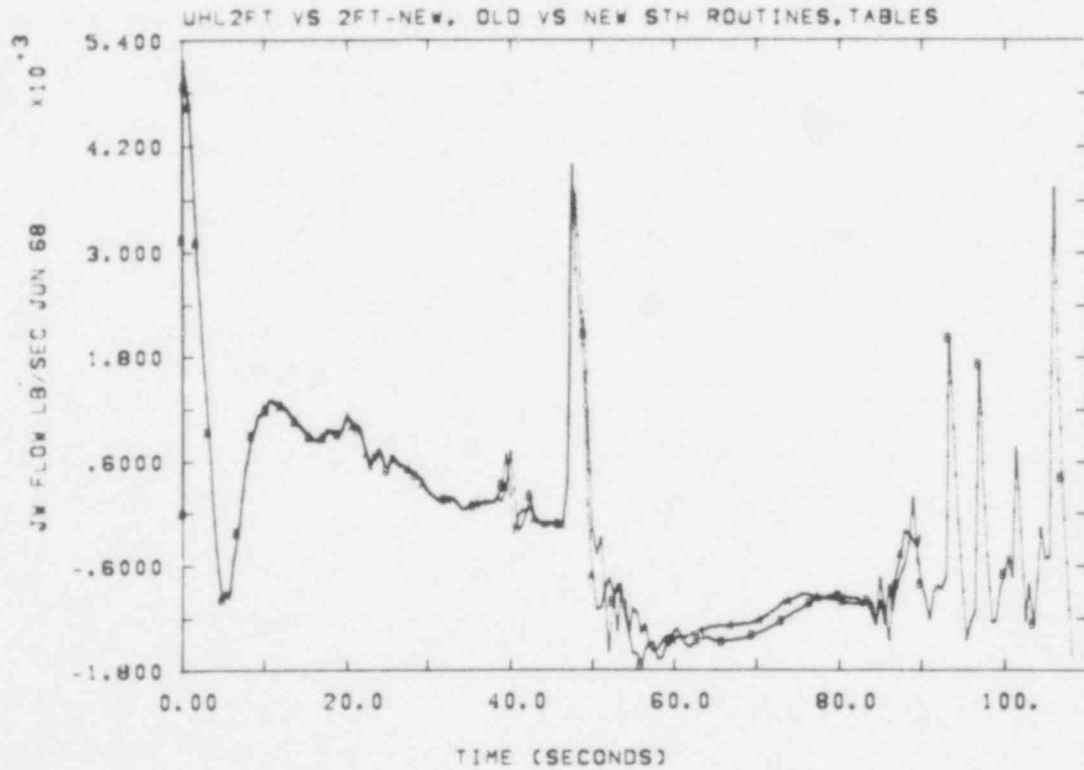Figure 4-8. Downcomer Flow, With and Without MOD7 Water Properties

Figure 4-9. Downcomer Crossflow, With and Without MOD7 Water Properties
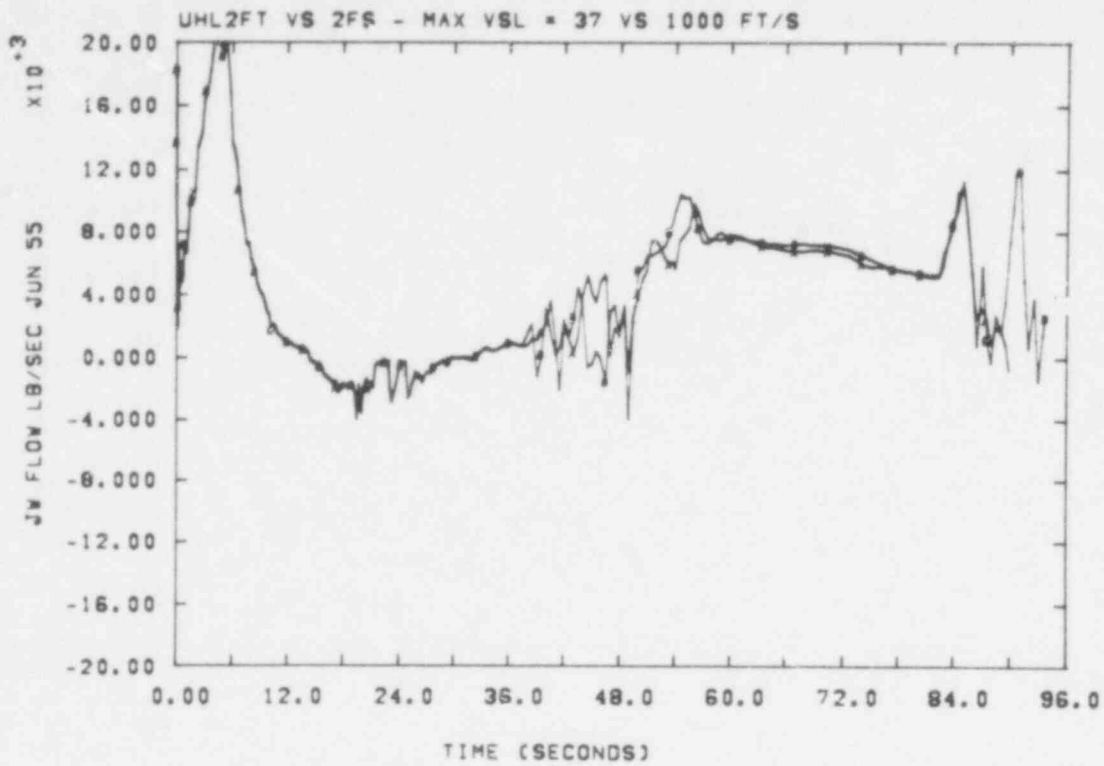
467 277

89

UHL2FT VS 2FS - MAX VSL = 37 VS 1000 FT/S

Figure 4-10. Downcomer Flow, α_m = 0.995 and 0.99999999
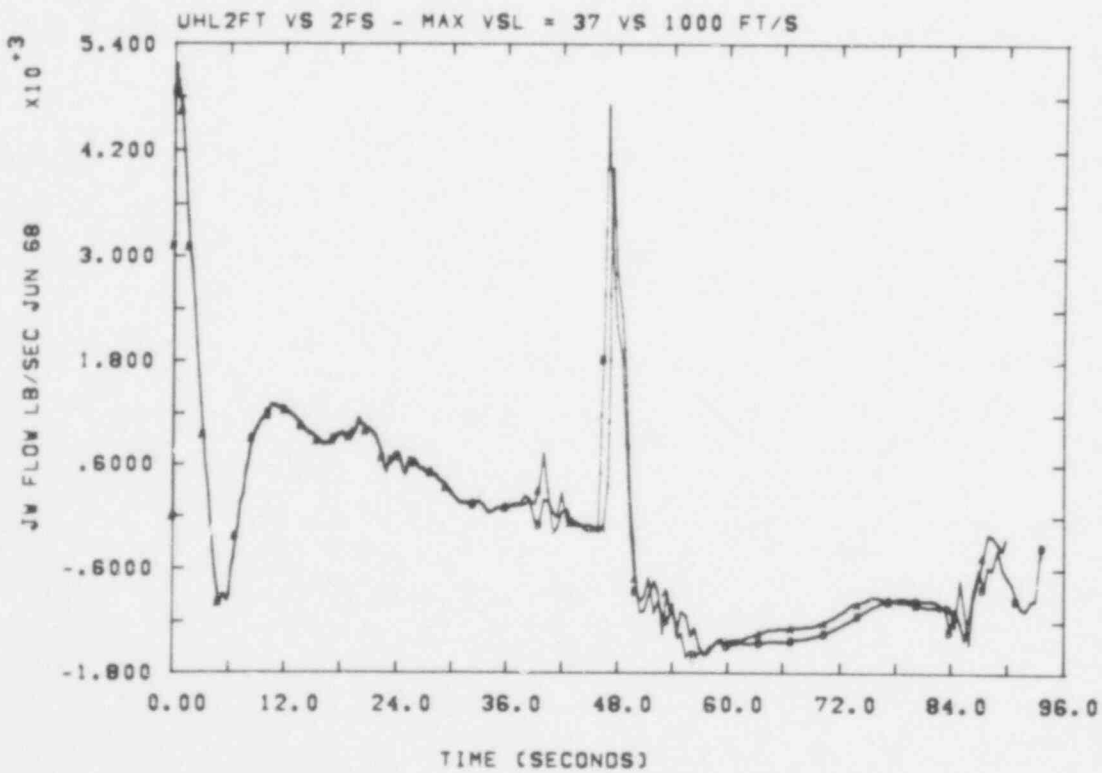

UHL2FT VS 2FS - MAX VSL = 37 VS 1000 FT/S

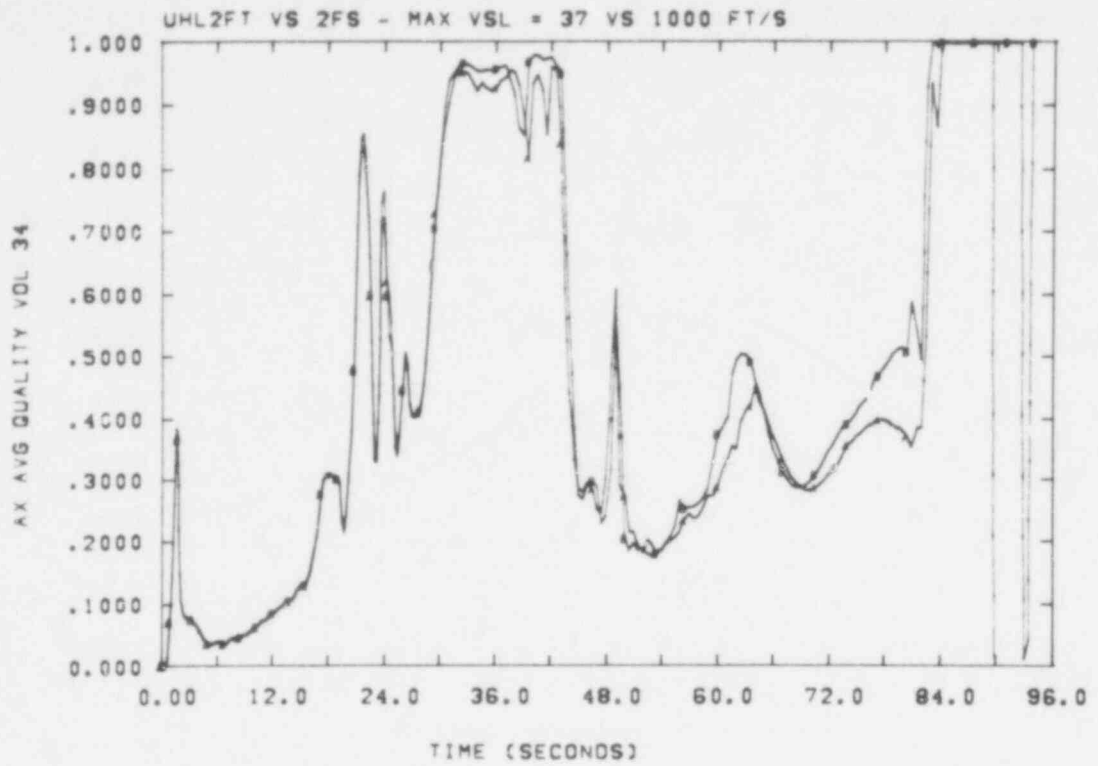Figure 4-11. Downcomer Crossflow, α_m = 0.995 and 0.99999999

90

Figure 4-12. Fluid Quality, Bottom Average Core Volume,
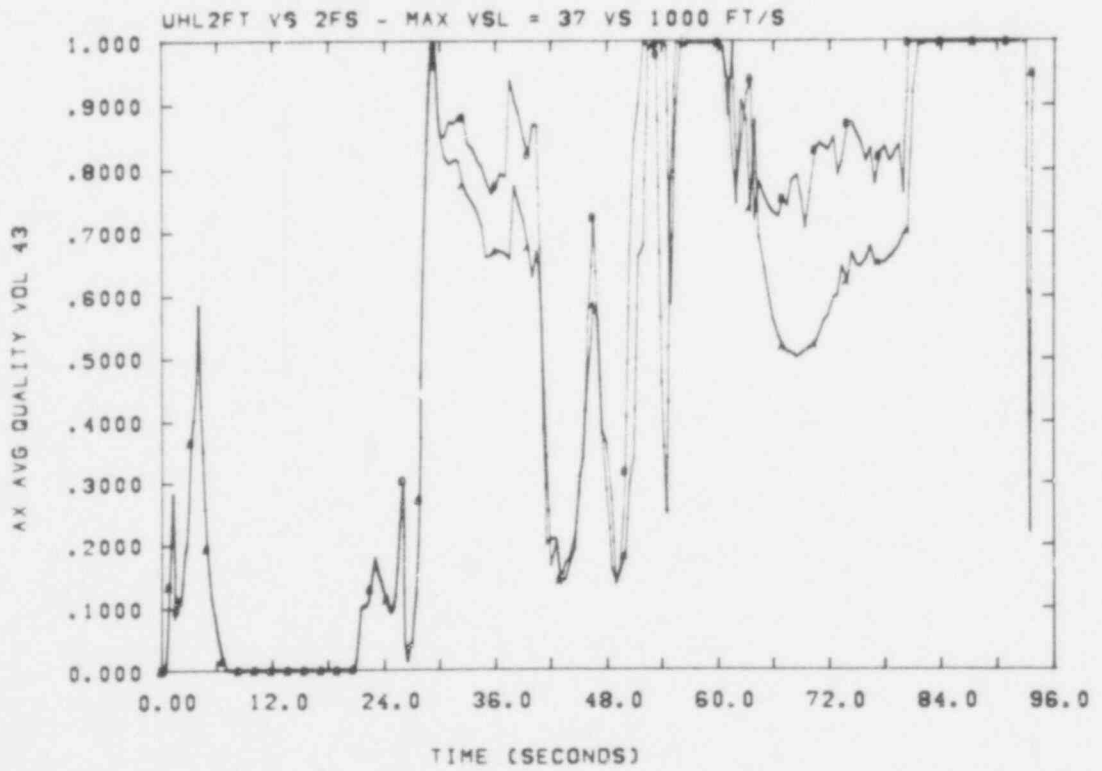α_m = 0.995 and 0.99999999

Figure 4-13. Fluid Quality, Lower Guide Tube Volume,
α_m = 0.995 and 0.99999999

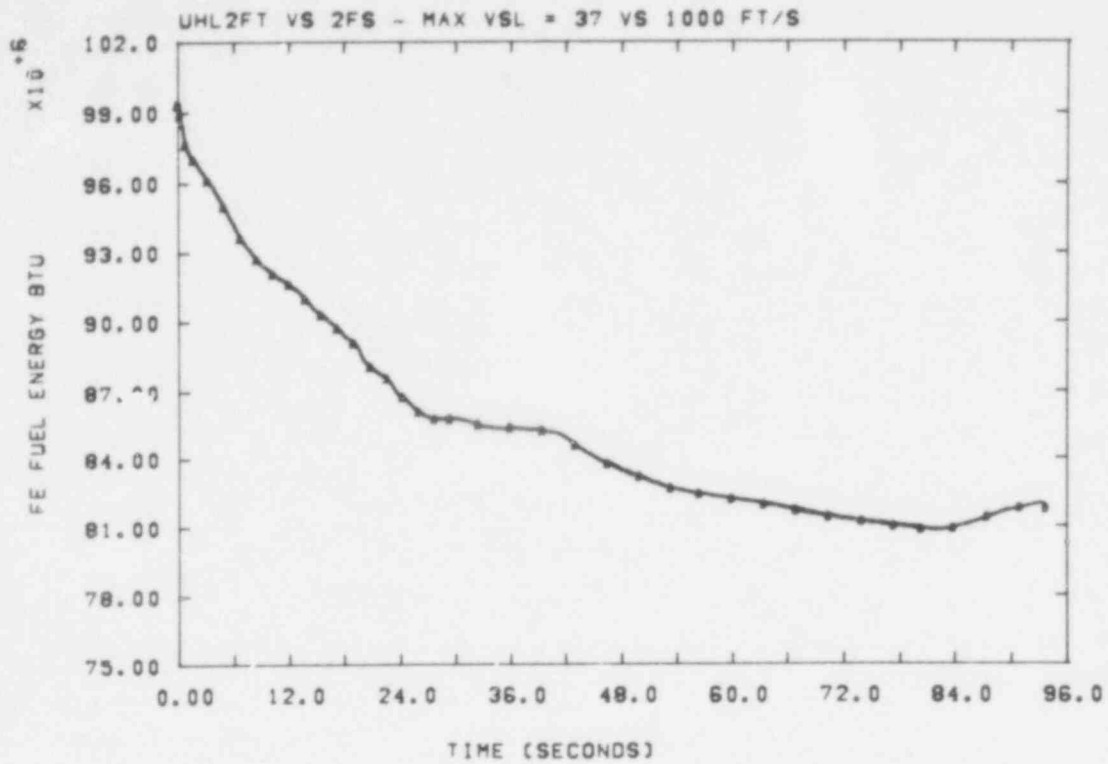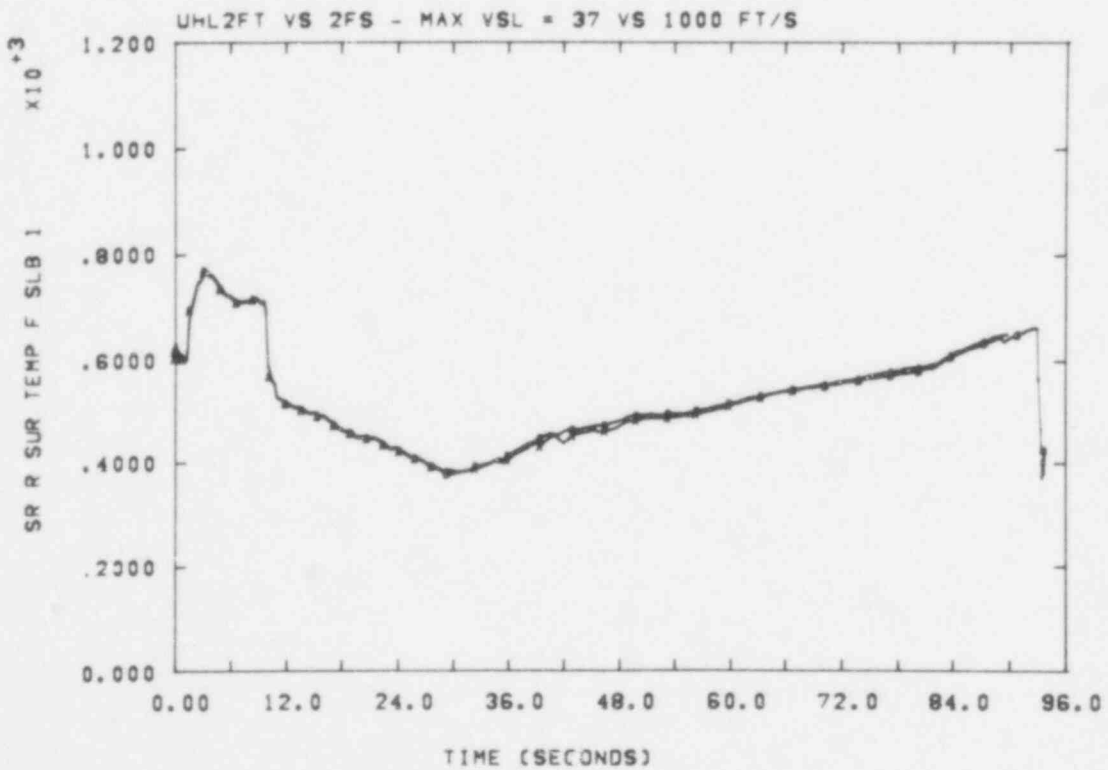Figure 4-14. Fuel Stored Energy, α_m = 0.995 and 0.99999999

Figure 4-15. Clad Temperature, α_m = 0.995 and 0.99999999

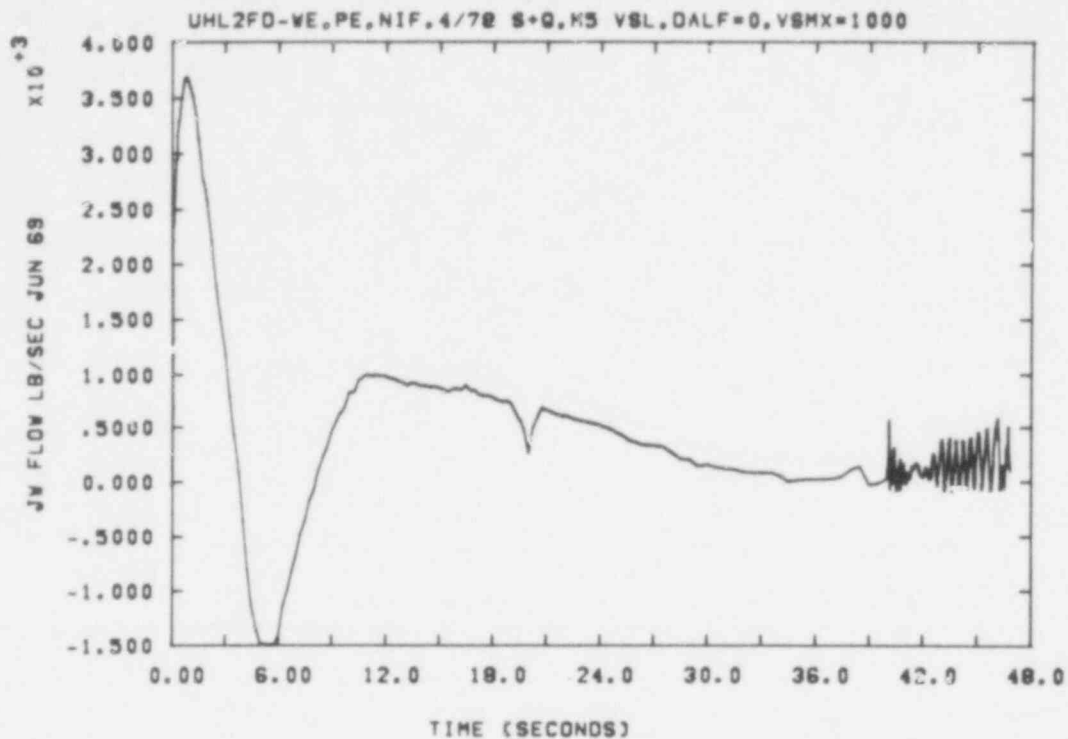UHL2FD-WE,PE,NIF,4/70 S+Q,K5 VSL,DALF=0,VSMX=1000

Figure 4-16. Downcomer Crossflow, No Void Fraction Difference Term

The only calculational difficulty we experienced in this series of runs was with UHL2FD, which had to be "coaxed" through a period around 40 s by means of a timestep alteration (Figure 4-16). Once this period of difficulty was passed, the calculation proceeded as well as the others.

In comparing these calculations with previous, generic, MOD5 results, the only other significant differences we observed were improvements in the calculations of the downcomer flows (Figures 4-17 through 4-19), and the early heat transfer associated with the different quench logic. Core slab temperature histories are shown in Figures 4-20 through 4-22. Quantities such as stored energy, upper head mass history, and drain flows were not markedly affected, as shown in Figures 4-23, 4-24, and 4-25, respectively.

We feel that these calculations provide strong evidence that the instability involves the slip correlation alone, and that the difficulty with the WZ correlation is more complicated than the relatively large slip velocities it permits.

An analysis of the stability of the basic differential equations has been performed, (see Section 4.3). We conclude that these equations are unstable (i.e., have complex characteristics) if the difference between the continuity-wave velocity and the average (mixture) velocity--that is, the velocity of a continuity wave relative to the mixture--is larger than some fraction of the sonic velocity. For the WZ correlation and countercurrent, or small cocurrent flow, this velocity difference in the transition region is much greater for the churn-turbulent-bubbly regime than for the film annular regime, which offers an explanation of the calculational instability problems.

93

467 201
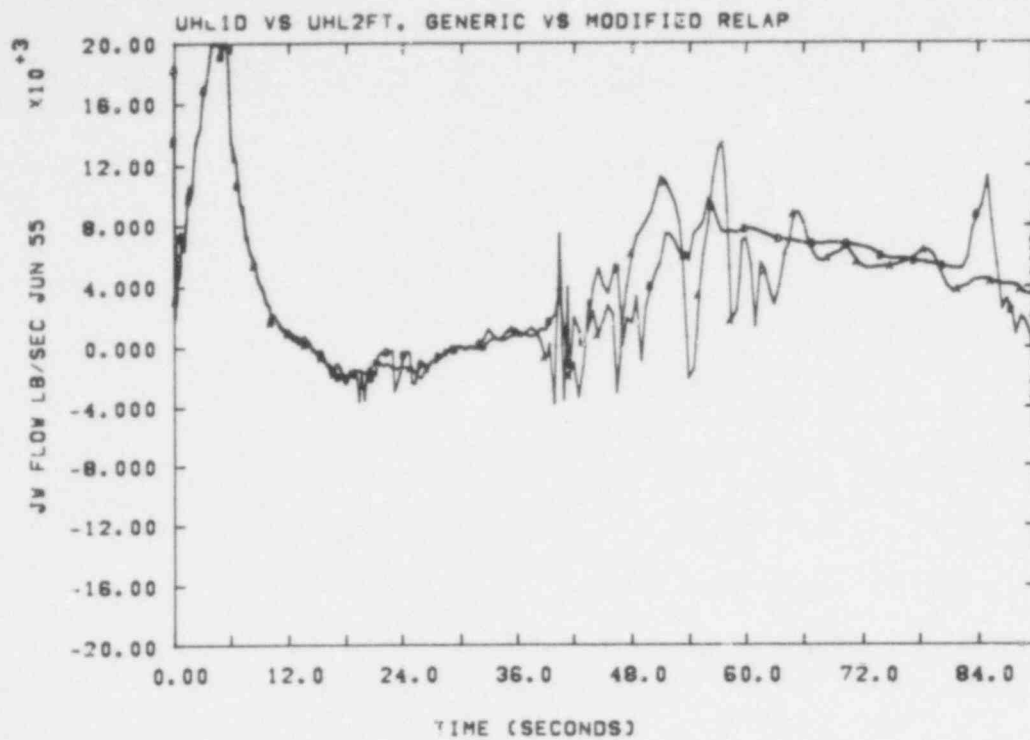
Figure 4-17. Downcomer Flow, Generic vs Modified RELAP
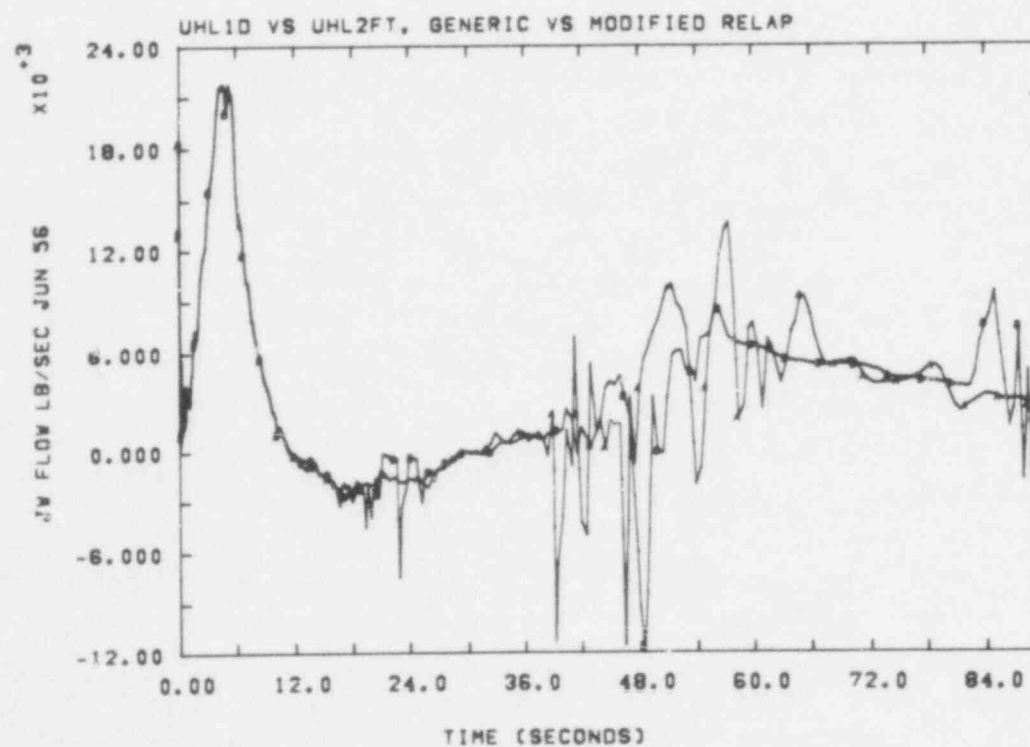
Figure 4-18. Flow to Lower Plenum, Generic vs Modified RELAP

467 282
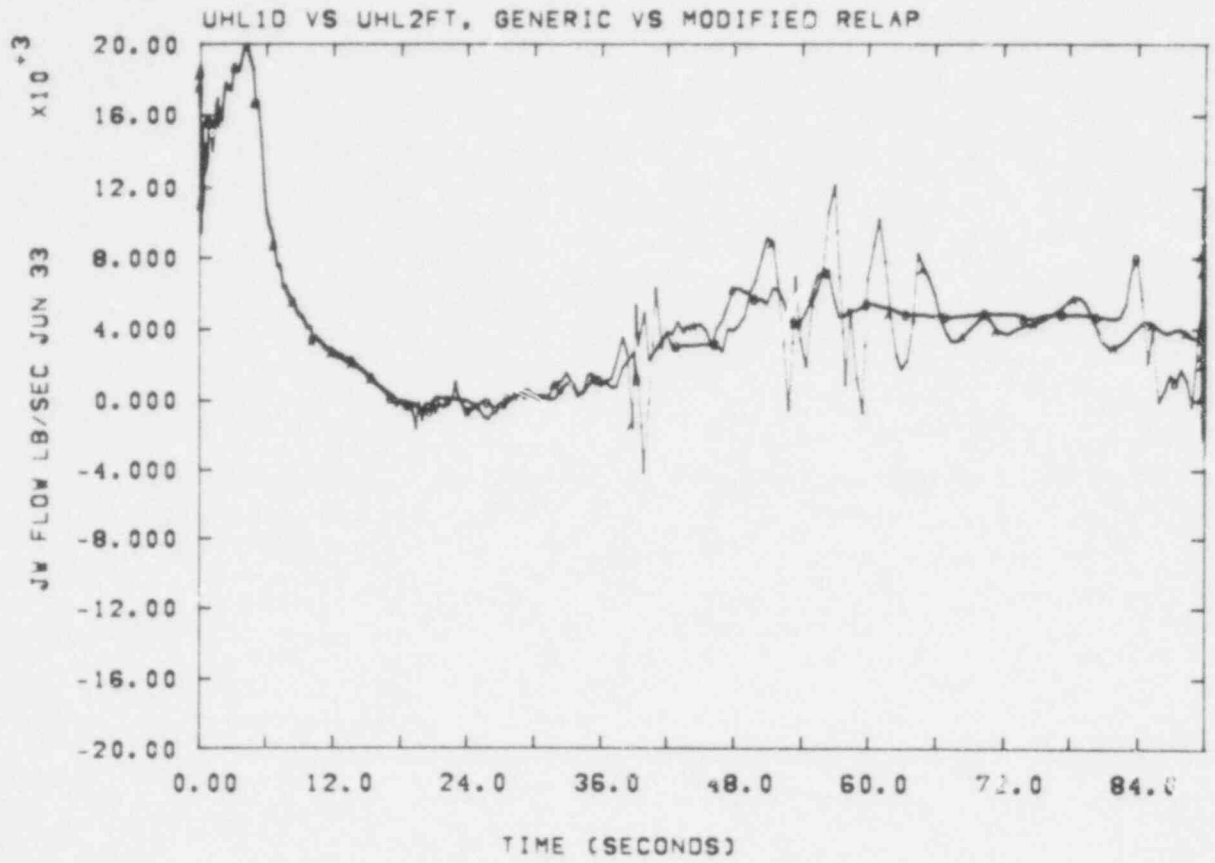
Figure 4-19. Flow to Downcomer, Generic vs Modified RELAP

95
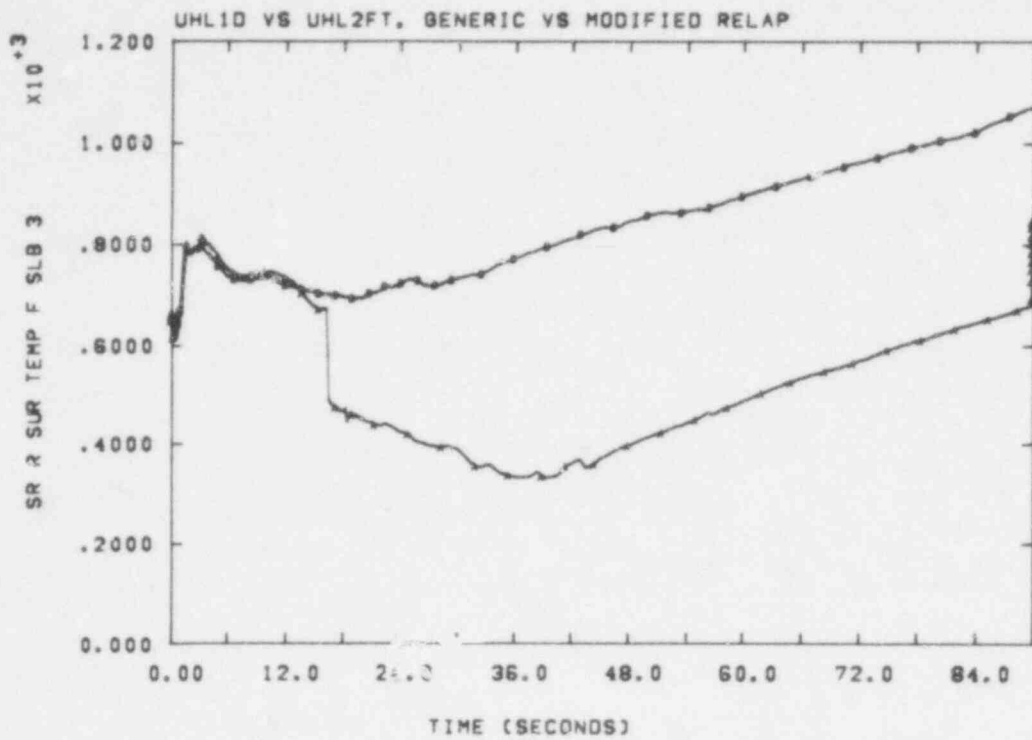
Figure 4-20. Clad Temperature, Top of Hot Assembly, Generic vs Modified RELAP
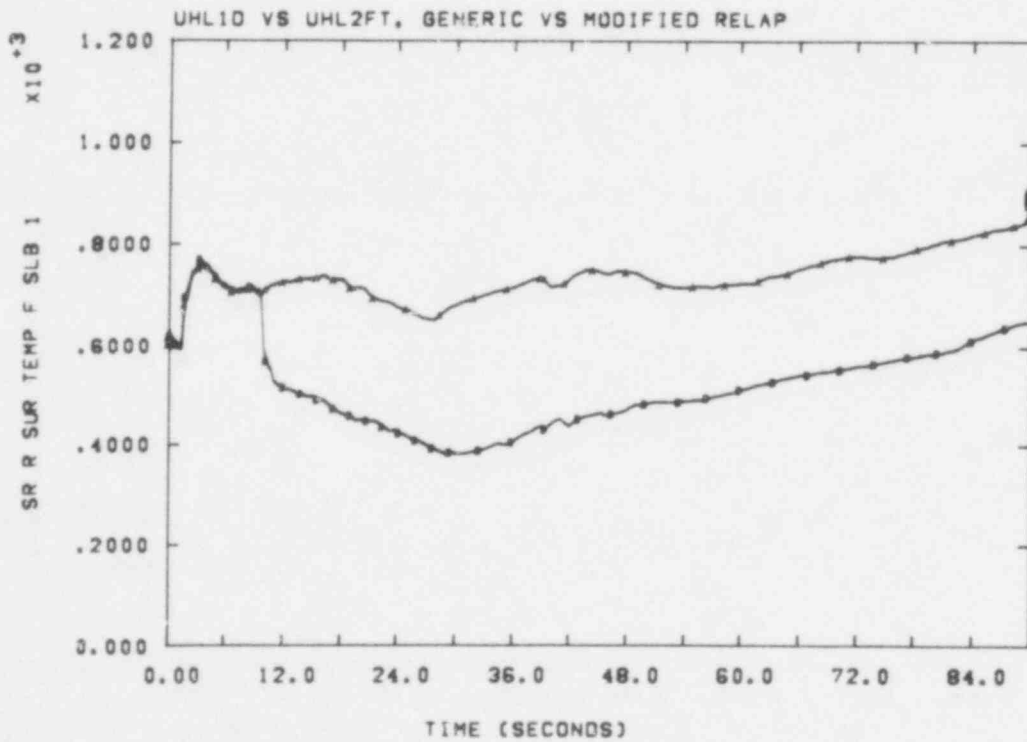
Figure 4-21. Clad Temperature, Bottom of Hot Assembly, Generic vs Modified RELAP

467 284

96
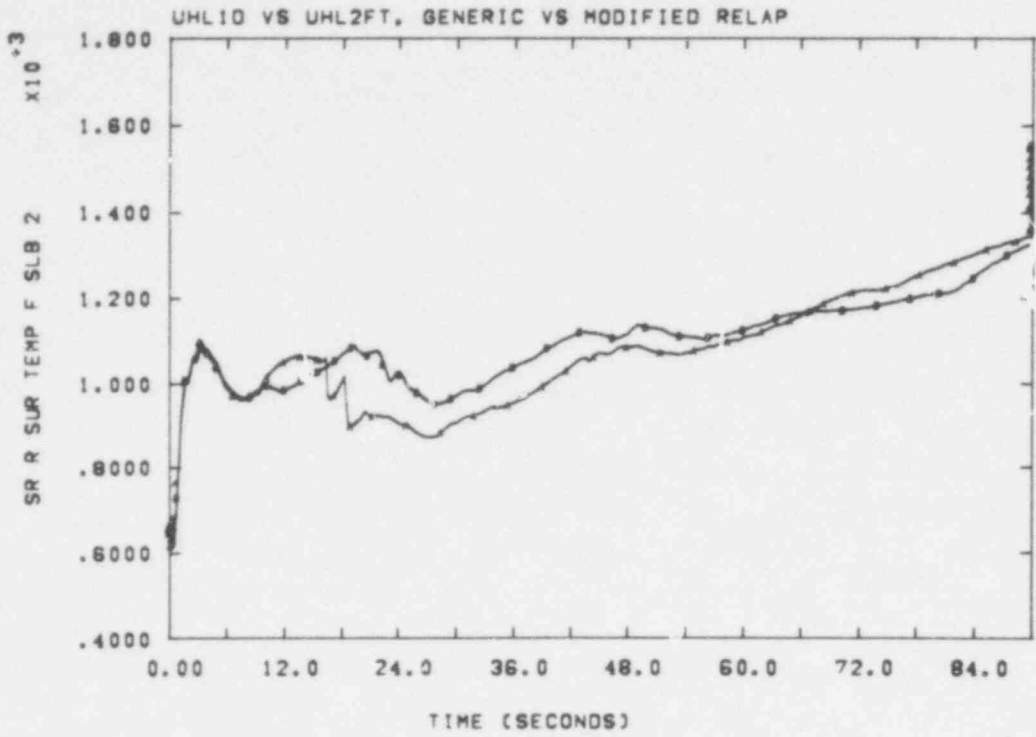
Figure 4-22. Clad Temperature, Middle of Hot Assembly, Generic vs Modified RELAP
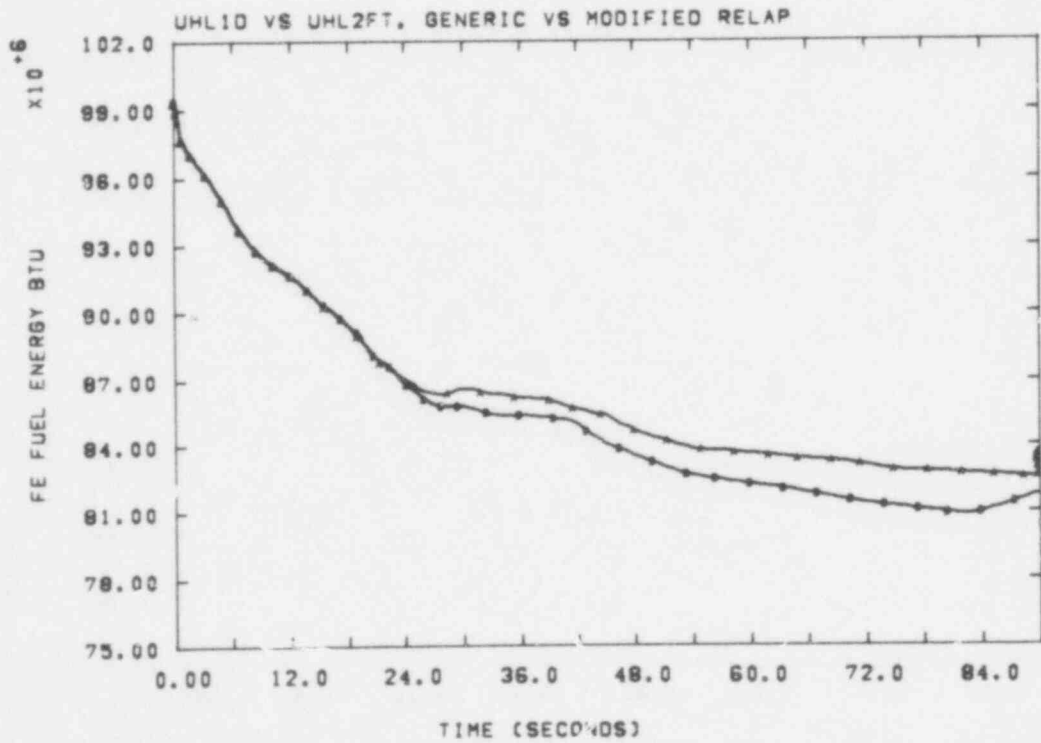
Figure 4-23. Fuel Stored Energy, Generic vs Modified RELAP

467 285

97

Figure 4-24. Mass in Upper Head, Generic vs Modified RELAP

Figure 4-25. Average Support Column Flow, Generic vs Modified RELAP

467 286

During this quarter, we became aware of relevant work done in Great Britain (RELAP-UK).[4][5] They concluded that the stability of the equations depends on the form of the slip correlation, with "profile slip" (or distribution parameter $C_o \neq 1$) being very important. The correlation used in RELAP-UK has been constructed to yield stable equations, essentially by making C_o a function o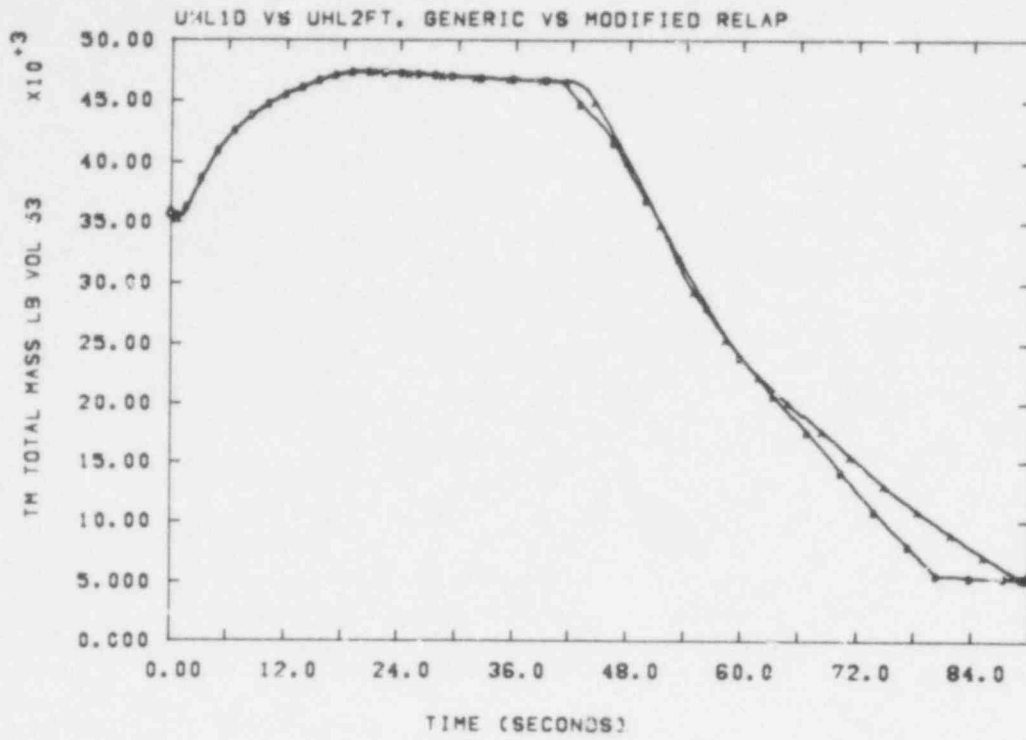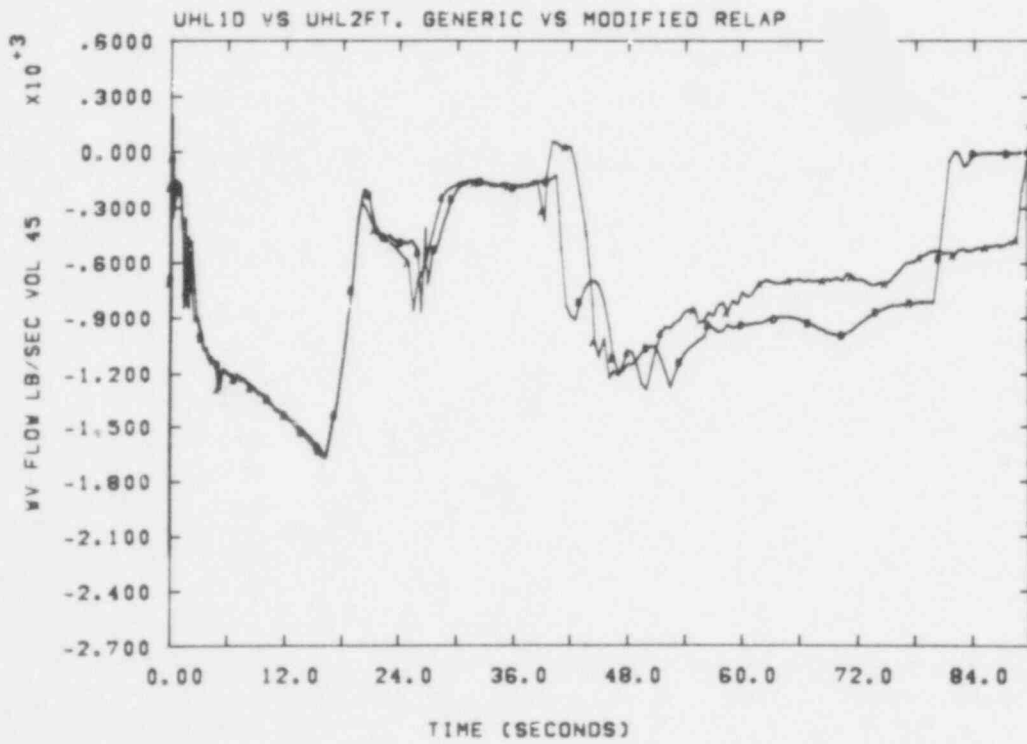f the net mass flux, G (which leads to a curved drift-flux line). We also note that RELAP-UK has a consistent junction void fraction, defined in a way which agrees with our prescription except for one case. This is the case of gravitationally unstable (low α above high α) countercurrent flow, where their prescription leads to a flow solution nearer to the flooding curve than does ours. We refer to this situation as "gravitationally unstable" because it corresponds to a high density mixture above a low density one, at least for the pressure below not much greater than the pressure above. The generic RELAP4/MOD5 correlation also has an enhancement of relative velocity for low α over high α, not limited to counter-current flow. In one of our calculations this enhancement was set to zero by an input parameter with no clear effect on calculational stability. Therefore, we have not pursued the idea of adding such a modification to the WZ correlation.

We are unsure at this point how best to proceed with slip-model development. The WZ correlation could perhaps be modified to give stable equations. The necessary modification is not obvious, and the resulting correlation would probably be quite different from the original. A change involving C_o as a function of mass flux (as in RELAP-UK) would require significant modification of the code. Also, it is somewhat disturbing that a correlation derived from experiment should lead to an instability; perhaps the form used for the conservation equations is involved in some manner. While we have not devoted much time to this possibility, it may be possible to cast the equations in a stable form only slightly more complicated than the present drift-flux form.

4.2.3 Calculations with a Smoothed Slip Correlation

As a final attempt to eliminate "triggers" for the observed slip instability, the continuous slip correlation described in Reference 1 was further modified to make the first derivatives of V_{gj} and C_o continuous. This was done by introducing quadratic (in α) transitions at all "corners". These were fit in the range where the candidate C_o's differed by less than 0.1, and where the V_{gj}'s differed by less than $0.2\,V_{gjB}$. Continuity of function and derivative fully defines each transition, and the equations may be easily derived. The correlations are illustrated in Figure 4-26.

A calculation, denoted UHL2G, was performed using this correlation and the UHL double-downcomer nodalization. The pressure in Volume 47 (the first downcomer node below nozzle elevation on the intact loop side), the void fraction, and the volumetric fluxes in Junction 54 (immediately below Volume 47) are shown in Figures 4-27, 4-28, and 4-29, respectively. An unphysical oscillation appears short after Junction 54 enters the transition region between film-annular and churn-turbulent-bubbly flow. Close examination suggests that it is the C_o transition which is responsible, as shown by the "step" in Figure 4-27 and the change of slope in Figure 4-29 at about 35.1 s when the C_o transitions are entered.
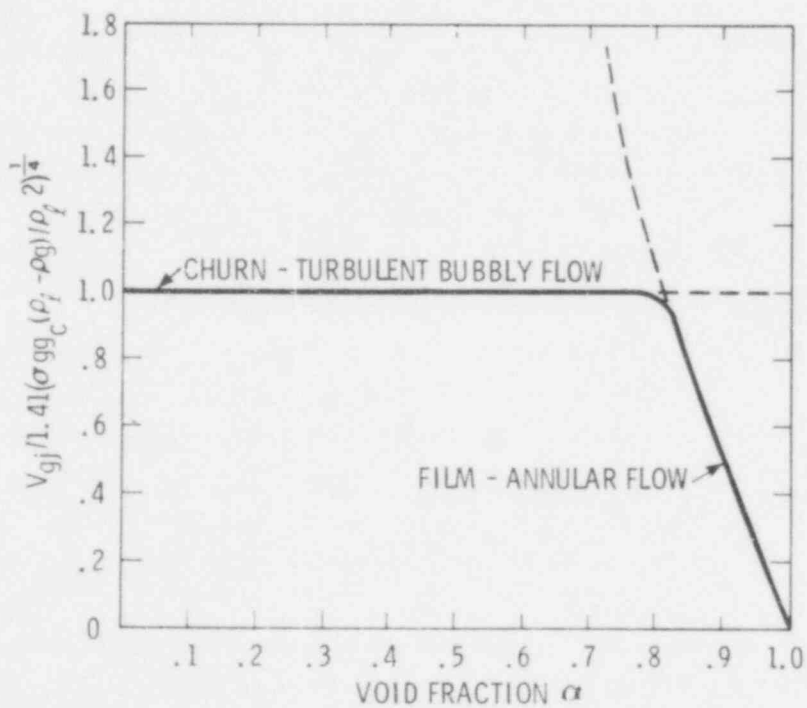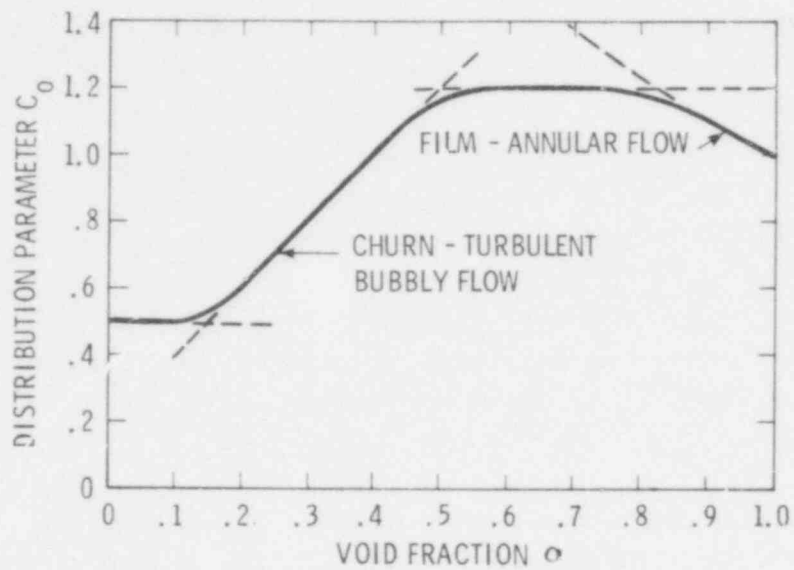
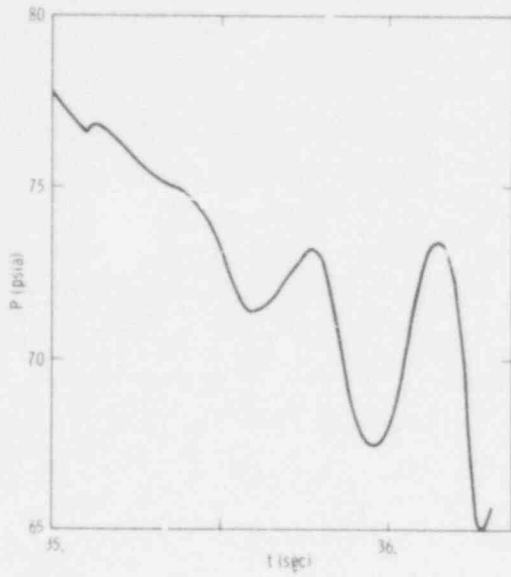Figure 4-26. Countercurrent Slip Parameters
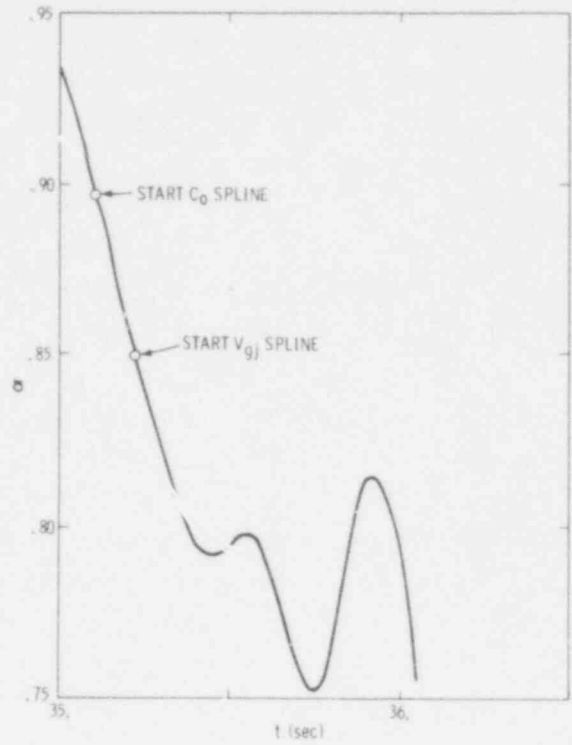
Figure 4-27. Pressure in Vol. 47

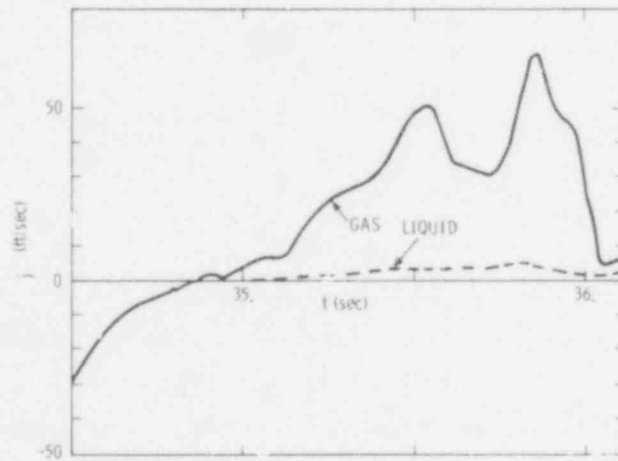Figure 4-28. Void Fraction in Junction 54, Below Vol. 47

Figure 4-29. Volumetric Fluxes in Junction 54, Below Vol. 47. Positive flow is down

Clearly, this approach does not completely solve the basic problem, and either a much greater change in the correlation or some change in the conservation equations is needed for stability.

A second calculation, UHL2C1, was performed using the spline-smoothed WZ correlation, but with C_o set to unity for cocurrent flow. This was motivated by the observations that, in generic MOD5 slip, C_o always takes this value, and the correlation used in RELAP-UK employs a C_o which approaches unity for high mass fluxes. We have not yet examined the results in great detail, but a brief inspection has led us to believe that there may be some merit in this technique.

Figures 4-30 and 4-31, showing flows from the downcomer to the lower plenum, indicate that some improvement has been achieved. Oscillations begin in both calculations, but -2G1 seems to recover. Figures 4-32 through 4-35 demonstrate that other quantities in the calculation do not seem strongly affected, although there is an as-yet-unexplained change in heat transfer in the core near 40 s. (See the temperature history in Fig. 4-35.) The flow improvements, however, seem encouraging, and we intend to pursue this method of calculation.

4.3 Stability of the Equations

We wish to investigate the stability of the general drift-flux model. The first step is to cast the partial differential equations describing the conservation of mass, of momentum, and of energy in characteristic form. In the absence of friction, gravity, and heat sources, the approximate one-dimensional forms used in RELAP 4 are

$$\frac{\partial}{\partial t} \rho + \frac{\partial}{\partial x} G = 0 , \tag{1}$$

$$\frac{\partial}{\partial t} G + \frac{\partial}{\partial x} P + (1-a) \frac{\partial}{\partial x} \left(\frac{G^2}{\rho} \right) = 0 , \tag{2}$$

$$\frac{\partial}{\partial t} \left\{ \rho \left[\varepsilon + \frac{1}{2} \left(\frac{G}{\rho} \right)^2 \right] \right\} + \frac{\partial}{\partial x} \left\{ \alpha v_g \rho_g h_g + (1 - \alpha) v_\ell \rho_\ell h_\ell + \frac{1}{2} \frac{G^3}{\rho^2} \right\} = 0 , \tag{3}$$

The notation is conventional, with subscripts ℓ and g referring to liquid and gas phases, respectively, while unsubscripted variables represent average (mixture) quantities. In Eq. (2), the coefficient a is 0 or 1 as momentum flux is included or neglected. In the presence of slip, Eq. (1) is correct, Eq. (2) neglects a term, $\partial/\partial x \left[\alpha(1 - \alpha) \rho_\ell \rho_g (v_g - v_\ell)^2/\rho \right]$, and Eq. (3) omits similar relative-velocity terms in the kinetic energy. These terms are at most comparable to the average momentum-flux term, $\partial/\partial x (G^2/\rho)$, which is often neglected in RELAP4 calculations.

UHL28-WIEST,PE,NIFTE,4/78 S AND Q,7/78 SLIP CORRN
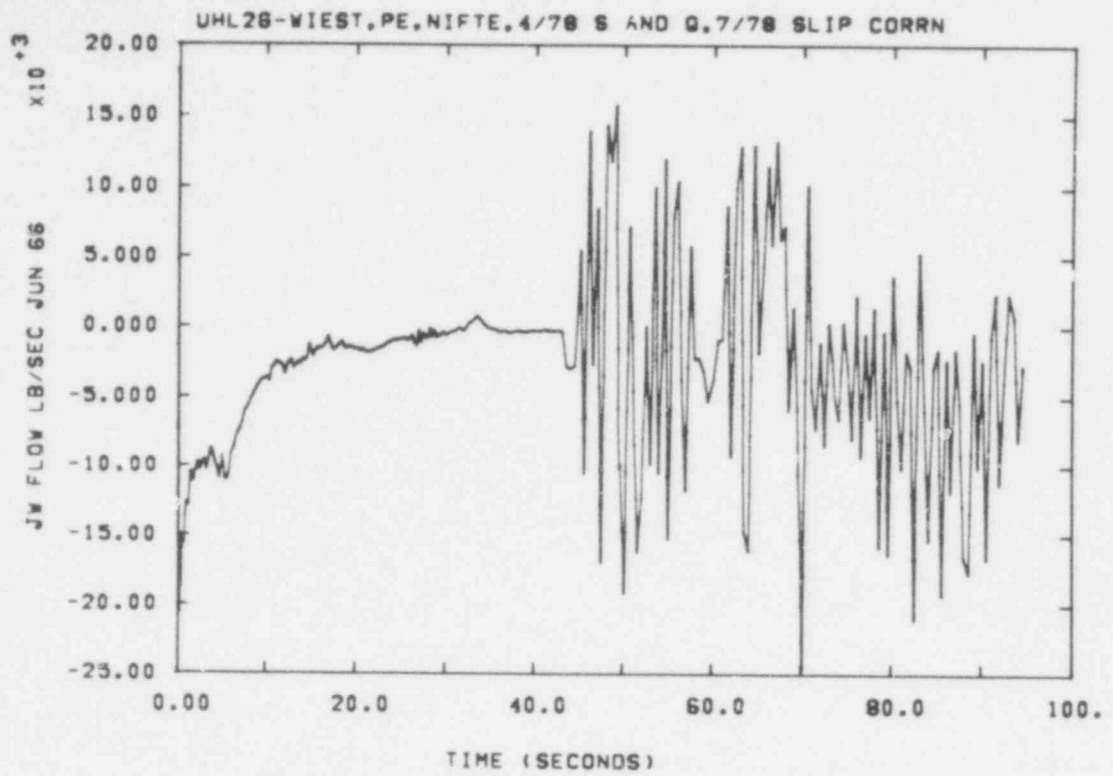
Figure 4-30. Flow to Lower Plenum, Spline-Smoothed Slip Correlation

UHL2G1-WE,PE,NIF,4/78 S+Q,7/78 S-S VSL,CO-CURR CO
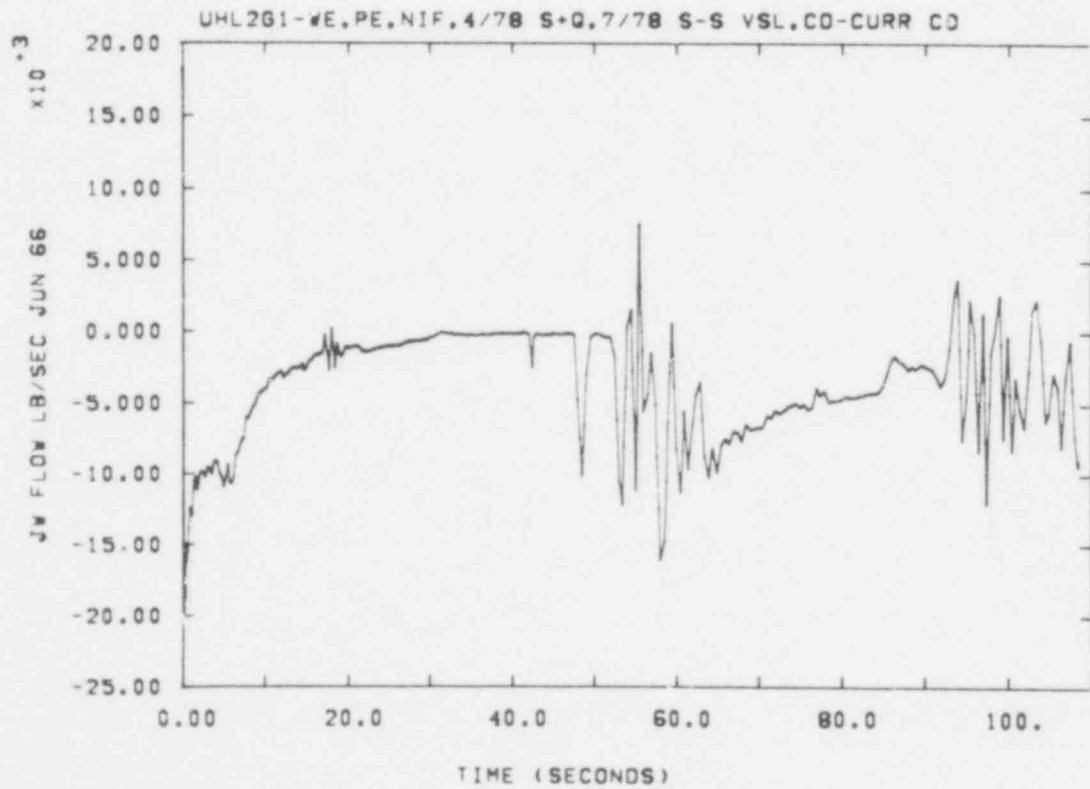
Figure 4-31. Flow to Lower Plenum, Spline-Smoothed Slip Correlation
With C_o = 1 for Cocurrent Flow

467   291
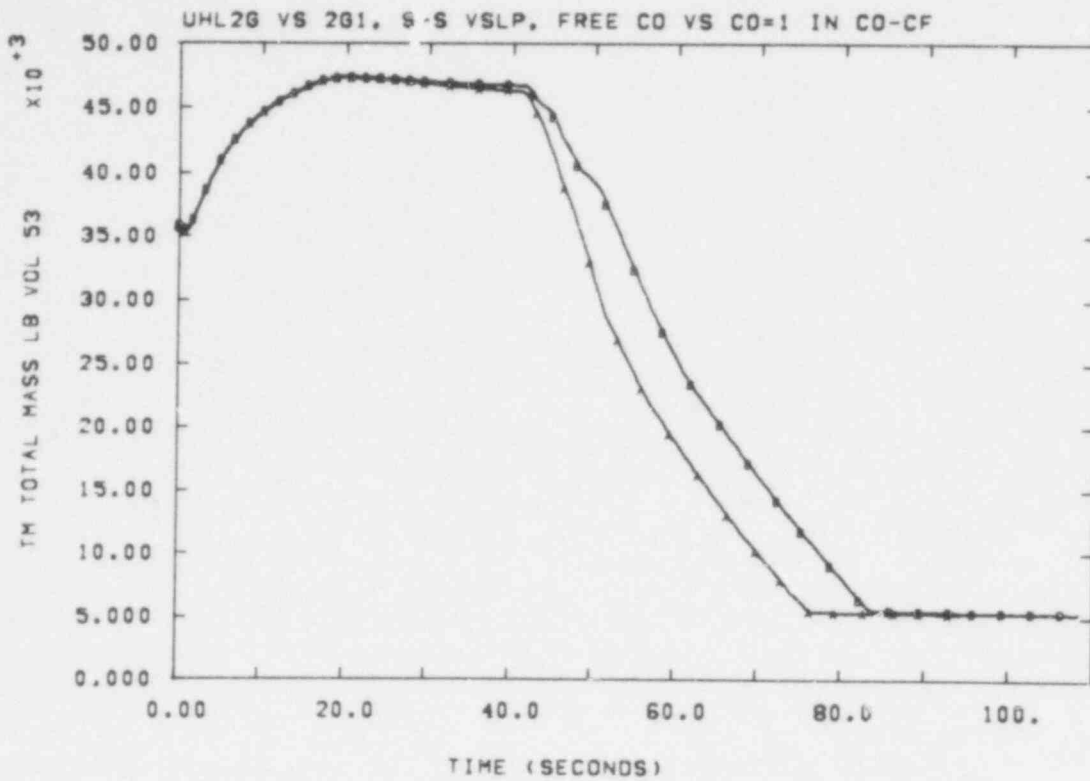
Figure 4-32. Upper Head Mass, Effect of Setting C_o to 1 for Cocurrent Flow
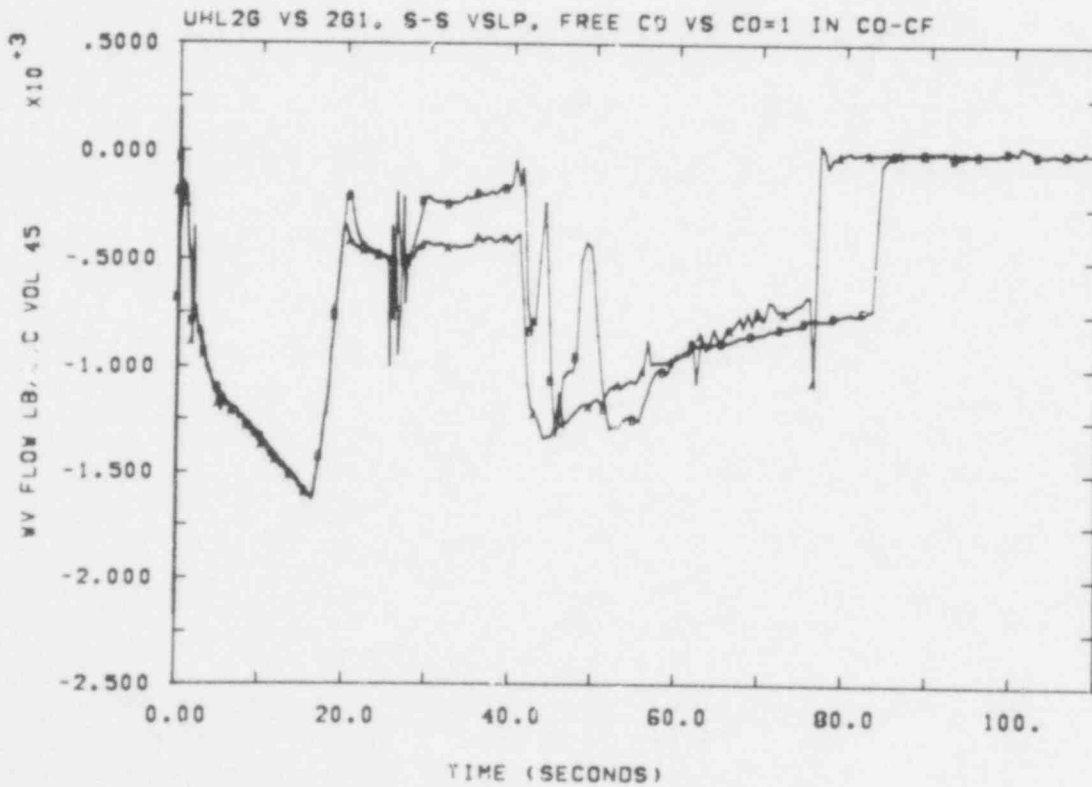
Figure 4-33. Support Column Flow, Effect of Setting C_o = 1 for Cocurrent Flow

UHL2G VS 2G1, S-S VSLP, FREE CO VS CO=1 IN CO-CF

FE FUEL ENERGY BTU   X10 +6

100.0
97.50
95.00
92.50
90.00
87.50
85.00
82.50
80.00
77.50
75.00

0.00   20.0   40.0   60.0   80.0   100.

TIME (SECONDS)
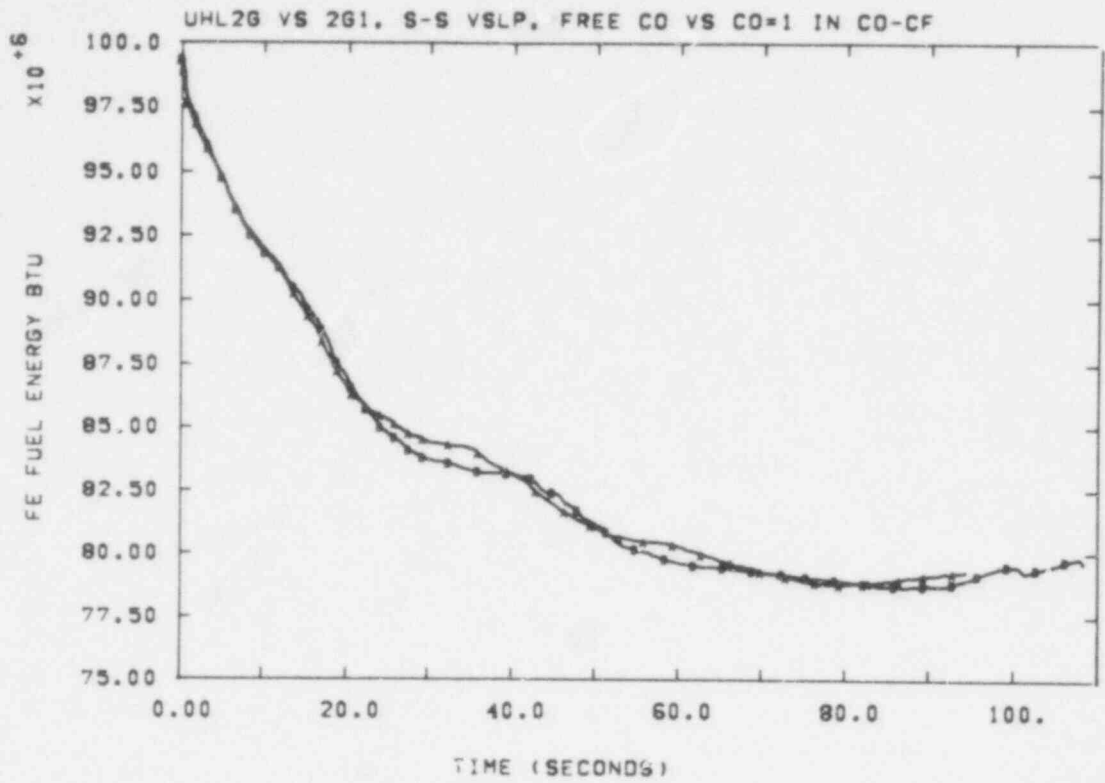
Figure 4-34. Fuel Stored Energy for Calculations With
Spline-Smoothed Slip Correlations

UHL2G VS 2G1, S-S VSLP, FREE CO VS CO=1 IN CO-CF

SR R SUR TEMP F SLB 1   X10 +3

1.200
1.100
.8000
.6000
.4000
.2000
0.000

0.00   20.0   40.0   60.0   80.0   100.

TIME (SECONDS)
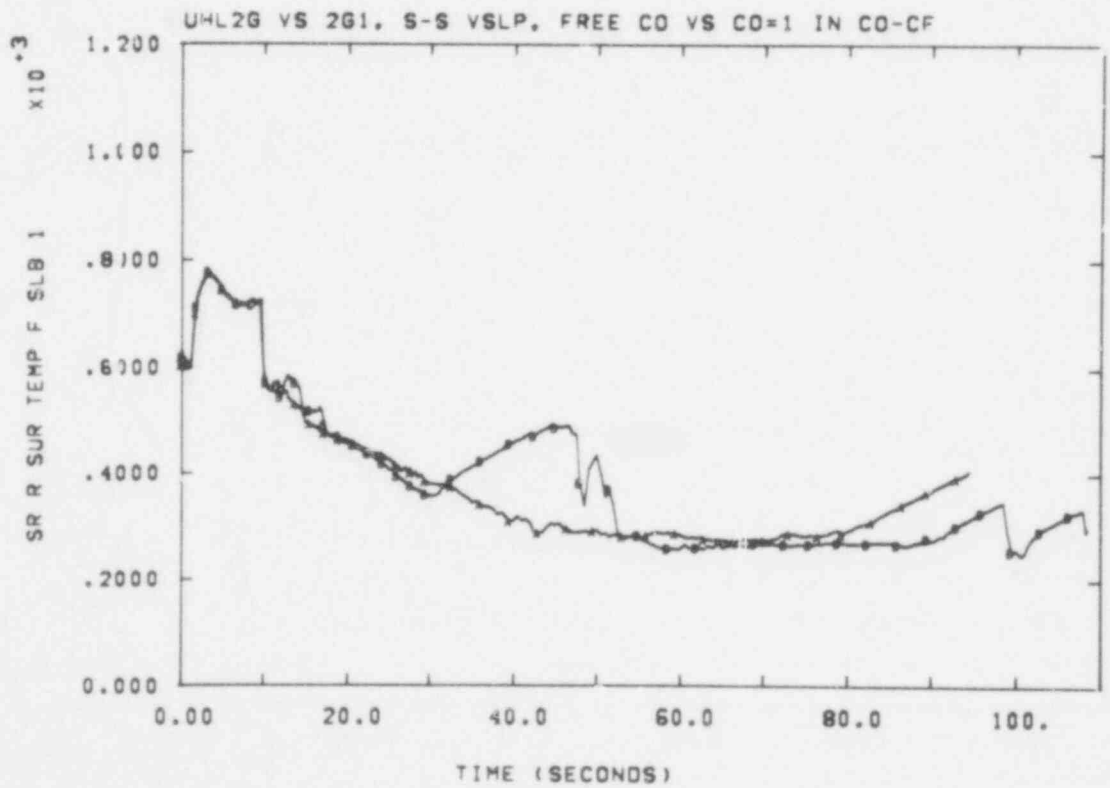
Figure 4-35. Clad Temperatures for Calculations With
Spline-Smoothed Slip Correlations

467 293

105

The energy equation may be simplifed by noting that

$$\alpha\, \rho_g v_g h_g + (1 - \alpha)\rho_\ell v_\ell h_\ell = \rho h U + (j - U)T\, \frac{dP_{Sat}}{dT} \, , \tag{4}$$

where

$$j = \alpha v_g + (1 - \alpha)v_\ell \tag{5}$$

is the volumetric flux,

$$U = G/\rho \tag{6}$$

is the average (mixture) velocity, and

$$\frac{dP_{Sat}}{dT} = \frac{\rho_\ell\, \rho_g}{\rho_\ell - \rho_g}\, \frac{h_g - h_\ell}{T} \tag{7}$$

is the slope of the saturation line. Note that Eq. (4) is still correct for a single-phase state: if $\alpha = 0$ or 1, $j-U = 0$

The conservation equations m   ow be put in the form

$$\left(\frac{\partial}{\partial t} + U\, \frac{\partial}{\partial x}\right)\, \rho + \rho \frac{\partial}{\partial x}\, U = 0 \tag{8}$$

$$\left(\frac{\partial}{\partial t} + U\, \frac{\partial}{\partial x}\right)\, U + \frac{1}{\rho}\, \frac{\partial}{\partial x}\, P - \frac{a}{\rho}\, \frac{\partial}{\partial x}\left(\rho U^2\right) = 0 \tag{9}$$

$$T\left(\frac{\partial}{\partial t} + U\, \frac{\partial}{\partial x}\right)\, S + \frac{a}{\rho}\, U\, \frac{\partial}{\partial x}\, \left(\rho U^2\right) + \frac{1}{\rho}\, \frac{\partial}{\partial x}\left[(j-U)\, T\, \frac{dP_{Sat}}{dT}\right] = 0. \tag{10}$$

In deriving Eq. (10) the differential relations $d\varepsilon = TdS + (P/\rho^2)\, d\rho$ and $dh = TdS + (1/\rho)\, dP$ were used, as was Eq. (4). If momentum flux is included (a=0) and there is no slip (j=U), Eq. (10) gives the conventional result that S is constant on the material characteristic $dx = Udt$. Finally, we form the pressure equation from the relation

$$dP = \left(\frac{\partial P}{\partial \rho}\right)_S\, d\rho + \left(\frac{\partial P}{\partial S}\right)_\rho\, dS, \tag{11}$$

noting that

$$\left(\frac{\partial P}{\partial \rho}\right)_S \equiv c^2 , \tag{12}$$

where c is the equilibrium sonic velocity. The final term of Eq. (10) is nonzero only for a two-phase state. Therefore in this term we may use

$$\left(\frac{\partial P}{\partial S}\right)_\rho = \rho^2 c^2 \left(\frac{\partial T}{\partial P}\right)_S \overset{\text{two-phase}}{=} \rho^2 c^2 \Big/ \frac{dP_{Sat}}{dT} \tag{13}$$

The resulting pressure equation is

$$\left(\frac{\partial}{\partial t} + U \frac{\partial}{\partial x}\right) P + \rho c^2 \frac{\partial}{\partial x} j = -\gamma a U \frac{\partial}{\partial x} \left(\rho U^2\right) - \rho c^2 (\; - U) \frac{\partial}{\partial x} \left[\ell n \left(T \frac{dP_{Sat}}{dT}\right)\right] \tag{14}$$

where

$$\gamma = \frac{1}{\rho T} \left(\frac{\partial P}{\partial S}\right)_\rho = \frac{1}{\rho} \left(\frac{\partial P}{\partial \varepsilon}\right)_\rho \tag{15}$$

is the Grueneisen ratio.

In the drift-flux model, the set of Eqs. (8), (9), and (14) is closed by prescribing j as a function of ρ, G, and P with P serving to determine the phase densities ρ_ℓ and ρ_g. This allows some simplifications. We start with

$$dj = \left(\frac{\partial j}{\partial G}\right)_{\rho, P} \left[dG - \left(\frac{\partial G}{\partial \rho}\right)_{j, P} d\rho\right] + \left(\frac{\partial j}{\partial P}\right)_{\rho, \;} dP, \tag{16}$$

and use

$$\left(\frac{\partial G}{\partial \rho}\right)_{j, P} = \begin{cases} U & \text{single phase} \\[2ex] \dfrac{(\partial G/\partial \alpha)_{j, P}}{(\partial \rho/\partial \alpha)_{j, P}} = v_{CW} & \text{two phase} \end{cases} \tag{17}$$

where

$$v_{CW} \equiv \left(\frac{\partial(\alpha v_g)}{\partial \alpha}\right)_{j, P} = - \left(\frac{\partial (1 - \alpha) v_\ell}{\partial \alpha}\right)_{j, P} \tag{18}$$

is the velocity of a continuity wave. Making the obvious interpretation that the continuity-wave velocity in a single-phase material is the particle velocity U, Eq. (14) becomes

$$\left(\frac{\partial}{\partial t} + U\frac{\partial}{\partial x}\right)P + \rho\left(\tilde{c}^2 + 2a\gamma U^2\right)\frac{\partial U}{\partial x} + \left[\tilde{c}^2(U - v_{CW}) + a\gamma U^3\right]\frac{\partial \rho}{\partial x} + j^*\frac{\partial P}{\partial x} = 0,\qquad (19)$$

where

$$\tilde{c}^2 = c^2\left(\frac{\partial j}{\partial U}\right)_{\rho,\,P}\qquad\qquad (20)$$

$$j^* = \rho c^2\left[\left(\frac{\partial j}{\partial P}\right)_U + \frac{(j - U)}{TdP_{Sat}/dT}\left(1 + \frac{Td^2P_{Sat}/dT^2}{dP_{Sat}/dT}\right)\right]\qquad (21)$$

Note that the γ term is absent if momentum flux is included and that $v_{CW} \to U$, $\tilde{c}^2 \to c$ and $j^* \to 0$ for a single-phase material. Eqs. 8, 9, and 19 may be written in matrix form as

$$\left[\frac{\partial}{\partial t} + (U + \underset{\approx}{A})\frac{\partial}{\partial x}\right]\begin{pmatrix}\rho \\ U \\ P\end{pmatrix} = 0.\qquad (22)$$

If λ is an eigenvalue of $\underset{\approx}{A}$, $U + \lambda$ is the slope of a characteristic; that is, $U + \lambda$ is the velocity of some "signal" in the mixture. For stability, all three eigenvalues must be real.

For the simplest case, momentum flux included and no slip, the matrix is

$$\underset{\approx}{A} = \begin{bmatrix} 0 & \rho & 0 \\ 0 & 0 & 1/\rho \\ 0 & \rho c^2 & U \end{bmatrix}\qquad\text{M.F., no slip,}\qquad (23)$$

for which the characteristic polynomial and its roots are

$$\lambda^3 - \lambda c^2 = 0$$
$$\lambda = 0, \pm c\qquad\qquad\text{M.F., no slip,}\qquad (24)$$

That is, signals are propagated with velocities U, U ± c.

If there is no slip, and the momentum flux term is neglected (a=1),

$$
\underset{\sim}{A} = \begin{bmatrix} 0 & \rho & 0 \\ -U^2/\rho & -2U & 1/\rho \\ \gamma U^3 & \rho(c^2 + 2\gamma U^2) & 0 \end{bmatrix} \qquad \text{no M. F., no slip} \tag{25}
$$

and the characteristic polynomial is

$$
\lambda^3 + 2U\lambda^2 - (\tilde{c}^2 + (2\gamma - 1) U^2)\lambda - \gamma U^3 = 0 . \tag{26}
$$

This polynomial has real roots, and the equations are stable, if and only if

$$
U^2 \left[c^2 + (\frac{1}{2}\gamma - \frac{1}{9}) U^2 \right] \leq \frac{1}{3} \left[c^2 + (2\gamma + \frac{1}{3}) U^2 \right]^3 \tag{27}
$$

While far from obvious, it may be shown that Eq. (27) _is_ satisfied for all U so long as $\gamma \geqslant 0$. Therefore, the homogeneous equations neglecting momentum flux are stable, even though they are clearly not correct for supersonic flow.

With inclusion of both slip and momentum flux,

$$
\underset{\sim}{A} = \begin{bmatrix} 0 & \rho & 0 \\ 0 & 0 & 1/\rho \\ c^2(U - v_{CW}) & \rho\,\tilde{c}^2 & j^* \end{bmatrix} \qquad \text{M. F., Slip,} \tag{28}
$$

and the characteristic polynomial is

$$
\lambda^3 - j^*\lambda^2 - \tilde{c}^2 \lambda + \tilde{c}^2 (v_{CW} - U) = 0. \qquad \text{M. F., slip} \tag{29}
$$

If the effects of slip are small, i.e., j^* and $(v_{CW} - U)$ are small, the characteristics have slopes

$$
\lambda + U \approx v_{CW}, \quad \frac{1}{2} (3U - v_{CW} + j^*) \pm \tilde{c} \qquad \text{M. F., small slip} \tag{30}
$$

That is, signals are propagated with the continuity-wave velocity, and with a slightly modified sonic velocity relative to a slightly modified average velocity.

The condition that the roots of Eq. (29) are real may be written as

$$\left[\tilde{c}^2 \left(U - v_{CW} + \frac{1}{3} j^* \right) + \frac{2}{27} j^{*3} \right]^2 \leq \frac{4}{27} \left(\tilde{c}^2 + \frac{1}{3} j^{*2} \right)^3 . \tag{31}$$

This is clearly a limitation on $|U - v_{CW}|/\tilde{c}$. The general form is not enlightening; but if we assume j^* is small, the result is

$$|U - v_{CW}| \leq \frac{2}{3\sqrt{3}} \tilde{c} \simeq 0.385 \tilde{c} \text{ for } j^* \ll \tilde{c} , \tag{32}$$

Therefore, for stability, the drift-flux correlation $j(\rho, G, P)$ cannot permit a continuity wave to propagate relative to the average velocity at more than some fraction (~ 0.385 for $j^* = 0$) of the effective sonic velocity.

The case of slip included but momentum flux neglected, while involving more complicated algebra, produces no new information; there is some (albeit very complicated) maximum velocity of a continuity wave relative to the mixture above which the equations are unstable.

Application to the Westinghouse-Zuber Correlation -- As shown in the previous section, the stability requirement for the present drift-flux equations is

$$|v_{CW} - G/\rho| < Bc , \tag{33}$$

where B is some extremely complicated expression. From the definitions

$$j_g = j - j_\ell = \alpha C_o j + \alpha V_{gj} \tag{34}$$

$$v_{CW} = \left(\partial j_g / \partial \alpha \right)_j \tag{35}$$

$$G = \rho_g j_g + \rho_\ell j_\ell . \tag{36}$$

we find

$$v_{CW} - G/\rho = \left[\alpha \frac{\partial C_o}{\partial \alpha} + (C_o - 1) \rho_\ell / \rho_m \right] j + \left[\rho_\ell V_{gj} / \rho_m + \alpha \partial V_{gj} / \partial \alpha \right] . \tag{37}$$

At moderate pressures, say 25 psi, the churn-turbulent-bubbly and film-annular correlations intersect at $\alpha \approx 0.82$. For the former

110

$$C_{oB} = 1.2 \quad , \tag{38}$$

$$V_{gjB} = v_{\infty b} \quad , \tag{39}$$

where

$$v_{\infty b} = 1.41 \left[\sigma g (\rho_\ell - \rho_g)/\rho_\ell^2 \right]^{1/4} \sim 2 \text{ ft/s} \tag{40}$$

Then

$$(v_{CW} - G/\rho)_B = \rho_\ell (0.2j + v_{\infty b})/\rho, \tag{41}$$

while for countercurrent flow

$$-0.83 \, v_{\infty b} \approx V_{gjB}/C_o \leq j \text{ countercurrent} \leq \alpha V_{gjB}/(1 - \alpha C_o) \approx 50 \, v_{\infty b} \quad , \tag{42}$$

which leads to

$$10 \text{ ft/s} \approx 4.6 \, v_{\infty b} \leq (v_{CW} - G/\rho)_B \leq 61 \, v_{\infty b} \approx 120 \text{ ft/s} \tag{43}$$

For film-annular flow,

$$C_{oA} = 1/(\alpha + \beta - \alpha\beta) \approx 1.20, \tag{44}$$

where

$$\beta = (\rho_g/\rho_\ell)^{1/2}/0.49 \approx 0.066, \tag{45}$$

and v_{gj} may be written in the form

$$V_{gj} = 4.63 (1 - \alpha) C_{oA} \, v_{\infty b} \quad . \tag{46}$$

After some manipulation, we find

$$(v_{CW} - G/\rho)_A = \left\{ C_o^2 \left[(1 - \alpha)^2 \beta\rho_\ell - \alpha^2 \rho_g \right]/\rho \right\} \left[(1 - \beta)j + 4.63 \, v_{\infty b} \right] \quad . \tag{47}$$

The limits for countercurrent flow are the same as for bubbly flow, Eq. (42), but now

$$0.1 \text{ ft/s} \approx 0.044 \, v_{\infty b} \leq (v_{CW} - G/\rho)_A \leq 0.59 \, v_{\infty b} \approx 1.2 \text{ ft/s} \tag{48}$$

467 299

111

For these conditions, $P \approx 25$ psia, $\alpha \approx 0.82$, the sonic velocity is

$$c \approx 30 \text{ ft/s} \tag{49}$$

Therefore, if B in Eq. (33) is of the order of unity, we would expect churn-turbulant-bubbly flow to be (probably) unstable for countercurrent or small cocurrent flow while film-annular flow is probably stable. This is in apparent agreement with our calculational experience.

4.4 FRAP and FLOOD

A continuing effort is being directed towards developing a FRAP-FLOOD package capable of analyzing the post-blowdown conditions of a reactor equipped with a UHI system. The FRAP T4 code is a single-pin heat transfer code which uses the time-dependent coolant properties calculated by RELAP4-MOD5 during the blowdown portion of a LOCA. An attempt was made to use the FRAPT4 code with all of the LACE (Licensing Audit Code) options activated in conjunction with output from the UHL1 blowdown run. It was discovered that LACE Option 14 (Fuel Deformation) was not contained in our version of the code. Additionally, the gas thermal conductivity option (Option 16) would not calculate because of an undefined variable, the fuel melt temperature. In order to exercise the FRAP T4 (LACE) program, the two modes were removed from the computational loop. The coding required to complete the LACE option package has been requested from INEL.

Future Work -- The two nonfunctioning LACE models will be updated upon receipt of a corrected version from INEL. Sample calculations will be made using one of the UHL2 blowdown series to determine the sensitivity of FLOOD to the initial quench height and midplane temperature.

4.5 References

1.   *Light Water Reactor Safety Research Program Quarterly Report, January - March 1978,* Nuclear Fuel Cycle Safety Research Department, SAND78-1511, NUREG/CR-0324, Sandia Laboratories, Albuquerque, NM, October 1978.

2.   *Light Water Reactor Safety Research Program Quarterly Report, April - June 1978,* Nuclear Fuel Cycle Safety Research Department, SAND78-1901, NUREG/CR-0422, Sandia Laboratories, Albuquerque, NM, January 1979.

3.   M. Berman, R. R. Eaton, R. K. Cole, Jr., C. . Steck, L. Dike, and D. A. Dahlgren, *LOCA Analyses Annual Report Fiscal Year 1977,* SAND78-0637, NUREG/CR-0154, prepared for U.S. Nuclear Regulatory Commission by Sandia Laboratories, Albuquerque, NM, June 1978.

4.   W. M. Bryce, *A New Flow-Dependent Slip Correlation Which Gives Hyperbolic Steam-Water Mixture Flow Equations,* AEEW - R 1099, Atomic Energy Establishment, Winfrith, Dorchester, Dorset, England, May 1977.

5.   J. A. Holmes, *The Drift Flux Correlation in RELAP-UK,* AEEW - R 1143 Atomic Energy Establishment, Winfrith, Dorchester, Dorset, England, November 197.

6.   *RELAP4/MOD5 A Computer Program for Transient Thermal-Hydraulic Analysis of Nuclear Reactors and Related Systems User's Manual, Volume I, RELAP4/MOD5 Description,* ANCR-NUREG-1335, Aerojet Nuclear Company, Idaho National Engineering Laboratory, Idaho Falls, ID, September 1976.

7.   G. W. Johnsen, G. L. Singer, L. H. Sullivan, S. R. Behling, C. H. Burgess, H. Chow, D. I. Slegel, D. K. Patel, L. J. Siefken, and B. W. Burnham, *RELAP4/MOD7 Blowdown Code, Version 2 User's Manual,* CDAP-TR-78-036, Idaho National Engineering Laboratory, Idaho Falls, ID, August 1978.

DISTRIBUTION:

US Nuclear Regulatory Commission
  (287 copies for R3)
Division of Document Control
Distribution Services Branch
7920 Norfolk Ave
Bethesda, MD 20014

Kenforschungszentrum Karlsruhe (7)
Postfach 3640
7500 Karlsruhe 1
Federal Republic of Germany
Attn: Dr. J. P. Hosemann
        Projekt Nuklear Sicherheit (PNS) (4)
     Dr. H. Albrecht
        Institut für Radiochemie (IRCH)
     Dr. H. Holleck
        Institut für Material-und
        Festkörperforschung (IMF)
     Dr. M. Reimann
        Institut für Reaktorbauelemente (IRB)

Prof. Dr. -Ing. F. Mayinger
Lehrstuhl und Institut für Verfahrenstechnik
TU Hannover
Callinstr. 36
3000 Hannover 1
Federal Republic of Germany

Milad Matthias
Dept. of Nuclear Studies and Safety
Ontario Hydro
700 University Ave. (H-16)
Toronto, Ontario
Canada M5G1X6

H. Seipel
BMFT
Federal Ministry for Research & Technology
53 Bonn
Federal Republic of Germany

Dr. E. Herkommer
Institute for Reactor Safety
5000 Koln 1
Gloschengasse 2
Federal Republic of Germany

Professor Dr. D. Unger
IKE
University of Stuttgart
7 Stuttgart - Vaihingen
Pfaffenwaldring 31
Federal Republic of Germany

Dr. Ian Brittain
United Kingdom Atomic Energy Authority
Atomic Establishment, Winfrith
Dorchester, Dorse
England

G. H. Kinehin
Safety & Reliability Directorate
Wigshaw Lane
Culeheth
NR Warnington, Cheshire
England

Dr. M. Peehs
KWU
Abt. Rb. 3
852 Erlangen
Postfach 325
Federal Republic of Germany

Dr. M. Dalle Doane
Kernforschungszentrum Karlsruhe
Institut für Neutronenphysik und Reaktortechnik
7500 Karlsruhe 1
Postfach 3640
Federal Republic of Germany

Dr. H. Kottowski
c/o - Euratom Ispra
21020 Centro Euratom di Ispra
(Varese) Italy

US Nuclear Regulatory Commission (5)
Office of Nuclear Regulatory Research
Washington, DC 20555
Attn: W. C. Lyon
     N. Zuber
     S. Fabie
     C. E. Johnson
     R. R. Sherry

US Nuclear Regulatory Commission (3)
Division of Systems Safety
Office of Nuclear Reactor Regulation
Washington, DC 20555
Attn: B. Sheron
     N. Rauben
     E. Throm

US Department of Energy
Operational Safety Division
Albuquerque Operations Office
P. O. Box 5400
Albuquerque, NM 87185
Attn: J. R. Roeder, Director

Westinghouse Electric Corporation
Research and Development Center
Churchill Boro
Pittsburgh, PA 15235
Attn: M. Mazumdar
        Mathematics Department

DISTRIBUTION (Cont):

Florida International University
Department of Statistics
Tamiami Trail
Miami, FL 33144
Attn: S. S. Shapiro

EG&G - Idaho, Inc. (2)
P. O. Box 1625
Idaho Falls, ID 83401
Attn: N. D. Cox
      D. M. Snider

Electric Power Research Institute
3112 Hillview Avenue
Palo Alto, CA 94304
Attn: J. Carey

Offshore Power System
8000 Arlington Expressway
Box 8000
Jacksonville, FL 32211
Attn: D. H. Walker

Prof. S. Abdul-Kalik
Nuclear Engineering Dept
University of Wisconsin
Madison, WI 53706

Dr. S. G. Bankoff
Chemical Engineering Dept
Northwestern University
Evanston, IL 60201

Westinghouse Advanced Reactor Division
P. O. Box 158
Madison, PA 15663
Attn: L. E. Strawbridge

Westinghouse Electric Corp. (2)
Bettis Atomic Power Laboratory
P. O. Box 79
West Mifflin, PA 15122
Attn: F. W. Lincoln
      W. D. Peterson

Westinghouse Electric Corp. (2)
Nuclear Energy Systems
P. O. Box 355
Pittsburgh, PA 15230
Attn: R. P. Vijuk
      M. Y. Young

Los Alamos Scientific Laboratory (2)
P. O. Box 1663
Los Alamos, NM 87545
Attn: M. McKay
      J. Jackson

400	C. Winter
1200	L. D. Smith
1223	R. B. Easterling
1223	I. J. Hall
1537	N. R. Keltner
2514	D. E. Mitchell
4000	A. Narath
4400	A. W. Snyder
4410	D. J. McCloskey
4412	J. W. Hickman
4420	J. V. Walker
4422	R. L. Coats
4422	D. W. Varela
4423	J. E. Powell
4425	W. J. Camp
4440	G. R. Otey
4441	M. Berman (10)
4441	L. D. Buxton (5)
4441	R. K. Byers
4441	R. K. Cole, Jr.
4441	T. J. Bartel
4441	B. W. Burnham
4441	P. Tomasko
4441	J. S. Muir
4442	W. A. Von Riesemann
4443	D. A. Dahlgren
4450	J. A. Reuscher
4533	B. D. Zak
4550	R. M. Jefferson
4732	H. J. Sutherland
5131	W. B. Benedick
5511	D. F. McVey
5511	B. M. Bulmer
5511	M. L. Corradini
5512	D. W. Larson
5520	T. B. Lane
5530	W. Herrmann
5532	B. M. Butcher
5534	J. E. Smaardyk
5641	G. P. Steck
5830	M. J. Davis
5830	L. S. Nelson (5)
5831	N. J. Magnani
5831	D. A. Powers (5)
5833	F. J. Zanner
5846	E. K. Beauchamp
5846	R. A. Sallach
8266	E. A. Aas
3141	T. L. Werner (5)
3151	W. L. Garner (3)
	For: DOE/TIC (Unlimited Release)
3172-3	R. P. Campbell (25)
	For Distribution to NTIS

15

Org.	Bldg.	Name	Rec'd by *	Org.	Bldg.	Name	Rec'd by *

* Recipient must initial on classified documents.